UNIVERSITY OF PAVIA

FACULTY OF ENGINEERING

DEPARTMENT OF ELECTRICAL, COMPUTER AND BIOMEDICAL ENGINEERING

PHD PROGRAM IN ELECTRONICS, COMPUTER SCIENCE AND ELECTRICAL

ENGINEERING

Innovative technique for generation of femtosecond high energy pulses in fiber lasers

Candidate: Sara Pizzurro

Supervisor: Federico Pirzio

XXXVI cycle

A.A. 2022/23

Contents

Abstract

In this thesis is presented the realization of a Mamyshev oscillator. It is one of the most promising solutions for environmentally stable fiber laser oscillators for ultrashort pulse generation, and this architecture represents an alternative to SESAM to achieve passive mode-locking by means of a saturable absorber (SA) effect in fiber lasers. The Mamyshev oscillator is an oscillator composed of two concatenated Mamyshev regenerators usually seeded by an external laser source. Its operating principle is based on self-phase modulation (SPM), which allows spectral broadening of the signal in the fiber, and on two non-overlapping spectral filters, which prevent CW lasing and thus force pulse formation.

The Mamyshev oscillator proposed in this work is based on single-mode, polarization-maintaining (PM) fibers and on a low-power (~ 400 mW) single-mode pump laser diode. To start the Mamyshev oscillator, we injected into the cavity a single pulse emitted by a sub-nanosecond passively Q-switched laser spectrally broadened by the nonlinear four-wave mixing (FWM) effect while propagating in a standard single-mode PM passive fiber.

For the spectral filtering, we investigated different solutions based on super-gaussian filters and gaussian filters. After a careful experimental investigation, we chose a combination of the two filters, obtaining 3.5 nJ pulse energy and a minimum compressed pulse duration of ~ 170 fs.

In order to increase the pulse energy, I also realized a chirped pulse fiber amplifier reaching ~ 100 nJ of pulse energy with a pulse duration after compression of 200 fs. This was pivotal for the optical parametric generation experiments I performed using the Mamyshev oscillator pulses as pump source for two different parametric crystals:

a 42-mm-long MgO:PPLN and a 19-mm-long PPLN. Such long crystals are not prone to group velocity mismatch effects when pumped at 1064 nm for generation of a signal around 1.55 μm, because the dispersion properties of the nonlinear materials are such that the pump and idler present the same group velocity for the wavelengths for which the phase-matching condition occurs. At the output we obtain similar results for both crystals: ~ 40 nJ of signal and ~ 20 nJ of idler with a conversion efficiency of 50% and 20% respectively, with signal pulse duration of about ~ 300 fs close to the Fourier limit, and a wide tuning range. Both the crystals showed very good average output power stability in Gaussian TEM$_{00}$ beam profiles with beam quality factor M$^2 \leq 1.5$. The very good nonlinear frequency conversion efficiency, beam quality and reasonable pulse duration preservation are a clear evidence of the effectiveness of the femtosecond fiber oscillator and amplifier based on the Mamyshev architecture I developed.

Chapter 1

Introduction

In recent years, in the field of laser source technologies, ultrafast lasers have been a prominent academic and industrial research topic. Ultrafast lasers are optical devices capable of generating ultrashort pulses, i.e., light pulses in the picosecond or femtosecond regime.

This type of lasers proved to be advantageous and innovative for a large number of applications in different fields, such as high-precision materials processing and micromachining in the industrial field, or the realization of advanced devices for treatments and diagnosis in the biomedical field, or also in fundamental and applied physics research, such as microscopy and multispectral imaging.

The reason why ultrafast lasers have become a key topic in research nowadays is because of the extremely short pulse duration they permit to achieve. This allows such lasers to reach very high peak intensity even with relatively low pulse energy. Moreover, as a result of their ultrafast excitation dynamics, when the laser beam is focused on a target material, negligible energy transfer in the form of heat occurs to the rest of the material. This is because the pulse duration is shorter than the vibrational relaxation time characteristic of the material, therefore the energy is deposited faster than it is dissipated through the material away from the point of impact [1]. This is especially true in the case of pulses in the femtosecond regime, which permit to process even soft and delicate materials that cannot be treated optically with conventional nanosecond or picosecond pulses.

For these reasons, scientific and industrial research is particularly active in the study

of ultrafast lasers. However, the physics and technology behind the generation and amplification of picosecond and femtosecond pulses are very different. The latter is more complex to realize, less reliable, and more expensive. Nevertheless, femtosecond pulses have the capability to enable new applications that cannot be addressed with picosecond pulses.

About 20-25 years ago, the femtosecond solitonic regime could be achieved mostly with bulk solid-state lasers based on Ti:Sapphire, which allowed to achieve pulse durations lower than 10 fs. For many applications still possible with longer pulse durations, in the range of hundreds of fs, Nd:glass-based lasers were used. For many years they represented the state-of-the-art in ultrafast lasers. This was true until the advent of Semiconductor Saturable Absorber Mirrors (SESAMs), which greatly simplified the implementation of mode-locked lasers. Moreover, the continuous improvements in the quality of the pump diodes resulted in the establishment of highly efficient quasi-three-level Yb-doped bulk femtosecond laser operating in the solitonic regime. The improvement of the performance of the pump diodes also led to the emergence of fiber lasers, although at the beginning they were operated mostly in the continuous wave (CW) regime.

Fiber lasers present some advantages over the classic bulk lasers, in fact, they can offer more compact and lightweight solutions, they are intrinsically misalignment-free, hence they can be more stable against environmental conditions. Moreover, fiber lasers are inherently robust, and can be cheaper than bulk solid-state lasers [2]. In addition, the geometry of the fibers and their built-in waveguiding effect permit to obtain excellent beam quality, even at very high average power levels [3]. For all the aforementioned advantages, fiber lasers represent a new frontier for the generation of ultrashort pulses.

However, fiber lasers have some drawbacks mainly caused by the strong confinement of the beam in the very small core of the fiber required to obtain a single-mode output beam. They are unwanted non-linear effects and optical intensity driven damages that can easily occur due to the high confinement and long interaction length within the optical fiber.

In order to have an idea of the maximum tolerable energy before reaching the damage

threshold, referring to the standard critical intensity value of $\sim 1\,\text{GW/cm}^2$, assuming a pulse duration of about 10 ps propagating in a single mode (SM) fiber with a core diameter of $\sim 5\,\mu$m (such as the single-mode fiber at 1 μm wavelength that will be introduced in the next chapters), the maximum energy allowed is in the order of few nJ.

If on the one hand, non-linearity can be harmful in some applications, like in fiber optic transmission systems, on the other hand, some advanced fiber laser solutions take advantage of such effects in order to generate ultrashort pulses.

In Fig. 1.1 you can observe the progress in the peak power provided by various types of ultrashort fiber oscillators dating from 1990 to 2020 [2], the year I enrolled in my Ph.D. course. In the chart, the range of peak powers offered by commercially available (and quite expensive!) Ti:sapphire based laser systems is marked by the striped grey area. Each result reported in the graph is obtained with fiber laser systems relying on standard, single-mode fiber with a core diameter of 6 μm. Each different marker correspond to different types of fiber oscillators that were progressively developed and investigated.
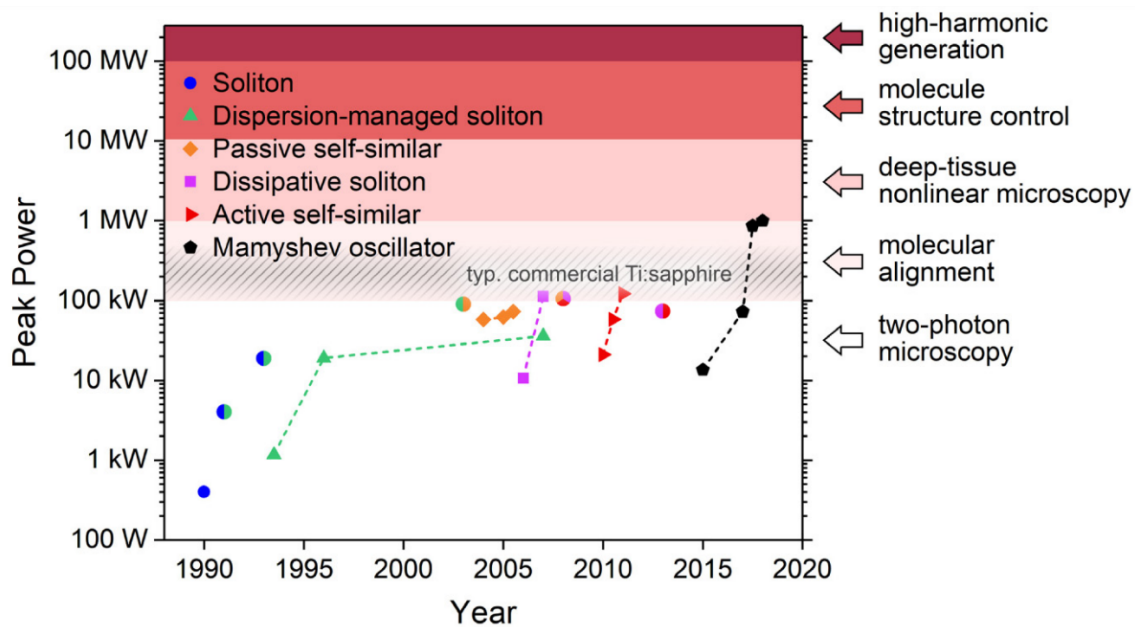

FIGURE 1.1: Peak power evolution for different ultrafast fiber lasers.

The working principle of these fiber lasers is briefly explained in the following list.

- In the *solitonic regime* (blue circle), the nonlinearity given by the self-phase modulation (SPM) and group velocity dispersion (GVD) are balanced, preserving the temporal and spectral shape of the pulses circulating in the fiber even for long propagation distances. This means that in the quasi-soliton pulses there is no temporal broadening or change in the optical spectrum and the pulses, and it is almost transformed-limited at each roundtrip. However, the nonlinear dynamics that occur in fibers at short pulse durations are the main reason why the solitonic fiber lasers yield very low pulse energy, typically in the order of a few pJ and the average power in the order of mW, with pulse durations limited to several hundreds of fs [3].

- In soliton mode-locking lasers, the dissipative effects due to gain media, loss, saturable absorbers (SA), or spectral filtering (if present) are weak compared to the conservative effects of SPM and GVD. However, in the so-called *dissipative soliton* mode-locking (pink cube in the chart) such dissipative effects are not negligible and can be adequately exploited to achieve mode-locking [4]. The dissipative soliton regime leads to an increase in energy. compared to the solitonic regime, up to a few tens of nJ. The output pulses can be de-chirped outside the laser cavity, reaching $\sim$ 100 fs duration.

- The *dispersion-managed soliton* regime (green triangle), exploits portions of fiber in which the sign of group velocity dispersion is alternate. They are used to periodically stretch and compress the pulses at each roundtrip. Since the pulse duration can be increased, the pulse energy can also be increased without suffering an excessive non-linear phase shift [3]. The output pulses can be de-chirped to < 100 fs duration with energies of a few nJ [5].

- *Self-similar* fiber oscillators, on the other hand, exploit parabolic amplification of the pulse in passive (orange rhombuses) or active (red triangle) fibers. The pulse, as it

propagates in the fiber, exploits nonlinearity, dispersion, and gain, so that it develops a parabolic shape and a linear up-chirp that, during amplification, is conserved due to the self-similar evolution experienced by the pulse. After output coupling, the original shape of the pulse is restored by a spectral filter for the next roundtrip. With normal net dispersion, the highest energies can be produced, in fact, pulses of a few nJ and a few ps can be obtained, which can be compressed to < 100 fs duration [6].

- The *Mamyshev oscillator* (black pentagram) is an ultrafast fiber laser that works in passive mode-locking, also called all-normal-dispersion femtosecond fiber lasers, where anomalous dispersion is also avoided, but the pulse evolution is generally not self-similar [7]. It is based on the combination of the spectral broadening of the pulses induced by the SPM process and two non-overlapping spectral filters: if the spectral broadening of the pulse is large enough to make the pulse pass through both filters repeatedly, a pulse with well-defined parameters is stabilized after a few iterations [8]. The mode-locking regime can be maintained since the spectral broadening is greater for higher pulse intensities, this process favors the oscillation of pulses with high peak power and suppresses the CW regime. The realization of Mamyshev Oscillators (MO) has already resulted in excellent performance. In fact, it is possible to obtain 50 nJ and 40 fs pulses (after the compression), with a corresponding peak power of 1 MW [9]. Moreover, scaling the cavity design to a larger core fiber of $\sim 10\ \mu$m, 190 nJ pulses that are de-chirped to 35 fs duration, have been obtained in [10], yielding to 3 MW peak power. These high peak power values are a fundamental prerequisite for experiments related to molecular alignment and deep-tissue nonlinear microscopy.

As can be seen, the MO represents the most promising solution for the realization of ultrafast fiber lasers. However, the limits of such techniques have so far not been fully explored and there is still much research to be done in this regard.

For these reasons, during my Ph.D. I started working on the realization of a femtosecond laser source based on the MO architecture. This study represents a new research

line for the Laser Source Laboratory of the University of Pavia, since research related to ultrafast femtosecond lasers was previously mostly based on Nd- adn Yb-doped, Diode Pumped Solid State Lasers (DPSSL).

Since this was a new research line for the group, this doctoral dissertation has a strong experimental connotation. The experiments reported in this thesis represent only the main results obtained. As usually occurs when a brand new research topic is started, we had to learn a lot from the experience, and at the beginning, we just tried to reproduce in the lab some of the most interesting results reported in literature.

As a first realization of the MO in the laboratory, we decided to operate at low average power using standard single-mode polarization-maintaining fibers at 1 μm. For the realization of the oscillator itself, the main aspect I worked on was the selection of the optimum configuration for the spectral filters, carried out by testing both super-gaussian and gaussian transmission-profile filters.

Another key aspect in the realization of the MO is represented by the methodology adopted to start the mode-locking regime. In particular, I tested two different solutions relying on external seeders. The first one was a home-made picosecond amplified fiber oscillator, which was already reported in literature. This was instrumental to start the experiments with the MO and better understand its operation principle. The second one was a low-cost, commercially available, passively Q-switched microchip laser. The results obtained with the latter were very interesting and original: we demonstrate that, to start the mode-locking in the MO, even narrow bandwidth sub-nanosecond pulses can be effective thanks to spectral broadening driven by four-wave mixing effect in a standard PM, passive fiber.

To increase the pulse energy of the low-power MO, I also built a chirped pulse fiber amplifier. This was instrumental to the nonlinear frequency down conversion experiments I later performed using for the first time this kind of femtosecond fiber laser. Part of this research was carried out at the Institute of Photonic Science (ICFO), Castelldefels, Barcelona. In fact, the amplified MO prototype was realized on transportable boards

allowing me to perform nonlinear frequency down-conversion experiments at the Parametric Optical Oscillators group headed by Prof. Majid Ebrahim-Zadeh in Spain.

This thesis is organized as follows:

- Chapter 2 is devoted to explaining the operating principle of the MO.

- Chapter 3 is focused on the realization and optimization of the experimental setup of the MO.

- In Chapter 4 I will discuss the experiments about the seeding lasers for starting the MO and the innovative solution we identified employing a passively Q-switched microchip laser as seeder.

- Chapter 5 shows the implementation of the chirped pulse amplifier (CPA) and the realization of the MO and the CPA into individual movable blocks, in order to make the setup completely portable.

- In Chapter 6 I will briefly discuss the operation principle of optical parametric generation with femtosecond pulse pump sources, and then I will present and discuss the results obtained by exploiting two different periodically poled nonlinear crystals for generation of tunable femtosecond pulses in the mid-infrared.

- In Conclusions I will summarize the main results of this work and trace the future foreseeable steps of this research activity.

Chapter 2

Principle of operation of ultrafast Mamyshev Oscillator

2.1 Mamyshev regenerator

The original idea that offset spectral filtering in combination with sufficient self-phase modulation (SPM) could be be exploited for generation of ultrafast pulses in laser oscillators, was proposed in 1994 by Michel Piché [11]. The idea went largely unnoticed, apart from a special application proposed by Mamyshev in 1998, during the 24th European Conference on Optical Communications [12]. The idea of Mamyshev was to design a "signal regenerator" in the field of telecommunications exploiting SPM and offset spectral filtering. The great potential of this technique for the generation of ultrashort pulses with high peak power was only developed experimentally in recent years, and for some reason, despite the original idea came from Piché, the class of fiber laser oscillators based on this concept, was named "Mamyshev Oscillators" (MO).

The Mamyshev regenerator [2] is based on the spectral broadening of a pulse by SPM when it propagates in a Kerr medium, such as a passive or active fiber. The spectrally broadened pulse then encounters a band-pass filter (BPF) that is offset from the central wavelength of the pulse. The offset of the BPF causes the filter band to have little overlap with the initially launched spectrum, limiting the portion of the transmitted spectrum only to the one generated by the nonlinear SPM process.

To understand the working principle of the Mamyshev regenerator, we can refer to the scheme in Fig. 2.1.
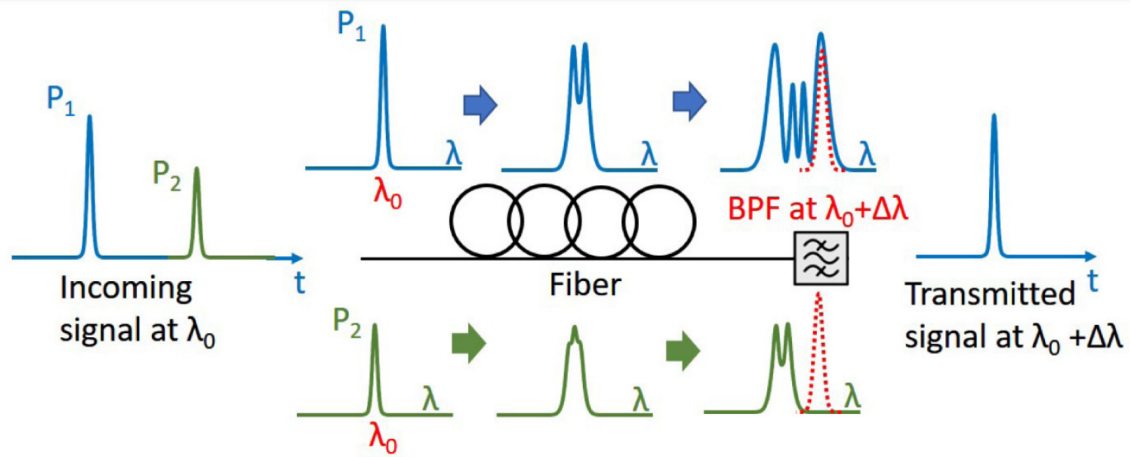

FIGURE 2.1: Mamyshev regenerator scheme.

P_1 represents the spectrum of the intense signal, while P_2 is the spike of noise that we want to suppress. Both signal and noise are centered at λ_0. When the two propagate in the optical fiber (our Kerr medium) both experience SPM, but after propagation, the spectrum of P_1, the most intense one, is broader than the spectrum of the noise P_2. This is because the SPM process is directly proportional to the intensity of the initial pulse. After the propagation in the non-linear medium, the two broadened signals arrive on the BPF with a transmission bandwidth centered at $\lambda_0 + \Delta\lambda$. At this point, part of the intense pulse P_1 is transmitted, while the noise can not pass, since it did not experienced enough SPM spectral broadening, falling outside the second BPF transmission bandwidth. Hence, the output is only related to the main signal P_1.

As you can notice, this mechanism acts as a saturable absorber (SA) in transmission, with low-intensity pulses producing insufficient SPM to be transmitted by the offset BPF. Mode-locked lasers usually start from noise and are maintained by a suitable saturable absorption mechanism. The SA promotes pulse generation by preferentially transmitting (or reflecting) higher intensities, allowing the initial random fluctuations to evolve into short pulses above the background noise level.

There are different types of SAs: they could be based on absorption in graphene,

carbon nanotubes or in semiconductors or, for fiber lasers primarily, SAs mechanisms such as nonlinear polarization rotation [13] and nonlinear loop mirrors [14] are used. The main problem nowadays with the use of material-based SAs is that they are prone to damage in high-power fiber lasers, since, under these conditions, you need to operate near the damage threshold of material. Because of this limitation, the technique proposed by Piché and named after Mamyshev was quite recently explored with great success for the realization of ultrafast fiber lasers without the use of materials exhibiting saturable absorption properties, or more complex nonlinear techniques. In fact nowadays the MO is the most promising solution for the generation of high peak power ultrashort pulses in environmentally stable resonators.

2.2 Mamyshev oscillator

The MO can be considered the natural evolution of the Mamyshev regenerator. It is an alternative to conventional mode-locking schemes exploiting SA, as it is based on the reamplification and reshaping (2R) optical regenerator technique. The MO is typically composed of two arms, each one with its own gain fiber (reamplification), output coupler, and offset spectral filter (reshaping).
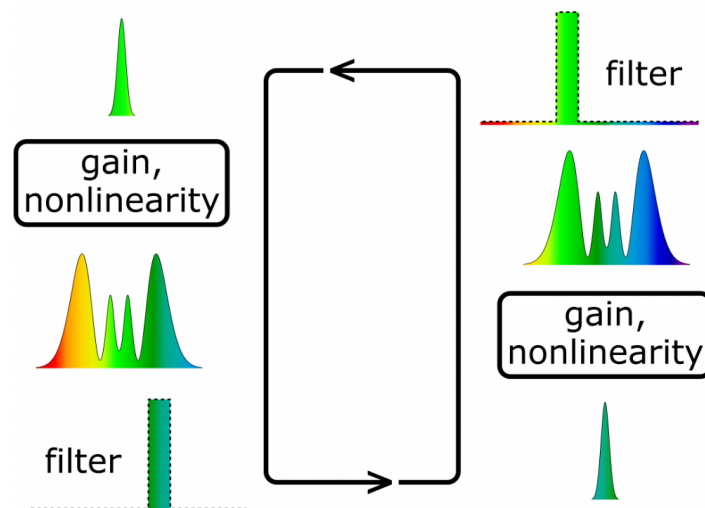

FIGURE 2.2: Effect of the MO on the pulse spectrum.

Similarly to the regenerator, the MO relies on SPM-induced spectral broadening in combination with two non-overlapping spectral filters. In this way, the MO structure acts as an effective SA to suppress CW lasing and sustain a high-intensity pulse, as explained in the previous section. Fig. 2.2 shows the effect of the MO on the pulse spectrum: between the two filters, the pulse propagates in an active fiber, exploiting power amplification, and propagates in passive fiber experiencing SPM. When the broadening of the spectrum is sufficient to repeatedly pass the pulse through both filters, stable and periodic evolution can establish.

Usually, an external, ultrashort seed pulse (few picoseconds) is injected into the cavity and the reshaping and reamplification process starts. The broadened pulse generates spectral components that can pass through the filters and, in this way, it can sustain itself and travel back and forth in the resonator.
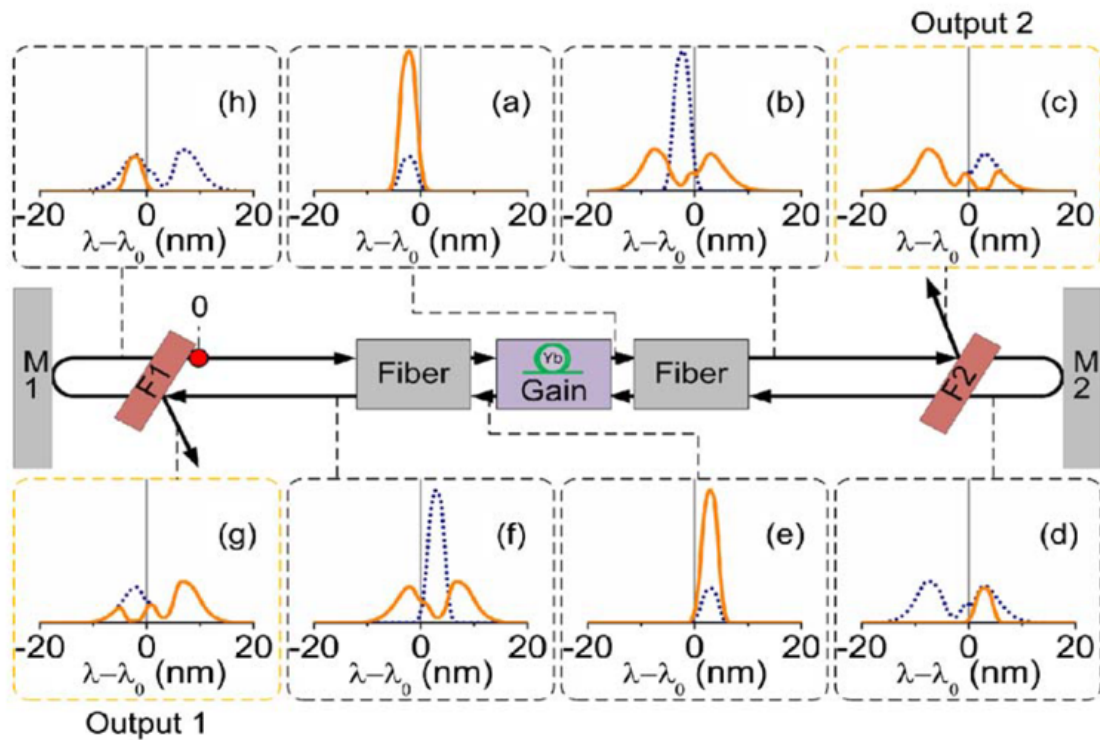

FIGURE 2.3: Schematic representation of pulse evolution in the MO.

To understand in detail the pulse evolution in the spectral domain in a MO, we refer to Fig. 2.3 (taken from [8]) in which the cavity of the MO is schematized in this way:

the gain medium is composed of a, e.g., Yb-doped fiber and to exploit SPM there are two passive fibers. There are also two offset band-pass filters F1 and F2, with the transmission bandwidth of F2 centered, e.g., at a longer wavelength with respect to F1. The cavity is closed between two mirrors M1 and M2. The different insets in the chart, named from a) to h) represent the pulse spectrum evolution in the cavity. In detail, the orange solid lines represent the spectrum of the pulse that is extracted from the resonator at the point indicated by the black dashed line, while the spectrum in the dashed blue lines is the spectrum of the pulse in the previous step. The starting point is the red dot named "0". We can assume that this position corresponds to the injection of the seeder pulse into the cavity through the reflection of the F1 BPF.

After the seed pulse is coupled into the cavity, it first travels trough the passive fiber. However, in this case, since the pulse intensity is very weak, the spectral broadening for SPM is negligible. Then it experience amplification in the Yb-doped fiber: inset (a) shows the pulse amplified (orange line) compared to the initial seed pulse (blue dotted line). At this point, due to the increase in intensity, the spectrum of the pulse propagating in the passive fiber is significantly broadened by SPM (b). Then the pulse reaches the F2 filter: the wavelengths that correspond to the BPF spectral window are transmitted, while those that fall outside the transmission bandwidth of the filter are reflected outside the cavity, generating Output 2 (c). This can be used as an output of the cavity, or simply as a monitor for the MO. The transmitted portion of the spectrum is then reflected by mirror M2 and re-coupled into the passive fiber (d). Again, even though it travels in the passive fiber, the contribution of SPM is marginal given the low intensity of the pulse. After its propagation in the active fiber, the pulse is amplified again (e) and then is spectrally broadened by SPM (f). When the broadened pulse arrives at filter F1, the reflected portion of the spectrum generates the output 1 (g), while the wavelengths that fall in the transmission window of BPF F1 are transmitted toward mirror M1 and re-coupled into the passive fiber so that a new cycle begins.

It should be noted that the transmission bands of the two filters are not overlapping, therefore no wavelength can be transmitted by F2 if the pulse inside the cavity does not

have sufficient peak power to induce significant SPM (the same reasoning applies to the F1 filter). As a result, the MO transmits only pulses with a peak power that is sufficient to "survive" in the cavity. In this case, it operates as a nonlinear optical gate. After the seed injection, few interactions are enough to stabilize the pulse parameters at well-defined energy and duration at each point in the diagram in Fig. 2.3. This establishes the mode-locking regime.

Having explained the working principle of the MO, it is now necessary to discuss some aspects related to the use of the MO as a generator of high-energy ultrashort pulses:

- the MO can generate pulses with duration of few ps, high energy (several tens of nJ), and a very broad spectrum due to the high degree of nonlinearity tolerated by the pulse if the two transmission windows of the filters are largely separated. At the output of the oscillator, therefore, it is necessary to use a compressor to obtain the shortest pulse that the spectrum can sustain. This is the reason why we implemented a negative-dispersion pulse compressor at the output of the MO to reduce the duration of the pulses, as you will see in Chapter 3 and Chapter 5.

- Since we want to obtain a broad spectrum and prevent cw lasing, the offset between the two filters must be optimized in a way that the transmission bands of the filters are not superimposed, inhibiting the CW regime. As a consequence, the oscillator cannot be self-starting. Among different starting techniques demonstrated in the literature [8] [15], the most reliable one is to use an external pulse injection that acts as the seed of the oscillation. The MO that I realized in the Laser Sources laboratory of the University of Pavia exploited an external seeder. In Chapter 4 I will present in detail the experiments on the original and innovative seeding solutions we implemented.

- Typically the MO generates pulses with worse temporal and spectral quality if compared to solitonic lasers. However, for many applications such as those related to nonlinear optics (e.g. harmonic generation, parametric frequency down-conversion, etc.), this aspect is not so critical as it is demonstrated in Chapter 6,

where I will present the results I obtained using the amplified MO I designed and built to realize femtosecond Optical Parametric Generation (OPG) in periodically-poled, group-velocity-matched crystals. In order to achieve the high intensities required for this parametric process, I realized a chirped pulse amplifier (CPA), as reported in Chapter 5.

Thus we can schematize the amplified MO I realized into three different building blocks:

1. an external seeder for starting the oscillation;

2. the MO itself, based on a standing-wave cavity and standard polarization-maintianing single mode fiber;

3. a chirped pulse amplifier to achieve the high energy and short pulse duration required for efficient nonlinear frequency down-conversion experiments.

During my Ph.D., I had the opportunity to develop and study all of these three building blocks, following this project from the beginning, realizing an ultrafast fiber laser source prototype, and then studying its direct application as pump source for OPG experiments.

Chapter 3

Low power standing-wave Mamyshev Oscillator

In this Chapter, I will present the experiments for the realization of the MO I built during the first half of my second year of Ph.D. In particular, the different techniques involved in spectral filtering will be discussed, and the experimental results obtained employing different configurations of the MO are presented. It should be pointed out that, chronologically, part of the experiments reported here were performed only after having identified and optimized the seeding technique to start the MO. The experiments regarding the seeder are presented in the next Chapter.

3.1 Oscillator Layout
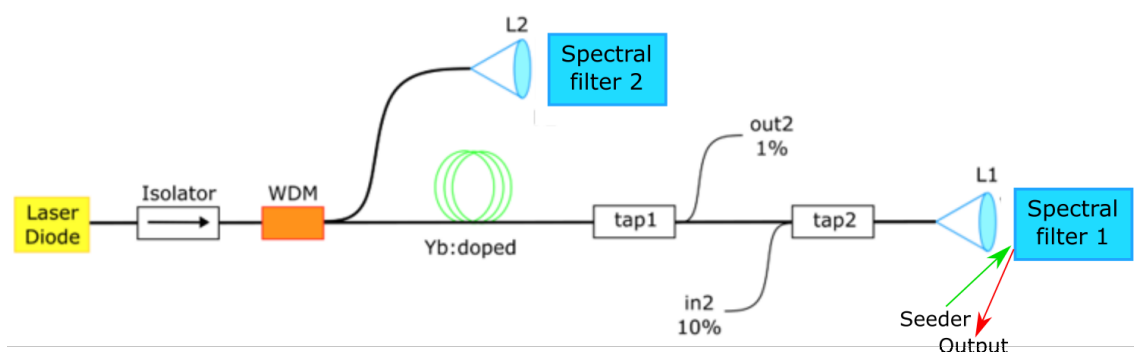
FIGURE 3.1: Initial setup tested for the Mamyshev oscillator.

The first implementation of the MO in the laboratory is shown in Fig. 3.1. The setup is similar to the one reported in [8]. MO cavity is in a standing wave configuration. Moreover it is a hybrid cavity, i.e., it is composed of fiber parts, but the oscillator ends are in air. We opted for this hybrid configuration, since it was more flexible in a preliminary stage in which we wanted to test different solutions for both the seeding and the offset spectral filters.

In detail, the following components are used for the realization of the MO:

- A 976 nm single-mode fiber-coupled laser diode is employed as the pump source. The characteristic reporting the output power as a function of the diode driving current is shown in Fig. 3.2 in blue.

- The Faraday isolator (FI) protects the laser diode against unwanted back-reflections from the cavity. In Fig. 3.2 the red curve represents the output power recorded after the isolator. The FI transmission is > 70%, resulting in > 250 mW incident pump power in the cavity at the maximum driving current of the laser diode.
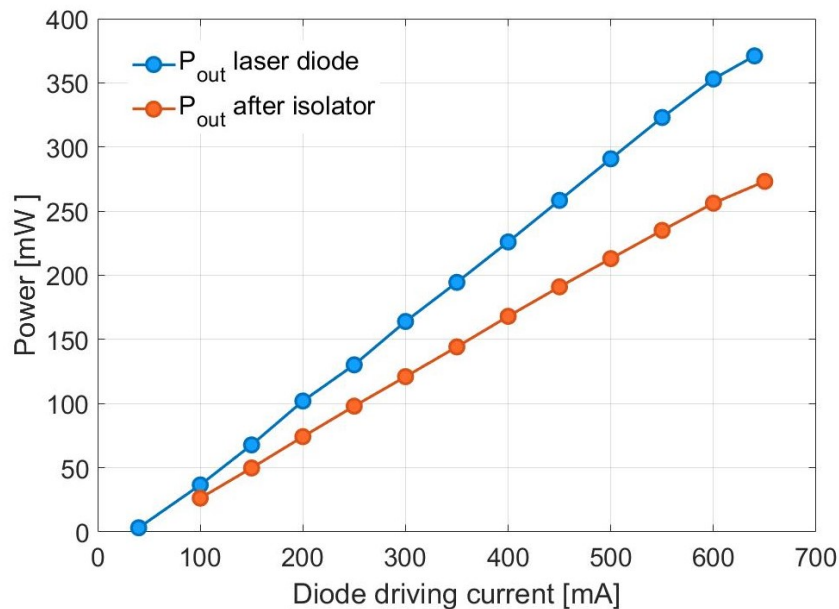

FIGURE 3.2: P-I characteristic of the pump diode in blue and after the Faraday isolator in red.

- A polarization maintaining Wavelength Division Multiplexer (WDM) at 980/1060 nm is used to combine the pump beam into the fiber cavity. The transmission of the component at the pump wavelength is $\sim$ 94%.

- The active fiber employed is a 80-cm-long, Yb-doped polarization-maintaining single-mode fiber (PM-SMF) (Nufern PM-YSF-HI), with a core diameter of $\sim$ 6 μm and a numerical aperture (NA) of 0.11. A 6.2-m-long PM-SMF (Nufern PM980-XP) is used as the passive fiber, with a core diameter of 5.5 μm and a NA of 0.12. The total length of the cavity is about 7 m, resulting in a repetition frequency of the standing-wave cavity of $\sim$ 14.75 MHz. It is possible to derive the dispersion given by the Mamyshev oscillator by taking into account the silica material of which the fiber is composed. In this way, we retrieve a $\beta_2 \approx 16 \, 10^{-30}$ s^2/mm.

- Two aspherical lenses L1 and L2 (f1 = 6.5 mm and f2 = 8 mm) were used to collimate and focalize the beam in the air parts of the cavity. With these components, we measured a maximum coupling efficiency of $\sim$ 60%.

- Taps were used to characterize the radiation circulating inside the MO cavity. In particular, tap 99/1 served as a monitor to measure the amount of radiation re-injected into the oscillator by the spectral filter 2 (out2 in Fig. 3.1). Tap 90/10 was used to monitor the seed injected into the cavity through spectral filter 1 (in2 in Fig. 3.1)). An important feature of the Taps is that they are "fast-axis blocking" components: they operate as polarizers for the radiation circulating in the Mamyshev cavity.

From this first version, the setups reported in the following sections show some adjustments that proved extremely useful in simplifying and optimizing the resonator.

For example, PM fiber collimators, with AR coating at 1-1.1 μm, replaced aspherical lenses L1 and L2. This greatly simplified cavity alignment and improved coupling efficiency up to 80%. In addition, we observed that the polarized seeder induces a deterministic and repeatable linear polarization state in the cavity, which is maintained even without any fast-axis blocking component is used. As a result, the two taps were removed

from the cavity (thus reducing cavity losses and complexity) and alternative methods to monitor the oscillator behavior were used during the experiments.

The goal of the MO is to achieve high pulse energy at low average power without employing expensive and relatively unreliable conventional SA such as SESAMs. In the next paragraphs, I will show and analyze the different solutions employed for spectral filtering, with their advantages and disadvantages, which led to the realization of the final version of the oscillator.

3.2 Two band-pass filters configuration
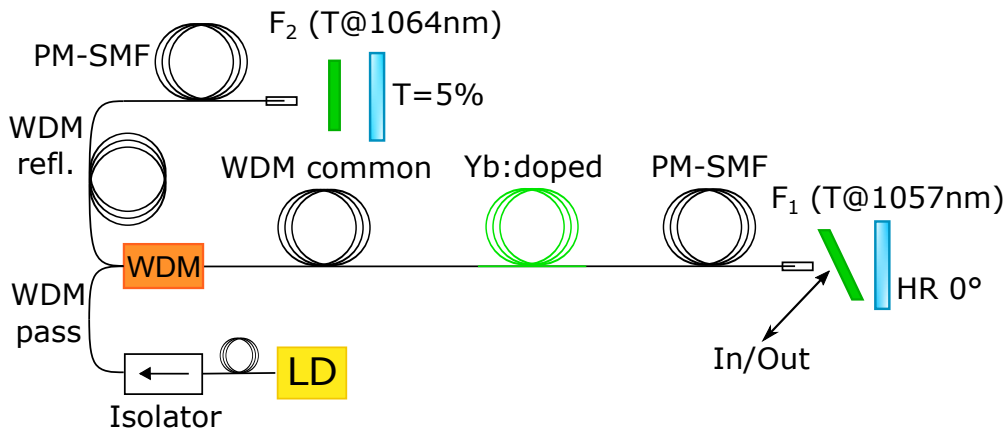
FIGURE 3.3: Two band-pass filter configuration setup.

The first configuration I implemented (see Fig. 3.3) involves two identical band-pass filters (BPFs, Semrock Max-Part Number: LL01-1064-12.5). They are super-gaussian filters with a top-hat transmittance profile with a full-width at half maxiumum (FWHM) bandwidth of ~ 3.5 nm and a transmission window central wavelength of 1064 nm at normal incidence. The central output wavelength can be continuously changed (red-shifted) by adjusting the filter incidence angle. The maximum transmission of the BPFs is > 95%. The measurement of the transmission curves at different incidence angles is shown in Fig. 3.4.

The BPF F_2 is placed at almost normal incidence and transmits at its nominal wavelength (1064 nm), which corresponds to the wavelength of the seeder. The F_1 filter is
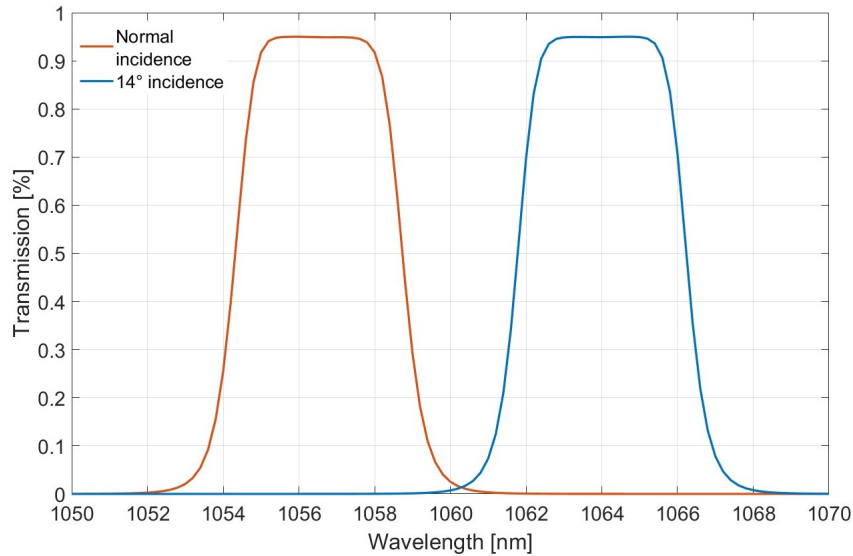
FIGURE 3.4: Filter transmission curves at different incidence angles.

tilted to shift the center of its spectral transmission window at ~ 1057 nm. The seeder beam at 1064 nm is coupled in the cavity through reflection on filter F_1. After half trip into the cavity, the seeder pulse is transmitted by the F_2 filter and reflected back by the mirror T = 5%, which is used as a monitor. When the seeder travels in the opposite path, if the spectrum is sufficiently broadened by SPM, part of it is transmitted by the F_1 and reflected by the high-reflectivity mirror (HR $0°$) to be re-coupled into the fiber. The portion of the radiation that is reflected by the filter is the output of the MO. The separation of the two filters is also adjusted to avoid CW operation.

From an experimental point of view, to align the MO cavity, I developed the following procedure:

1. Starting from a configuration in which the F_1 super-gaussian filter is absent, I place the F_2 BPF at normal incidence and align the HR $0°$ and the T = 5% mirrors to have laser action (which occurs at 1064 nm due to the presence of F_2 at normal incidence). To monitor the output power and the threshold, I exploited the output from the T = 5% mirror. I then minimize the cavity threshold by optimizing the alignment of the end mirrors.

2. I then introduce the F_1 filter into the cavity, also placed at normal incidence to allow

lasing at 1064 nm and adjust again the cavity end mirrors alignment to minimize the laser threshold. Experimentally, a threshold of about 20 mW incident pump power was measured in this condition.

3. At this point, I increase the pump power to the working level of 270 mW, and I tilt the F_1 filter to suppress the CW laser action of the cavity. This occurs when I rotate the filter by 14°, which means that its spectral transmission window is centered at 1057 nm (see Fig. 3.4).

4. At this point the seed pulse is injected in the MO and mode-locking starts.

In this configuration, with an incident pump power of 270 mW, I measured an average output power of 55 mW, which corresponds to 3.7 nJ at the repetition rate of 14.75 MHz in a linearly polarized, TEM_{00} laser beam.

The MO pulses are then directed to a Treacy compressor [16] configured with four-bounces on a single blazed reflection grating (300 grooves/mm). In Fig. 3.5 you can observe the autocorrelation (AC) trace after compression (Fig. 3.5 a, black line), and the corresponding spectrum (Fig. 3.5 b). The particular shape of the spectrum is due to the super-gaussian F_1 filter: the spectrum is reflected to the output, except for the portion corresponding to the transmission band of the filter, which is transmitted and reflected back into the fiber by the HR mirror. The hole in the spectrum therefore matches the transmission band of the BPF F_1. A pulse duration of 88 fs is measured assuming a $sech^2$ curve fit (red line). However, we can observe the presence of a pedestal in the AC trace of the pulse. Nevertheless, as it is shown in Fig. 3.6, this pedestal can be effectively reduced or even removed, by progressively cutting-off the blue part of the spectrum with a sharp blade properly inserted in the Treacy compressor where the spectral components are spatially separated.

In detail, you can notice how cutting the blue part of the spectrum (bottom graphs), improves the quality of the pulse, in the sense of a reduction of the pedestal. To quantify the improvement, we calculated the area underneath the AC best-fit function and the area underneath the measured AC trace. The ratio of the areas gives an estimation of
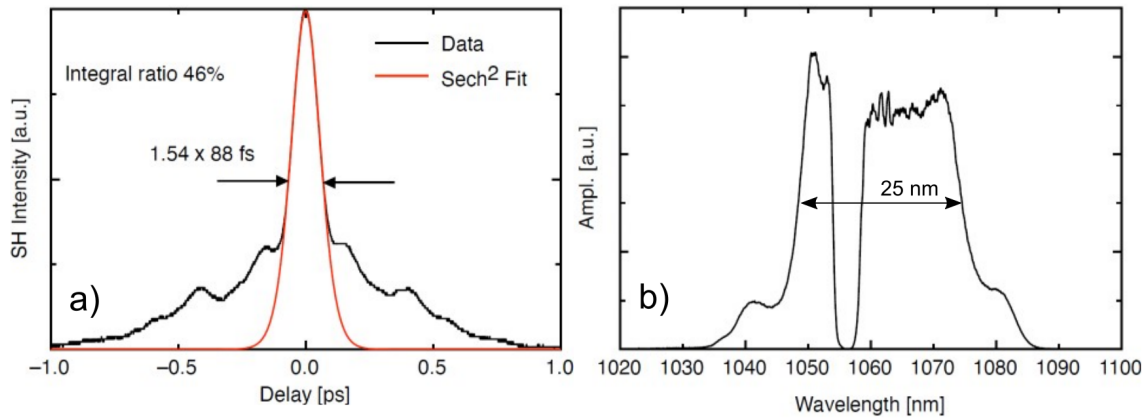
FIGURE 3.5: a) Autocorrelation trace of the compressed pulses (black line) and hyperbolic secant fit (red line). b) Output spectrum of the Mamyshev oscillator.

the amounts of the total energy contained in the main pulse. In fact, from the first to the third case, the integral ratio improves from 46% to 84%, with a maximum pulse duration of 175 fs. By performing this pulse-cleaning operation, however, the energy is reduced to 1.3 nJ from the initial value of 3.7 nJ. Thus, about 64% of the initial energy of the pulse is lost.
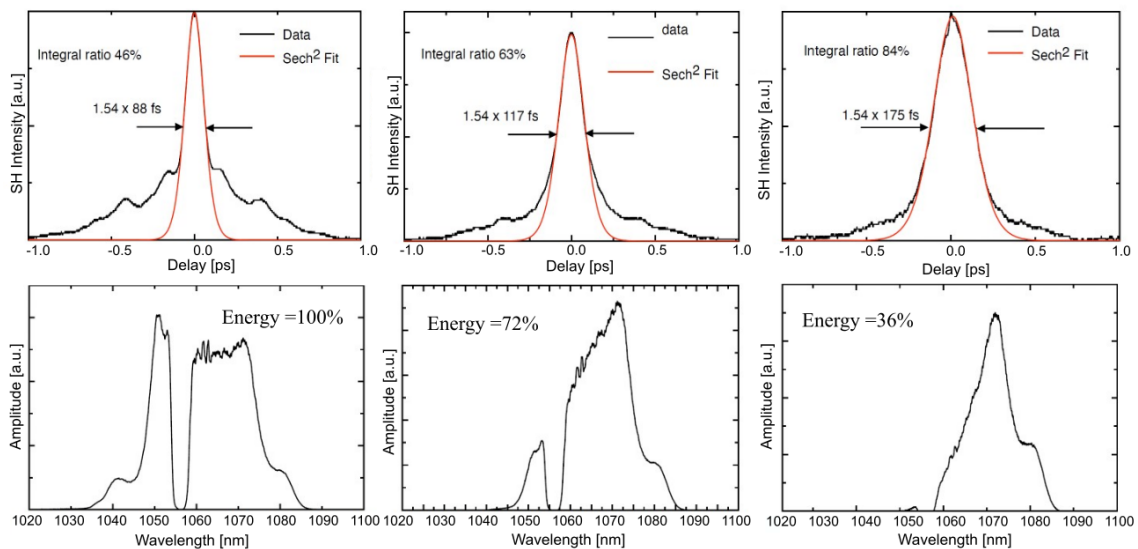
FIGURE 3.6: Upper graphs: autocorrelation trace of the pulses (black line) and sech^2 fit (red line). Bottom graphs: spectra of the pulses without cutting, and with cut of the blue part of the wavelengths.

It is well known in the literature that the Super-gaussian filter allows for maximum

coupling efficiency, achieving few nJ of output energy with the MO in our case, but at the expense of the quality of the pulses [9]. For this reason, we decided to explore other alternative solutions with Gaussian spectral filtering.

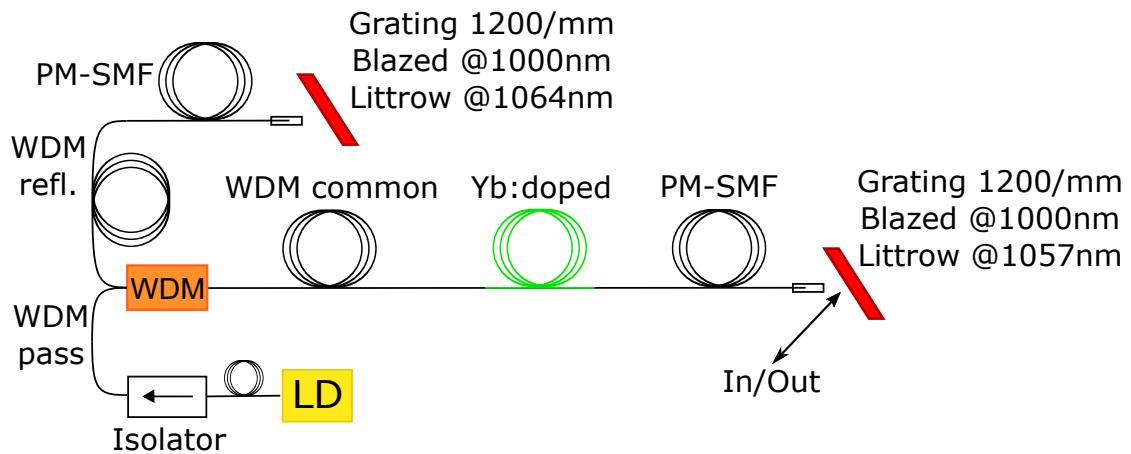## 3.3 Two reflection-gratings configuration

FIGURE 3.7: Two gratings configuration setup.

In this second configuration, spectral filtering by means of reflection-gratings was chosen to improve the spectral quality of the pulses. To this purpose, two blazed diffraction gratings were employed (Thorlabs GR13-1210). Both gratings have 1200 grooves/mm, are blazed at 1 μm and are used in Littrow configuration, i.e., the 1st order of diffraction, which is the most intense one, is reflected in the same direction as the incoming light. Thus, the beam is reflected back into the fiber oscillator. The Gaussian spatial filtering given by the fiber aperture, results in Gaussian spectral filtering profile given by the dispersion of the chromatic components of the laser beam in the horizontal plane due to the grating. In this way, the blazed reflective diffraction gratings, in combination with the fiber, can be used as wavelength-selective mirrors with a Gaussian spectral shape.

In the setup shown in Fig 3.7, one grating is placed at the Littrow angle for 1064 nm, and the other one is put at the Littrow angle for 1057 nm and acts as the seed input/MO output mirror.

In order to estimate the width of the spectral band ($\Delta\lambda$) back-reflected into the MO by the gratings, we can proceed as follows. Given the angular dispersion of the diffraction grating D, measured in nm/mrad, if we call 2θ the full diffraction angle of the laser beam, we have:

$$\Delta\lambda = D\,2\theta \qquad (3.1)$$

For our 1200 grooves/mm diffraction grating at Littrow, we have $D \simeq 0.67$ nm/mrad. θ is the angular divergence of the diffracted beam, given by:

$$\theta = \frac{\lambda}{\pi\,w} \qquad (3.2)$$

where $\lambda \simeq 1\mu$m is the central wavelength of the beam, and w is the waist of the beam on the grating. The value of w, measured by the knife edge technique, is $\sim 200\ \mu$m.

Considering the expressions (3.2), the equation (3.1) for the wavelength reflectivity bandwidth becomes:

$$\Delta\lambda = \frac{2D\lambda}{\pi w} \sim 2.5\ \text{nm} \qquad (3.3)$$

In this setup configuration with gratings as wavelength-selective mirrors, the working principle is the same as explained in section 3.2. In addition, the gratings have the advantage of simplifying alignment procedures for optimizing spectral filter separation. Moreover, the zero-order reflection (specular reflection) from the grating can be used as a monitor for the laser, and as output for the other grating.

The alignment procedure for the MO is similar to the one explained before. In detail:

1. I start with a hybrid cavity in which there is a mirror and a grating so that the laser action is at 1064 nm (wavelength defined by the grating tilt in the horizontal plane). I then optimize the cavity alignment.

2. I remove the mirror and introduce the second grating into the MO cavity so that we still have laser action at 1064 nm. I then minimize the threshold.

3. At a pump power of 270 mW, I simply tilt the grating in the horizontal plane to change the Littrow wavelength from 1064 nm to 1057 nm. In this way, CW regime is avoided.

4. At this point the seed pulse is injected in the MO through the 0-th order reflection of the input/output grating and mode-locking starts.
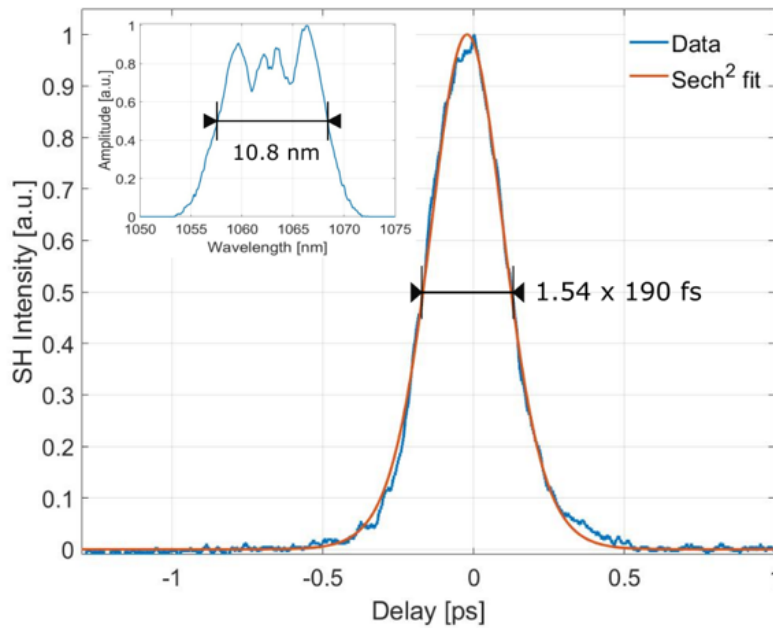

FIGURE 3.8: Autocorrelation trace of the pulse (blue line) and hyperbolic secant fit (red line). Inset: output spectrum.

As expected, the quality of the compressed pulses is greatly improved thanks to the smooth Gaussian spectral reflectivity profile of the gratings acting in combination with the spatial filtering effect of the fiber aperture, and pulse duration remains relatively short (about 190 fs see Fig. 3.8). However, using the two gratings as spectral filters, a maximum average power of only 15 mW is measured. This means that the available energy of the oscillator is 1 nJ, a value lower than the one measured with the two band-pass filters in the case of a maximum spectrum cutoff of 1.3 nJ. This is due to the lower coupling efficiency of the grating which is in the range 20-30%, whereas before we experienced a sort of cavity dumping due to the sharp spectral response of the super-gaussian filters.

This second configuration shows that the Gaussian filter guarantees high spectral and temporal quality pulses, but at the expense of a significant reduction of efficiency, output pulse energy and thus peak power.

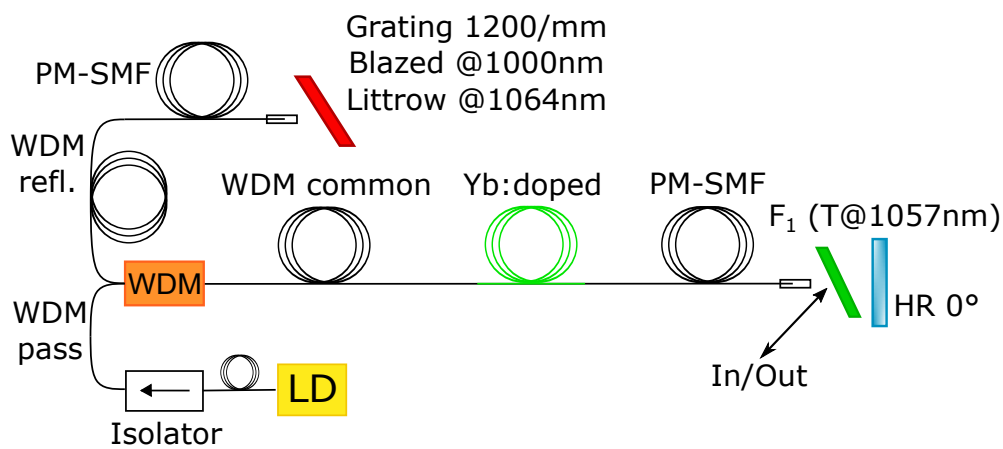## 3.4 Band-pass filter in combination with diffraction grating configuration

FIGURE 3.9: Band-pass filter + grating configuration setup.

For the third configuration implemented, the advantages associated with the two previously tested setups were combined: better spectral quality of the pulses (Gaussian filter) combined with an output power of the Mamyshev oscillator of few nJ (Super-Gaussian filter). For this reason, the cavity is composed of the tilted BPF at 1057 nm as input/output, which ensures excellent coupling due to its spectral dumping effect, and the grating put at Littrow angle at 1064 nm in the other branch of the MO for enhance the quality of the pulses (see Fig. 3.9).

The evolution of this configuration included two steps to optimize the performance.

1st step: 0.8-m Yb-doped fiber and 14.75-MHz pulse repetition rate

In this first configuration, only the spectral filtering was changed. The cavity length remained the same as the previous two configurations, therefore, the pulse repetition frequency is 14.75 MHz. During the experiments, however, it was noticed that a residual un-absorbed pump component was also present at the output of the oscillator. To understand this behavior, I explored how the spatial separation of spectral filters could affect this residual pump. The results are shown in Fig. 3.10.
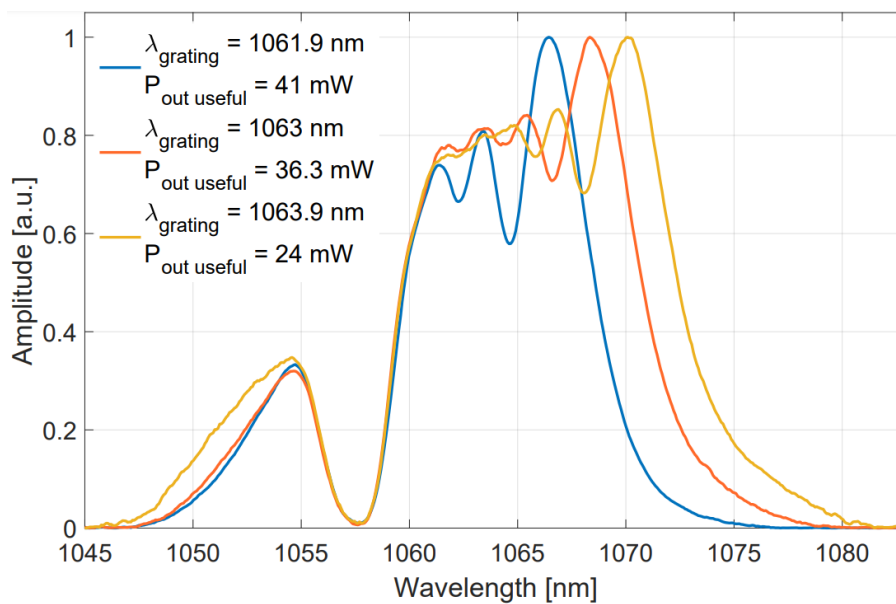

FIGURE 3.10: Output spectra for three different spectral offsets.

In this graph, you can observe three spectra recorded at the output of the MO by shifting the central wavelength of the reflection grating. The graph also reports the corresponding measured output power of the MO once the residual pump contribution was subtracted. Since the band-pass filter remained centered at 1057 nm, you can see that larger separations lead to wider spectra, but the useful output power tends to decrease. Thus, separate the spectral filters bands causes less in-band injection in this configuration, consequently, there is an increase in residual pump power because the amount of power injected back in the cavity by the band-pass filter is not enough to saturate well the active fiber thus enhancing pump absorption in the quasi-three level Yb-doped fiber. Moreover, since at any spectral filter separation we measured residual pump power in

the output, we can conclude that the active fiber length might be optimized by increasing it.

Despite this un-optimized operating condition, even in the case where spectral broadening is maximum (yellow curve) and the output average power is lower, the useful output pulse energy is ~ 1.7 nJ, which is almost a factor 2 greater than the energy obtained with the two reflection gratings configuration. In addition, the corresponding AC trace measured, after the compressor, without any cut of the spectrum (see Fig. 3.11) has an integral ratio with the ideal sech^2 fit function of 66%, a better result than the 46% of the AC trace with the two filters and no cut (Fig. 3.6).
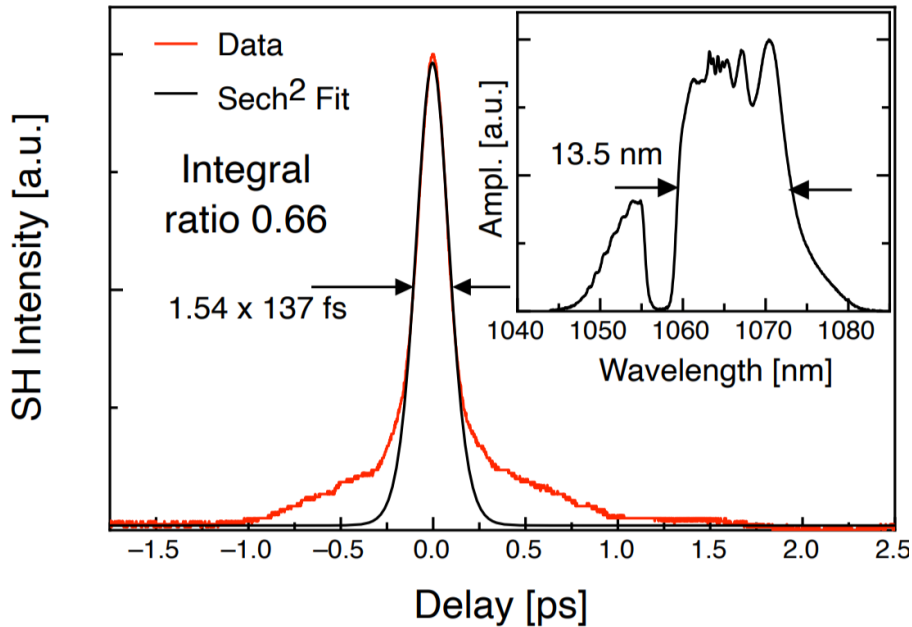

FIGURE 3.11: Autocorrelation trace of the pulse (black line) and sech^2 fit (red line). Inset: output spectrum.

2nd step: 1-m-long Yb-doped fiber and 10-MHz pulse repetition rate

Given the problems seen in the previous section due to the un-absorbed pump power, the Yb-doped active fiber was lengthened by 20 cm. In addition, to increase the pulse energy, we decided to reduce the repetition frequency of the pulse train to 10 MHz by adding 3 m of passive fiber in the oscillator. The results obtained with these modifications are

excellent. As shown in the characteristic reported in Fig. 3.12, the output energy of the resonator increases up to 4.6 nJ.

Moreover, after the compressor, you can see in Fig. 3.13 b that the ideal $sech^2$ fit is almost superimposed to the measured AC trace with the spectral cut-off, with a pulse duration of 167 fs. The output energy is reduced to 3.5 nJ but the quality of the compressed pulses is significantly improved.

Therefore we can conclude that the best configuration involves spectral filtering given by the combination of the band-pass super-gaussian filter and the grating.
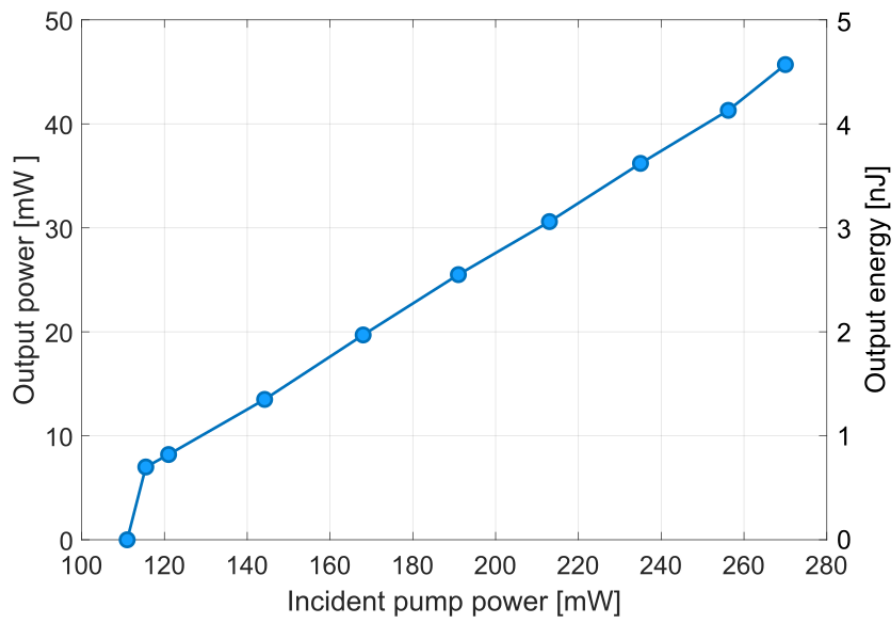

FIGURE 3.12: Mamyshev resonator output power/energy as a function of the incident pump power.
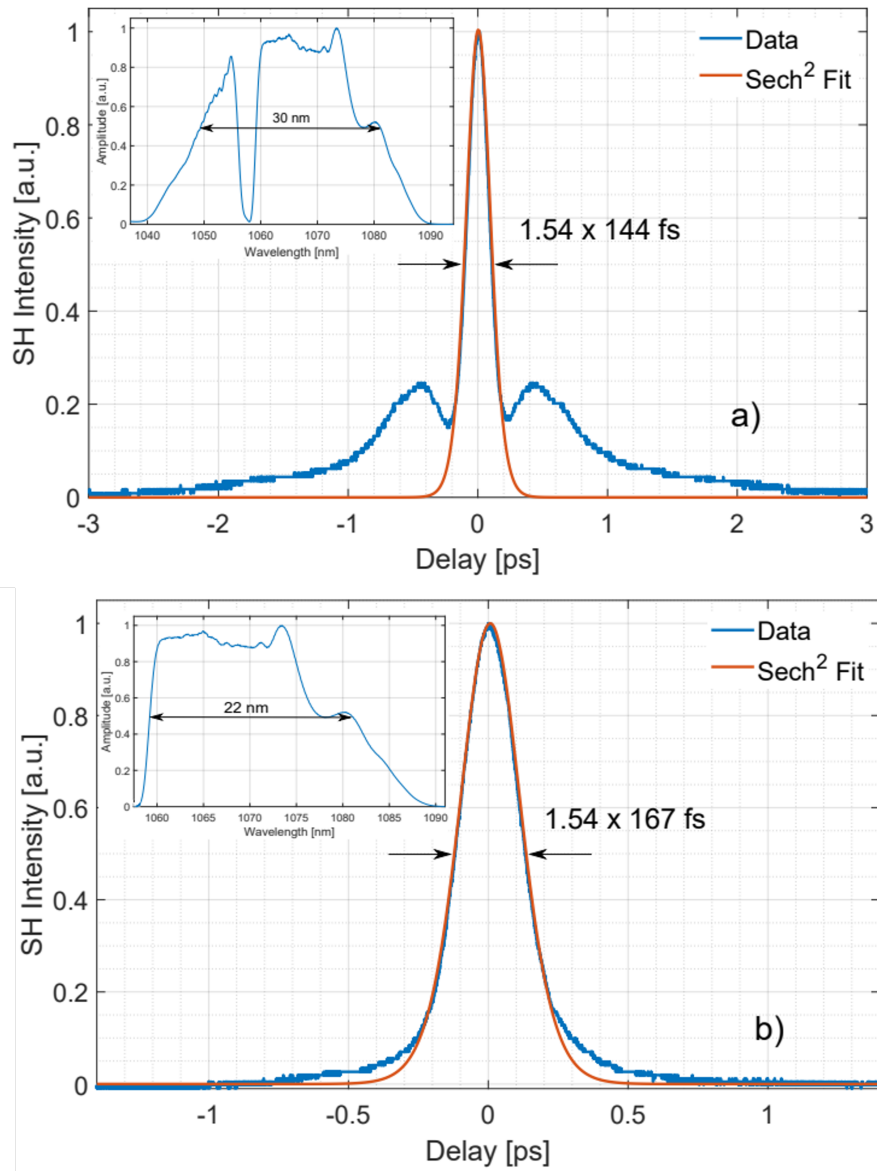
FIGURE 3.13: a) AC trace of the pulse (blue line) and hyperbolic secant fit (red line) without cutting the spectrum (inset). b) AC trace of the pulse (blue line) and hyperbolic secant fit (red line) by cutting the spectrum (inset).

Chapter 4

Mamyshev Oscillator starting techniques

Several papers can be found in literature in which MOs are self-starting if filter bandwidths partially overlap. This allows weak prelasing which starts a pulsed regime that needs to be optimized by increasing, for example, filter separation or in combination with a pulsed pump [17][18]. Other starting techniques have been demonstrated using feedback from an auxiliary arm of the resonator [8][10][19][15][9], but sometimes including a SA or external modulator. Although the research of effective methods for MO self-starting in a fixed, full-yield configuration remains relevant, it is also desirable to find simpler, totally reliable and possibly inexpensive external seeders. When there is no filter overlap to allow weak prelasing, the most reliable starting technique is to use external injection. In this case, gain-switched laser diodes are used, with pulse duration of a few picoseconds [9], or CW mode-locked lasers, with pulse duration up to a few tens of picoseconds [8][20]. However, these can be complex solutions to implement.

In this Chapter, I will present studies on the energy and bandwidth characteristics required for the seeder pulse to successfully initiate the Mamyshev oscillation. Two different types of seeder were tested: an in-house-made master oscillator fiber amplifier (MOFA) and a low-cost, commercially available, passively Q-switched microchip laser. The seeding experiments refer to the setup of the MO with the two BPFs shown in section 3.2.

4.1 First configuration: MOFA seeder

The basic idea of this seeding method is to inject in the MO cavity a pulse with a bandwidth and peak power already sufficient to be broadened enough by SPM, to start the mode-locking regime, as reported in [8]. For this purpose, to start the pulse generation, the Mamyshev cavity was seeded by a passively mode-locked fiber oscillator and amplifier designed and built in the Laser Source Laboratory. The mode-locking operation was induced by a SESAM and stabilized in the normal dispersion regime thanks to spectral filtering produced by a fiber Bragg grating (FBG) combined with intracavity SPM [21]. It provides 12-ps pulses with a repetition frequency of approximately 22 MHz. The seeder had a spectral width $\Delta\lambda \approx 1.35$ nm at the maximum pump power (see Fig. 4.1, blue line). To further increase the bandwidth of the pulses, we exploited SPM by adding 12 m of polarization-maintaining single-mode fiber (PM-SMF, Nufern, PM980-XP) at the end of the MOFA. Fig. 4.1 highlights the broadening of the spectrum obtained at the output of 12 m of passive fiber (orange line). Further increase of the length of the passive fiber was not beneficial due to the onset of the Raman effect. The maximum spectral width was 3.25 nm and the pulse duration was only slightly increased to 14.5 ps.
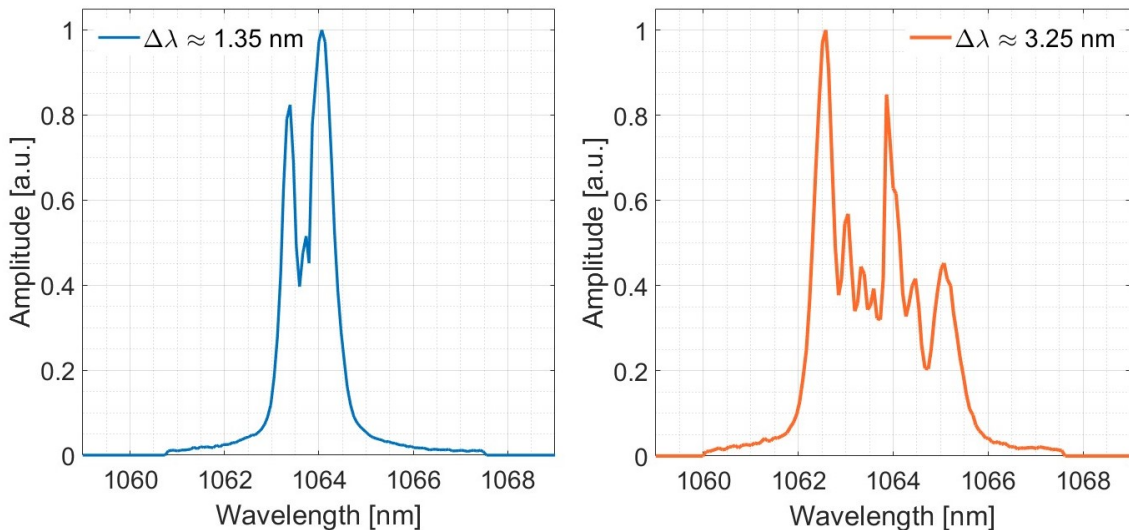

FIGURE 4.1: Seeder spectra at the maximum amplification current of 820 mA. Blue line: output spectrum without passive fiber. Orange line: output spectrum after adding 12 meters of passive fiber. The shaded area represents 50% of the total area of the spectrum.

In order to investigate the possible role of the seeder pulse repetition rate in starting the MO, and to possibly test a "single pulse" seeding, we built the setup shown in Fig. 4.2.
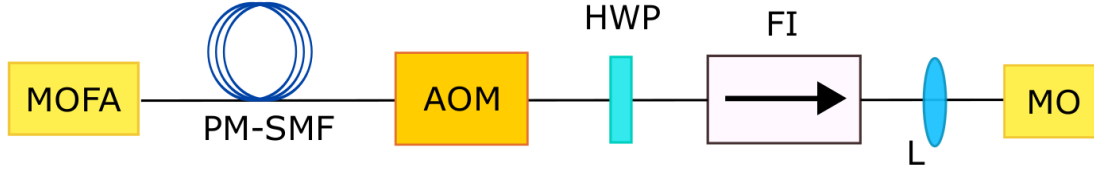

FIGURE 4.2: Setup of the MOFA seeder injection in the MO.

The average power available after the chain of optics, isolator, and Acousto Optical Modulator (AOM), is about 24 mW, corresponding to an energy per pulse of about 1.1 nJ. By introducing a pulse-picking stage made of an AOM driven by a signal synchronized with the ML pulse train, I was able to control the pulse repetition rate of the seeder, while leaving the energy per pulse substantially unchanged. In these conditions, I evaluated the energy required to trigger the Mamyshev oscillation, as a function of the repetition frequency for various bandwidths of the seed pulse ($\Delta\lambda \approx 3.2$ nm, $\Delta\lambda \approx 2.15$ nm, $\Delta\lambda \approx 1.3$ nm and $\Delta\lambda \approx 0.7$ nm). I was able to control the spectral width of the seeder pulses by decreasing the current of the amplifier stage of the MOFA. The results are shown in Fig. 4.3.

As you can notice in the graph, the energy required to start the Mamyshev oscillation is relatively small: the minimum value is $E_{th,min} = 16$ pJ for $\Delta\lambda \approx 3.2$ nm. A trend appears in the curves: for seed pulse repetition frequencies below 1 MHz, the threshold energy does not depend on the repetition frequency of the seeder pulse train. For repetition frequencies greater than 1 MHz, the seed pulse energy required to start the MO grows rapidly. Furthermore, it is observed that the larger the spectral width, the lower the energy needed to trigger the Mamyshev oscillation. At $\Delta\lambda \approx 0.7$ nm (yellow line) I was able to register only two measurements: reducing the amplifier current of the MOFA to reduce the spectral width, the maximum available energy dropped to about 0.2 nJ, insufficient to trigger the Mamyshev at high frequencies.
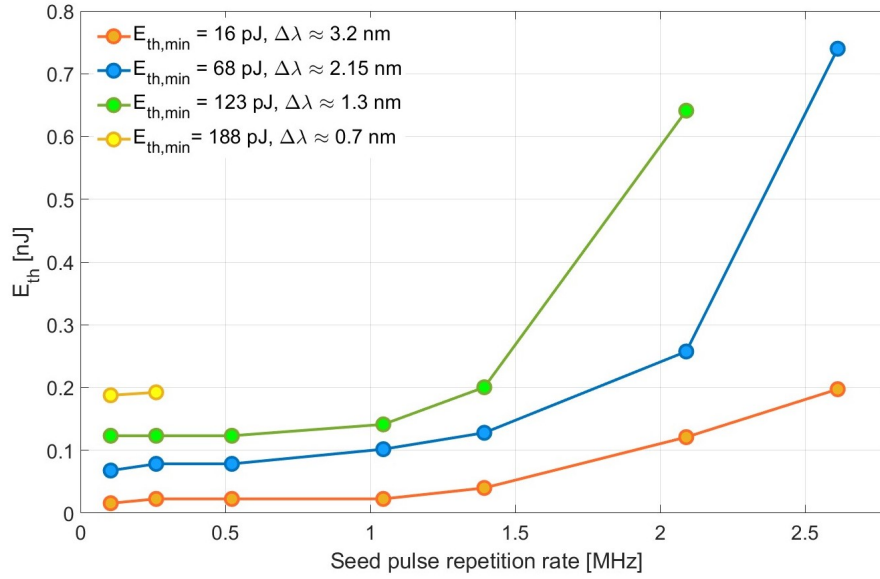
FIGURE 4.3: Seed pulse energy required to start the MO as a function of the seeder repetition frequency for different seeder pulse spectral widths. $E_{th,min}$ is the minimum energy necessary to trigger the MO.

To investigate the threshold at lower frequencies, I positioned a filter with T = 10 % before the half wave-plate in order to decrease the incident energy (see Fig. 4.2). In these conditions, I measured the threshold energy as a function of the seed pulse repetition frequency, for the seeder pulse spectral width of 3.2 nm. The curve is shown in Fig. 4.4, where the frequencies are represented in log scale. The minimum repetition frequency is about 10 kHz. As evident from the figure, the curve is almost flat for frequencies lower than 1 MHz.

A MOFA seeder has the advantage of achieving high gain and output power with high efficiency. In addition, high beam quality is achieved. However, given the studies reported in this section, high energy levels are not necessary to trigger the Mamyshev oscillation. In addition, the MOFA configuration is rather complex to implement and relatively expensive. For this reason, we decided to explore a different and innovative technique.
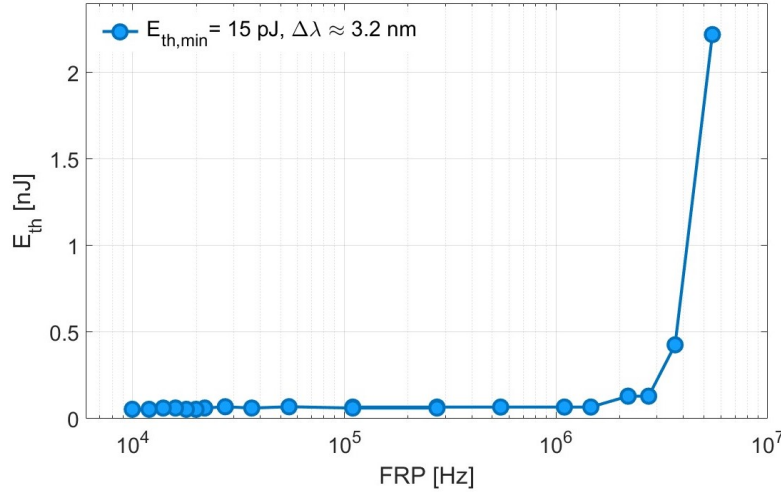
FIGURE 4.4: Threshold energy of the seeder to start the Mamyshev oscillation as a function of the seeder repetition frequency at $\Delta\lambda \approx 3.2$ nm. The horizontal axis is in log scale.

4.2 Second configuration: passively Q-Switched microchip laser

The results with the MOFA seeder were excellent, but in order to use a simpler seeder source, I investigated the use of diode-pumped solid-state sub-nanosecond passively Q-switched microchip laser (PQS-MCL) at 1 μm. For the experiments, we choose the microchip model FP2-1064-1-55 (Bright Solutions Srl), with a pulse repetition frequency FRP $\approx$ 55 kHz, a pulse duration $\tau_p \approx 300$ ps, a pulse energy E ≈ 1.5 μJ, with a single longitudinal mode (SLM) pulse emission. The corresponding pulse peak power is about 5 kW at the output of the PQS laser. The beam is almost diffraction limited ($M^2 < 1.5$) and linearly polarized. Given the SLM nature of the pulses, assuming a Gaussian temporal profile, one should expect a $\Delta\lambda \sim 6$ pm, well below the ~ 20 pm resolution of our ANDO AQ6317B optical spectrum analyzer we had in our lab (see Fig. 4.5)

In this second seeding configuration you can observe that the bandwidth is about 3 orders of magnitude smaller than in the previous case ($\Delta\lambda_{MOFA} \sim 3.2$ nm, $\Delta\lambda_{MCL} \sim 6$ pm), and the pulse duration is 20 times longer ($\tau_{p,MOFA} \approx 14.5$ ps, $\tau_{p,MCL} \approx 300$ ps).

Knowing that spectral broadening by SPM is proportional to peak power and inversely proportional to pulse duration, pulses longer than a few tens of picoseconds are
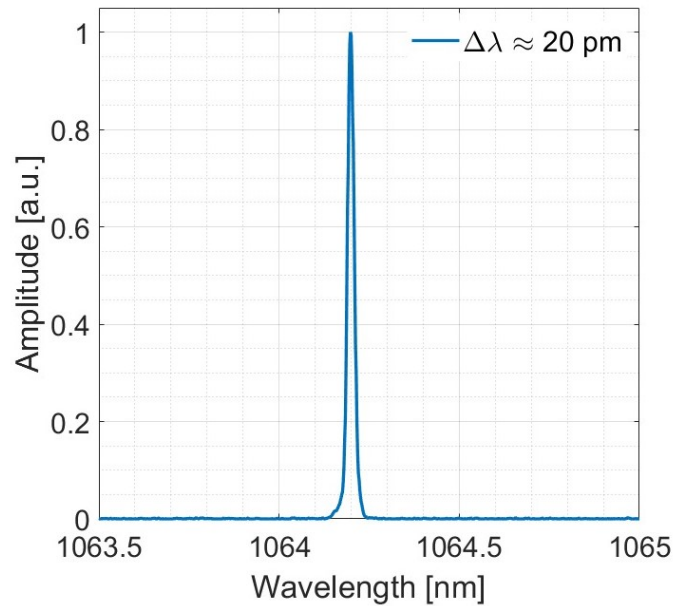
FIGURE 4.5: Microchip spectrum as measured by ANDO AQ6317B spectrometer with a maximum resolution of 20 pm.

therefore inefficient to initiate a MO relying on this effect alone. However, not-phase-matched four-wave mixing (FWM) in normal dispersion fibers has been demonstrated to produce relatively broad side-bands of several nm near the pump frequency [22][23], before stimulated Raman scattering (SRS) starts massive spectral broadening. For these reason, in this second configuration, we investigated the FWM non-linear process, for the starting of the MO.

The setup for the experiments shown in Fig. 4.6, is similar to the one reported in the previous section.
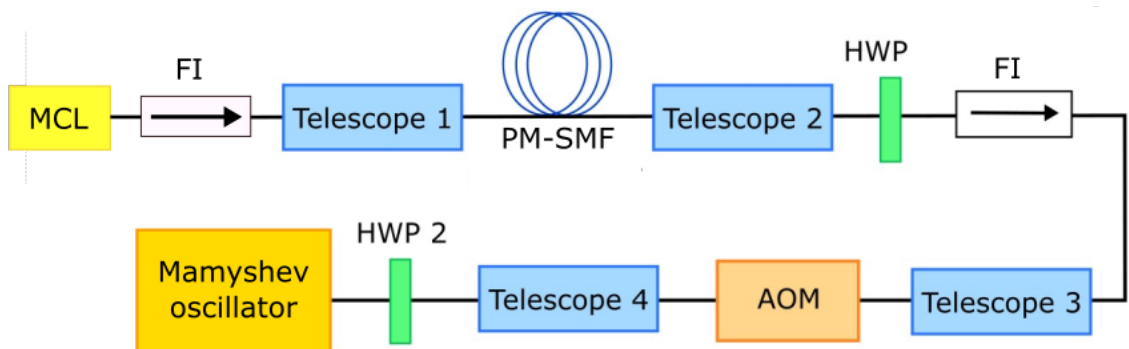

FIGURE 4.6: Setup of the MCL seeder injection in the MO.

We introduced two Faraday isolators (FI) with a maximum transmission of approximately 80% to avoid disturbance to the PQS seeder due to residual reflection at the uncoated surface of the passive fiber we used to broaden the pulse spectrum. An acoustic-optic modulator is used to control the repetition frequency of the seed train pulses from "single shot" up to the maximum repetition rate of 55 kHz. Moreover, in the setup, we could control the energy of the injected seed and the polarization of the seed beam so as to rotate the linear polarization along the principal axis of the fiber. To estimate the length of polarization-maintaining single-mode fiber (PM-980 XP) to add at the output of the PQS microchip laser for effective spectral broadening, we performed some calculations to predict the Raman threshold. The onset of Raman effect, basically fixes the maximum practical length of the passive fiber. We can estimate the length L of the fiber, if we assume that Raman gain, before depletion of the pump become significant, is given by [22]:

$$g = g_r \frac{P_{peak}}{A_{eff}} L \tag{4.1}$$

where $g_r \sim 5 \ 10^{-14}$ mW^{-1} is the Raman gain coefficient of the material (silica glass in our case), L is the length of the PM-SMF and P_{peak} is the peak power of the seeder pulse coupled in the passive fiber. By considering the transmission of 80% of the FI and a coupling efficiency into the PM-SMF of $\sim 55\%$ (measured in the lab), the maximum injected peak power is ~ 2 kW, at 600 nJ of pulse energy. The effective core area A_{eff}, can be estimated as:

$$A_{eff} \approx \pi \left(\frac{MFD}{2} \right)^2 \tag{4.2}$$

where the mode field diameter (MDF) for the PM-980 XP fiber is 6.6 μm from the datasheet. The effective core area results $\sim 3.4 \ 10^{-11}$ m^2.

Starting from quantum noise, the typical value of the gain required to reach a detection threshold of the Raman shifted signal is (see Eq. 4.1) $g \sim 16$ [22].

We can conclude that with few meters of PM passive fiber we should already trigger Raman effect if the PQS seeder has $\sim$ kW peak power coupled in the PM-SMF.

In Fig. 4.7 you can observe the seeder spectrum after the 10 m of PM-SMF by injecting a pulse energy of 300 nJ, corresponding to $\sim$ 1 kW peak power. In this condition, Eq. 4.1 g $\sim$ 16, in fact you can observe the slight contribution of the Raman process: there is a Stokes line at $\approx$ 1100 nm and an Anti-Stokes line at $\approx$ 1030 nm.

The FWHM of the seed spectrum is $\Delta\lambda$ = 180 pm. This broadening is due to the SPM process. The maximum nonlinear phase shift due to the SPM can be estimated by [22]:

$$\phi_{max} = \gamma\, P_{peak}\, L \tag{4.3}$$

where P_{peak} and L are defined as before, while γ is the non-linear fiber parameter defined as:

$$\gamma = \frac{2\pi n_2}{\lambda A_{eff}} \tag{4.4}$$

which depends on the nonlinear-index coefficient of the fiber $n_2 \approx 2.2\ 10^{-20}$ m^{2}W^{-1}, on the seed central wavelength λ = 1064 nm and on the A_{eff} defined in Eq. 4.2. In this case, the value of γ is $3.7\ 10^{-3}$ W^{-1}m^{-1}.

The maximum phase shift ϕ_{max} obtained with the SPM process, with 10 m of passive fiber and a peak seeder power of 1 kW is about 37.

The ratio between the FWHM of the spectrum after the SPM spectral broadening and the bandwidth of the initial spectrum is given by the formula [22]:

$$\frac{\Delta\omega_{SPM}}{\Delta\omega_0} = \sqrt{1 + \frac{4}{3\sqrt{3}}\phi_{max}^2} \approx 32 \tag{4.5}$$

This implies that the spectrum of the seed broadened by SPM in 10 m of passive fiber with a peak power of 1 kW is $\sim$ 30 times larger than the initial one. This estimation is in very good agreement with the experimental results: the ratio of the FWHM of the seed spectrum after the passive fiber ($\Delta\lambda_{10m}$ = 180 pm) to the FWHM of the PQS microchip laser ($\Delta\lambda_0 \sim$ 6 pm) is indeed about 30.
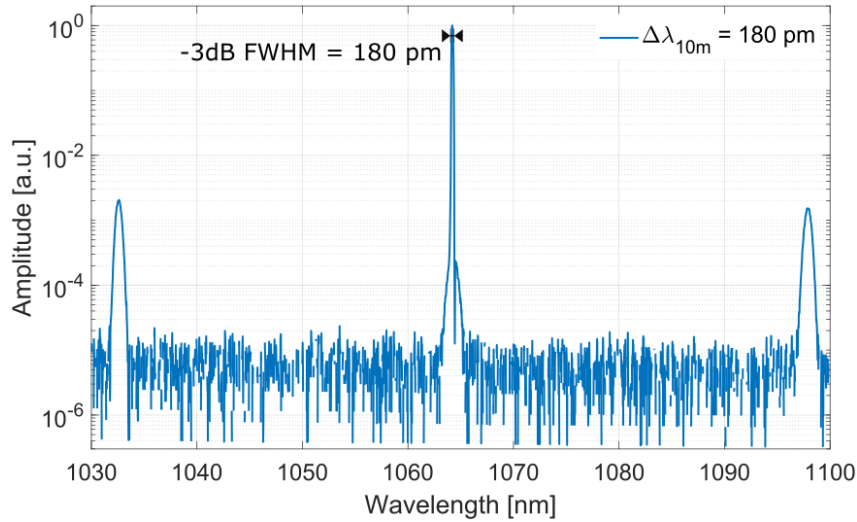
FIGURE 4.7: Microchip spectrum adding 10 m of passive fiber with the
Raman stokes (at ≈ 1100 nm) and the anti-stokes (at ≈ 1030 nm).

In Fig. 4.7, you can also notice that, around the narrow line at 1064 nm, close to the instrument noise level, there is a broadening of the seed pulse spectrum. This is due to the nonlinear Four-Wave Mixing process.

A more detailed investigation of the spectral broadening for FWM of the seeder by varying the pulse energy injected into the PM-SMF is shown in Fig. 4.8. FWM-induced spectral broadening around 1064 nm starts to be detectable at ≈ 400 nJ seed pulse energy (≈ 1.3 kW peak power). As the seed energy increases, the pedestal of the FWM grows rapidly until it broadens to about ± 10 nm around 1064 nm for the injected enegry of 600 nJ (≈ 2 kW peak power). This behavior is in qualitative agreement with experiments reported in [23]. If compared to [23], the use of a longer fiber (10 m versus 3.5 m) resulted in a slightly narrower spectral broadening for FWM, as it reduced the phase-matching bandwidth of the FWM process. Moreover, our experimental results are in fair agreement with numerical simulations based on the analytical solution of the generalized nonlinear Schrödinger equation that includes the effects of dispersion and Raman scattering [24].

The inset in Fig. 4.8 shows the seed spectral broadening over a larger span, which includes the contribution of Stimulated Raman Scattering (SRS) which is clearly very significant at the maximum seed energy of 600 nJ.

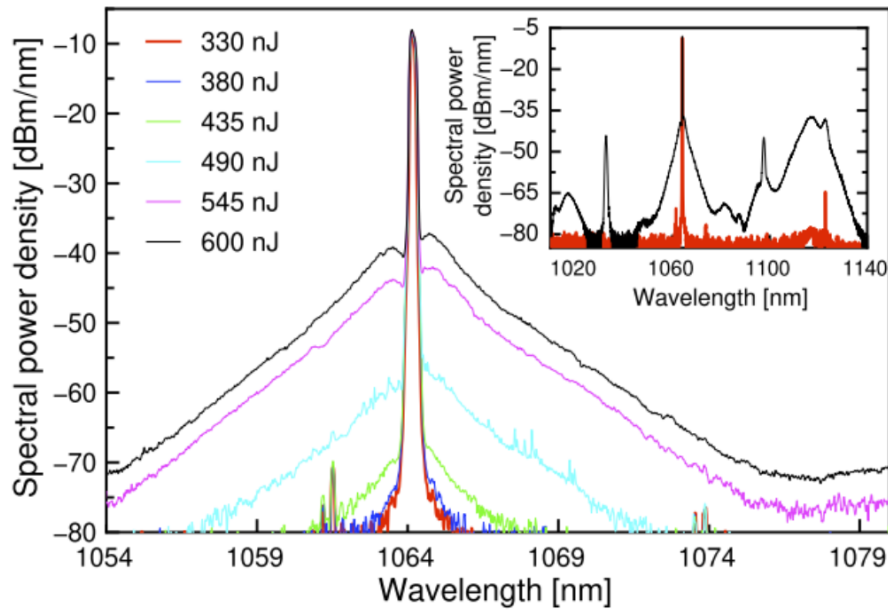In order to test the effectiveness of the seeder in initiating the MO, I used an AOM to

FIGURE 4.8: FWM-induced seeder spectrum broadening in 10-m-long PM-SMF for different values of pulse energy. Inset: spectrum broadening over a larger span including the SRS.

control the pulse repetition frequency of the seeder. During the early stage of the experiments, we noticed that even a single seed pulse with adequate energy was sufficient to start the MO. However, due to the inherent jitter of the PQS laser, the deflection window of the AOM could not be synchronized with the pulse train of the seeder. Therefore, to ensure the presence of at least one seed pulse, I created a deflection window of 50 μs (about 2 pulses). After the optical chain in Fig. 4.6, the FI, and the AOM, the maximum pulse energy available to seed the MO is ~ 250 nJ, which corresponds to a peak power of ~ 0.9 kW. I tested the effectiveness of the MCL as seeding at four different levels of the MO diode pump power. For each power level, I varied the energy of the seeding pulse injected into the MO and collecting 200 measurements for each experimental point. The results for this test are reported in Fig. 4.9.

The results suggest that a range of energies that ensures the start of the oscillation exists. In particular, at the maximum tested diode pump power of 193 mW (green line), I always got 100% success for injected energies > 30 nJ. By decreasing the pump power you can notice a slight decrease in the incident energy range. However, even in the worst
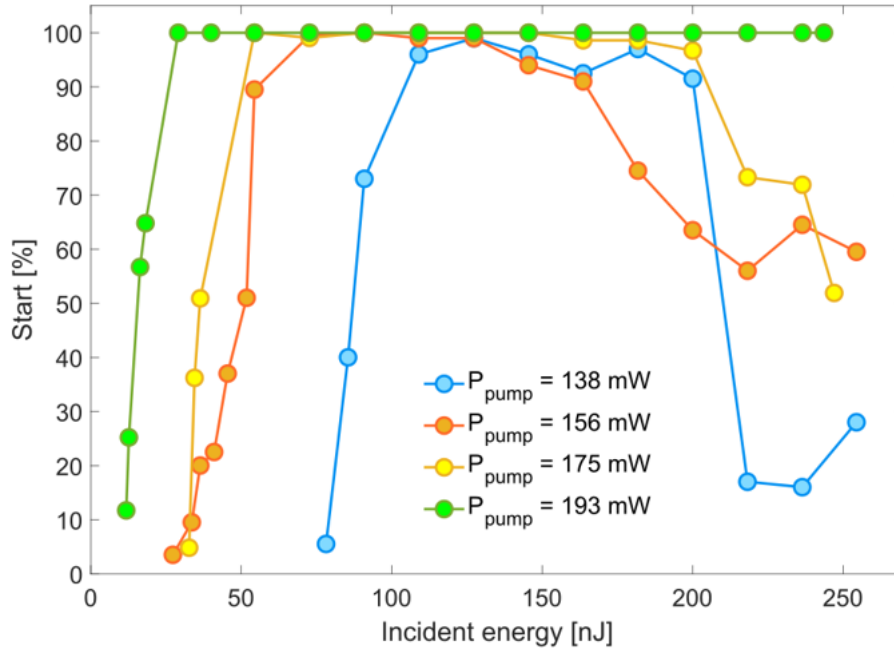
FIGURE 4.9: Mamyshev oscillation starting statistic at different pump currents.

case (blue line) the energy range that ensures a starting is from 100 nJ to 200 nJ.

Given the excellent results of the previous experiment, we decided to test a seeding configuration that did not involve the use of PM-SMF, thus directly injecting the pulses emitted by the PQS microchip laser into the MO, making the setup simpler.

In this case, FWM spectral broadening occurs exclusively in the passive and active fiber of the MO. Under these conditions, seeding was successful in starting the mode-locking only operating near the maximum available pump power and using the full energy of the seeder pulse. However, this clearly exposes the MO to a higher risk of optical damage. Nevertheless, we can expect that by optimizing the length of the different fiber sections, MO will reliably start at lower seeding energy when injected directly from the PQS seeder, thus eliminating the external fiber, and reducing its cost and complexity.

To asses the contribution of the FWM sidebands in starting the MO, we employed a Lyot filter in combination with a band-pass filter, identical to that used in MO setup, to selectively suppress the 1064 nm peak of the seeding pulse, broadened by the FWM process. In Fig. 4.10, the black curve represents the seeder spectrum before filtering, while
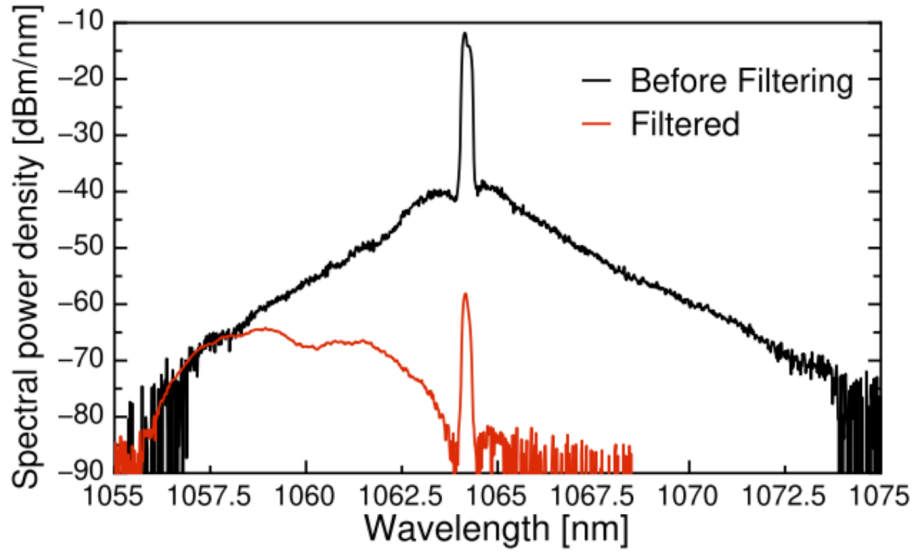
FIGURE 4.10: FWM-broadened spectrum of the seed pulse before (black line) and after (gray line) selective filtering.

the red curve represents the seeder spectra after filtering still effective to successfully initiate the MO. By numerical integration of this spectrum, we estimated that its FWM sideband contained > 85 % of the total energy, $\sim$ 100 pJ, proving the crucial role played by the FWM effect to enable the MO starting.

4.3 Physical picture of the MO starting mechanism with FWM

In case of the first seeder I tested, the picosecond MOFA seeder, the starting mechanism of the MO is quite clear: since the picosecond pulse injected in the MO already has enough peak power to enable significant SPM in the passive and active fiber of the MO, the ML regime is established. The physical picture is quite different in the second case, when we demonstrated the starting of the MO employing SLM, sub-ns pulses from a PQS microchip laser.

To better figure out what is going on during the starting of the MO in this latter case, we can assume that FWM originates from random noise fluctuations obeying a Gaussian statistics, as in [25]. These fluctuations originates within the gain bandwidth of the FWM, which is fixed by the phase matching condition along the fiber, and we can call

$\Delta \nu_{FWM}$. Within this bandwidth we can define an average power $\overline{P}$ in the time interval corresponding to the Fourier-limited PQS pulse duration ($\tau_0 \sim 300$ ps) and following [25], we can estimate the average number of fluctuations that randomly present a power $P > \eta \overline{P}$ (with parameter $\eta > 1$), and their duration as

$$\overline{N} = \Delta \nu_{FWM} \sqrt{2\eta} e^{-\eta} \tag{4.6}$$

$$\overline{\tau} = \frac{1}{\Delta \nu_{FWM} \sqrt{2\eta}} \tag{4.7}$$

The value of η to estimate the more intense fluctuation can be obtained if we ask that within a PQS pulse duration τ_0, only a single fluctuation exists, being the average time interval between different fluctuations equal to

$$\overline{\Delta t} = \frac{1}{\Delta \nu_{FWM} \sqrt{2\eta}} (e^\eta - 1) \sim \tau_0 \tag{4.8}$$

Now, since the FWM is significantly broader than the original spectrum of the SLM PQS pulse, $\Delta \nu_{FWM} \tau_0 \gg 1$, and one obtains $\eta \sim \ln m$, with $m = \Delta \nu_{FWM} \tau_0 \sim 400$ for a $\Delta \lambda_{FWM} \sim 5$ nm as in Fig. 4.10 and $\tau_0 = 300$ ps.

In this way, it is possible to estimate the peak power P_f, pulse duration τ_f, and energy E_f, provided by the most intense FWM temporal fluctuation [26].

$$P_f \sim \frac{E_{FWM}}{\tau} \ln m \tag{4.9}$$

$$\tau_f \sim \frac{1}{\Delta \nu_{FWM} \sqrt{\ln m}} \tag{4.10}$$

$$E_f = P_f \tau_f \sim E_{FWM} \frac{\sqrt{\ln m}}{\Delta \nu_{FWM} \tau} \tag{4.11}$$

By considering the red curve in Fig. 4.10, we can assume a bandwidth $\Delta \lambda_{FWM} \sim 5$ nm. From our measurement, its energy content $E_{FWM} \sim 100$ pJ, and the microchip seed pulse duration $\tau \sim 300$ ps, resulting in $P_f \sim 2$ W, $\tau_f \sim 300$ fs, and $E_f \sim 0.6$ pJ. In the first

half roundtrip in the MO, the FWM fluctuation peak power P_f is not enough to trigger significant spectral broadening through SPM and it is only temporally is stretched by dispersion to $\tau_f \sim 1$ ps. The SPM becomes relevant after double-pass amplification in the active fiber of the MO and subsequent propagation in the passive fiber. Given the small-signal gain of the single-pass amplification in our low-power oscillator $G_0 \sim 10$, we have a double-pass unsaturated gain $G_0^2 \sim 100$. To estimate the fluctuation energy E_f required to trigger the MO mode-locking regime, we can ask that the spectral broadening $\Delta\lambda_0$ (or $\Delta\nu_0$ in the frequency domain) is large enough to create a contribution within the transmission bandwidth of the offset filter in the MO.

Given a propagation along a fiber of length L of the amplified FWM fluctuation, we calculate from SPM:

$$\Delta\nu_0 \sim \frac{8n_0n_2L}{\lambda}\left(G_0^2\frac{E_f}{A\tau_f}\right)\frac{1}{\tau_f} \tag{4.12}$$

or equivalently for the fluctuation energy as a function of the filters wavelength offset $\Delta\lambda_0$

$$E_f \sim \frac{Ac\tau_f^2\Delta\lambda_0}{8n_0n_2\lambda LG_0^2} \tag{4.13}$$

where A ~ 2.3 x 10^{-7} cm^2 is the fiber core area, $n_0 \sim 1.5$ and $n_2 \sim 2.2$ x 10^{-16} cm^2/W are the linear and nonlinear refractive indices respectively, and L ~ 5 m is the length of the passive fiber of the MO, with the amplifier in the middle. For a filters offset $\Delta\lambda_0$ ~ 10 nm, we obtain E$_f \sim 0.5$ pJ, in fairly good agreement with the fluctuation energy calculated from Eq. 4.11 from the measured FWM spectrum that successfully started the oscillator

This model explains the experimental observations that successful starting of the MO is obtained in a relatively wide range of seed energies. The success rate (see Fig. 4.9) has a relatively broad plateau then it decreases at high seed energy. One possible explanation of this behaviour is that the unfiltered multi-pulse seed residual at 1064 nm, which was injected for simplicity with the FWM signal and is rejected in the first round trip, is responsible for the undesired nonlinear optical effects that affect MO steady state oscillation.

Moreover, since strong absorption saturation occurs in the active fiber, when the pump power is increased, G_0 remains almost constant. However, the plateau extends progressively toward lower seed , since with higher circulating pulse energy, oscillation becomes increasingly insensitive to perturbations, starting with smaller seed energy.

Chapter 5

Chirped pulse double-clad fiber amplifier

In this chapter, I will introduce the chirped pulse amplification (CPA) and the reasons why it is useful for ultrashort pulses. Then, I will present the CPA results obtained from the MO pulses reported in Chapter 3, subsection 3.4. In addition, I will show how the whole setup was realized in order to be reasonably compact and modular. This was necessary to allow me to transport the laser and perform the experiments on optical parametric generation described in Chapter 6 at the Institute of Photonic Sciences (ICFO), in Castelldefels, Spain.

5.1   CPA working principle

The chirped pulse amplification is a technique for amplifying ultrashort pulses to high optical intensities, up to terawatt or petawatt level, while avoiding unwanted nonlinear optical effects or optical damage in the gain medium [27].

As you can see from Fig. 5.1, CPA is logically divided into three phases: stretching, amplification, and re-compression.

In the first stage, pulses are chirped and temporally stretched to a longer pulse duration by means of dispersive elements, such as gratings, prisms, etc. This decreases the peak power of the pulses that will then be amplified, thus making optical damage or unwanted nonlinear optical effects less relevant in the amplification medium.
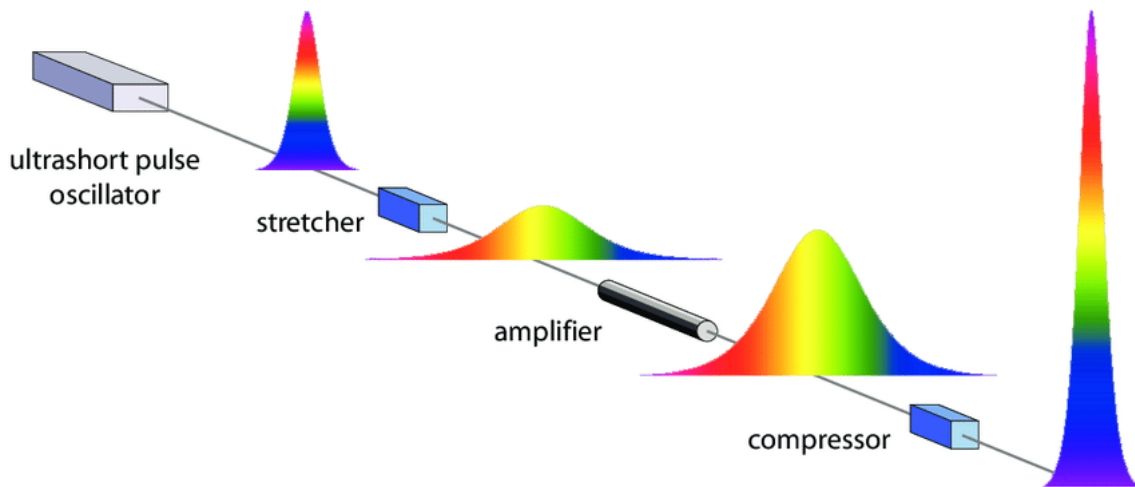
FIGURE 5.1: Chirped pulse amplifier scheme.

The second phase is the amplification itself, in which the pulses pass through a pumped active medium to increase their energy.

The third and final stage, compression, also involves the use of dispersive elements to compress the amplified pulses, but the dispersion must be of the opposite sign with respect to the stretcher one. There is usually positive dispersion in the stretching and negative dispersion in the compression, where higher powers are involved.

5.2 Experimental results

In Chapter 3, I showed how we realized a MO capable of generating 3.5-nJ pulses compressible to a minimum duration of 170 fs, with a clean (almost pedestal-free) AC trace thanks to the cut-off of the blue part of the spectrum. Tab.5.1 summarizes the main features of the MO.

Mamyshev Oscillator Features	
Average Power	35 mW
Pulse Energy	3.5 nJ
Spectral bandwidth	22 nm
Central wavelength	1067 nm
Repetition Rate	10 MHz
Pulsewidth before stretching/compression	~ 5 ps

TABLE 5.1

The ultimate goal for the realization of this laser is to obtain a pulse energy of several tens/hundreds of nJs with pulse duration possibly below ~ 200 fs. Therefore, a CPA was employed in view of the advantages outlined in the previous section. The scheme of the realized CPA is shown in Fig. 5.2.
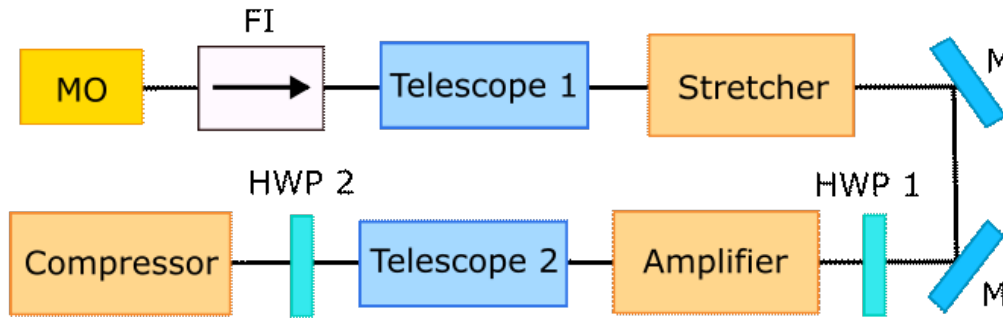

FIGURE 5.2: Setup of the CPA.

A Faraday isolator with $\sim 90\%$ transmission is used between the low-power oscillator and the CPA to avoid back reflections and disturbance of the MO. Two properly designed telescopes were used to re-size the laser beam to a beam waist $w \sim 1$ mm, while the half wave plate (HWP1) was used to rotate the polarization of the beam to match the amplifier PM double clad fiber fast axis. The other half-waveplate HWP2 was used to optimize grating pulse compressor efficiency by accommodating the linear polarization of the amplified beam along the direction parallel to the grating grooves. We now analyze in details all the three building blocks of the CPA.

5.2.1 Stretcher

The dispersive pulse stretcher was made with a single transmission grating in the Martinez folded configuration [28], hence with a total number of 4 bounces on the grating, to obtain positive second-order dispersion. In Fig. 5.3 it is shown the setup implemented. In detail:

- The beam coming from the MO is reflected by mirror M_1 (HR 45°) and passes through the grating for the first time (red arrow).

- The beam transmitted by the grating, travels trough the lens L (f = 100 mm) offset with respect to the center of the lens, as shown in the figure: this allows the beam to be deflected, so that, after reflection from the mirror M_2 (HR 0°), returns to the lens shifted with respect to the initial position and then travels through the grating a second time (green arrow).

- After being transmitted for the second time, the beam is shifted vertically by means of a right angle prism, thus going through the grating for a third time (blue arrow) in the same horizontal position with respect to the second bounce, but in a different vertical position.

- At this point, the beam retraces its path until it returns for the fourth time on the grating (yellow arrow). Now the beam passes above the mirror M_1 and goes to mirror M_3 to be re-directed towards the amplifier (black dotted line).
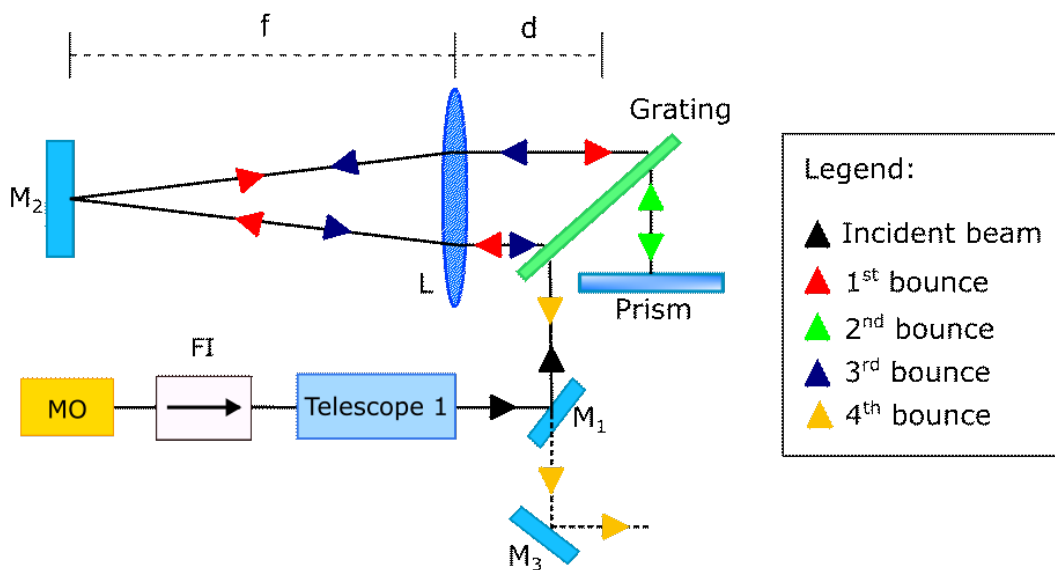

FIGURE 5.3: Setup of the stretcher.

In the Martinez configuration the distance between the lens L and the mirror M_2 must be equal to the effective focal length of the lens (f = 100 mm), so that the focal plane of L coincides with the mirror M_2. If the distance d between the grating and the lens L is equal to the focal length of the lens ($d = f$), the stretcher add no dispersion, if this

$d > f$ it adds negative dispersion, if $d < f$ it adds positive dispersion. In our case, the distance between L and the grating is of few mm, in order to exploit the maximum possible positive dispersion achievable with the stretcher of about 80 ps^2. The grating (1200 grooves/mm) has a transmission $T_{max} \sim 85\%$, which means that in four passes $T_{4P} \sim T_{max}^4 \sim 52$ %. If we add losses from the mirrors, lens and right-angle prism, the overall transmission of the stretcher is about 45%. The capability to cut the spectra, to improve the quality of the compressed pulses, occurs at this stage. The main features of this first step, with the cutoff of the blue part of the MO spectrum, are reported in Tab.5.2.

Mamyshev oscillator + Stretcher Features	
Average Power	14 mW
Pulse Energy	1.4 nJ
Spectral bandwidth	10 nm
Pulse Repetition Rate	10 MHz
Pulsewidth after stretching	> 50 ps

TABLE 5.2

Fig. 5.4 shows the AC trace of the stretched pulse. The delay line of the commercial AC we had at our disposal in the lab was not long enough to permit a precise measurement of the stretched pulse duration, but it is clear that it is > 50 ps.
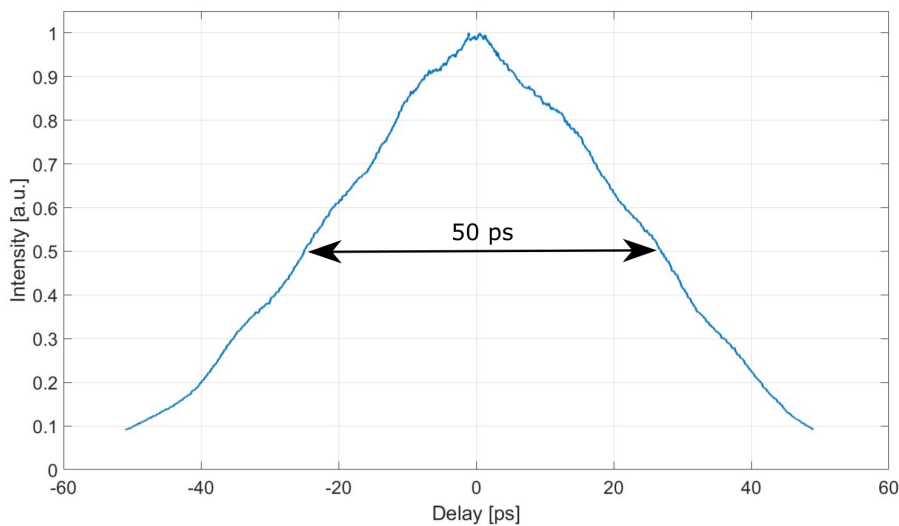

FIGURE 5.4: Autocorrelation trace of the stretched pulse.

5.2.2 Amplifier

The amplification stage consists of a 2-m-long, diode-pumped, Yb-doped, PM, double-clad large mode area (MDF = 10 μm) fiber in a counter-propagating configuration. This means that the seed travels in the opposite direction with respect to the pump inside the active fiber. The ends facets of the active fiber were cut at an angle of about 6° to prevent self-lasing. The setup employed is shown in Fig. 5.5.
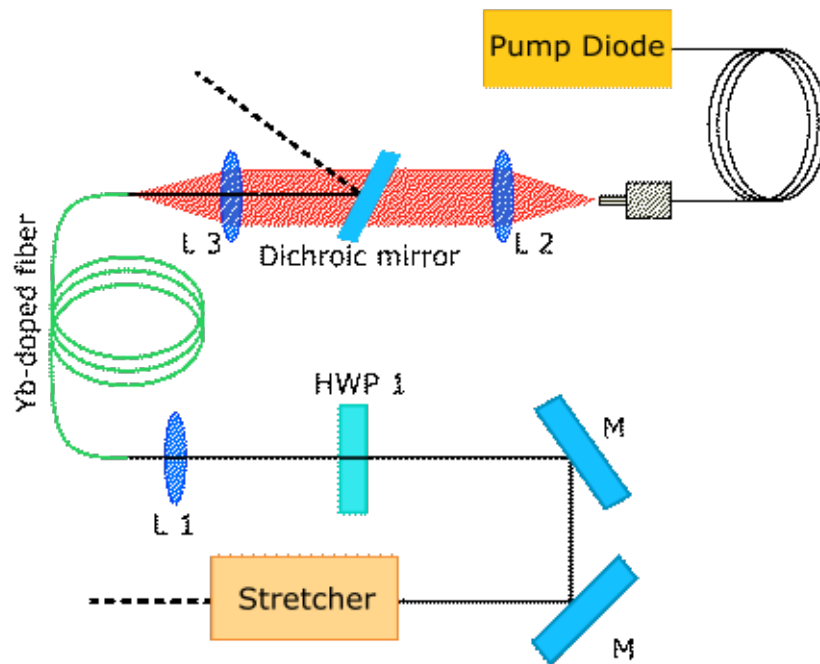

FIGURE 5.5: Setup of the amplifier.

The seeder beam coming from the stretcher passes through an the half-wave plate HWP 1 to accommodate the linear polarization of the seed to be parallel to the Yb-doped fiber slow axis. It was then focused in the active fiber by means of the L1 lens (f_1 = 11 mm), to obtain a good mode-matching with the large mode area fiber core. The pump unit is a fiber-coupled (NA = 0.22 and $\varnothing$ 105 μm) laser diode with a maximum output power of 6 W at 976 nm. The characteristic of the laser diode output power as a function of the diode driving current is reported in Fig. 5.6. The wavelength of the pump diode was temperature-tuned by means of a Peltier thermo-electric cooler.

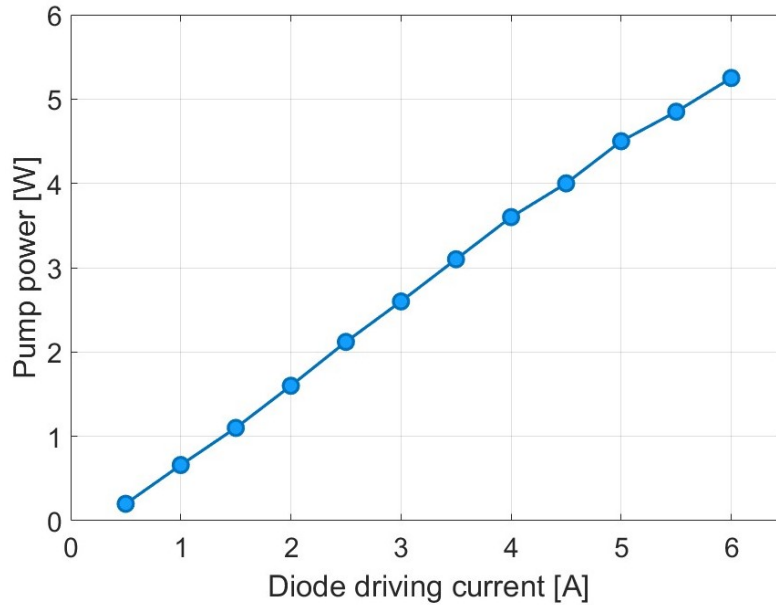The L2 lens in the setup (f_2 = 11 mm) collimates the pump beam out of the diode fiber,

FIGURE 5.6: Diode output power as a function of the diode driving current.

while the L3 lens (f_3 = 11 mm) focuses it into the active fiber, moreover the L3 lens is used to collimate the amplified laser beam out of the LMA fiber. The dichroic mirror (HR: 1000 - 1100 nm, HT: 900 - 980 nm) is used to transmit the pump (976 nm), while reflecting the amplified seed and direct it towards the compressor.

The characteristic of the output power from the amplifier as a function of the diode pump power is shown in Fig. 5.9, blue line. In this second stage of the CPA we reach a maximum average output power of 1.8 W, corresponding to a 180 nJ. A reasonable preservation of the linear polarization of the seed is also obtained in the PM LMA active fiber; in fact we measured a ratio between the two principal axis of 13:1. Neither a significant contribution of ASE, nor a spectral distortion of the seed pulse was observed in the amplifier.

5.2.3 Compressor

Eventually, there is the pulse compression stage. It was realized with a single transmission grating (Edmund optics, 1000 grooves/mm, design wavelength 1040 nm) in a folded (four-bounces), Tracy configuration. In this stage, a negative dispersion is added to the pulse to re-compress it. The setup implemented for the compressor is shown in Fig. 5.7.
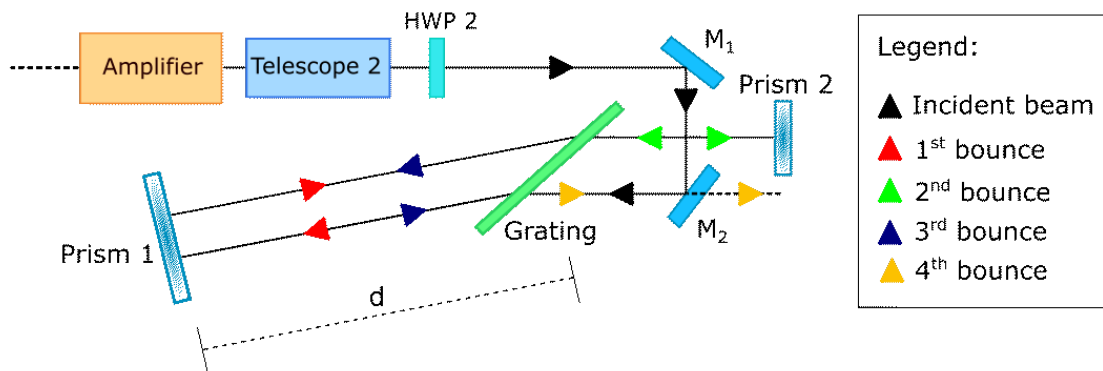

FIGURE 5.7: Setup of the compressor.

The beam coming from the amplifier passed through a telescope in order to be collimated with a beam radius of ~ 1 mm. The HWP 2 is used to rotate the polarization of the beam to match the maximum transmission efficiency of the grating (E-field parallel to the grating grooves). The d represents the average distance between the grating and Prism 1. For what concerns the compressor itself it was realized in this way:

- The incoming beam (black arrow) is reflected by means of the M_2 mirror to be transmitted by the grating for the first time (red arrow, first bounce).

- The beam is then horizontally shifted thanks to Prism 1, in order to go through the grating for the second time (green arrow) in a laterally shifted with respect the first bounce.

- The beam transmitted is then vertically shifted by means of Prism 2. In this way, the beam can go through the grating for the third time (blue arrow).

- at the end, the beam is reflected back by means of Prism 1 and can be transmitted by the grating for the last time (yellow arrow). The beam now is above the incoming beam (black line) and can continue its path without impinging on M_2 mirror.

Prism 1 was mounted on a transitional stage to vary the distance d and, consequently, also the dispersion of the compressor, so as to obtain the shortest possible pulse duration of 200 fs FWHM, in a clean $sech^2$ pulse intensity profile (see Fig.5.8) with a time-bandwidth product ~ 0.5. This occurs when the average distance d is ~ 36 cm, which corresponds to a second-order dispersion of about $\sim$ - 2.4 ps^2. No instabilities were noted in either the autocorrelation trace or the spectrum output from the chirped pulse amplifier.
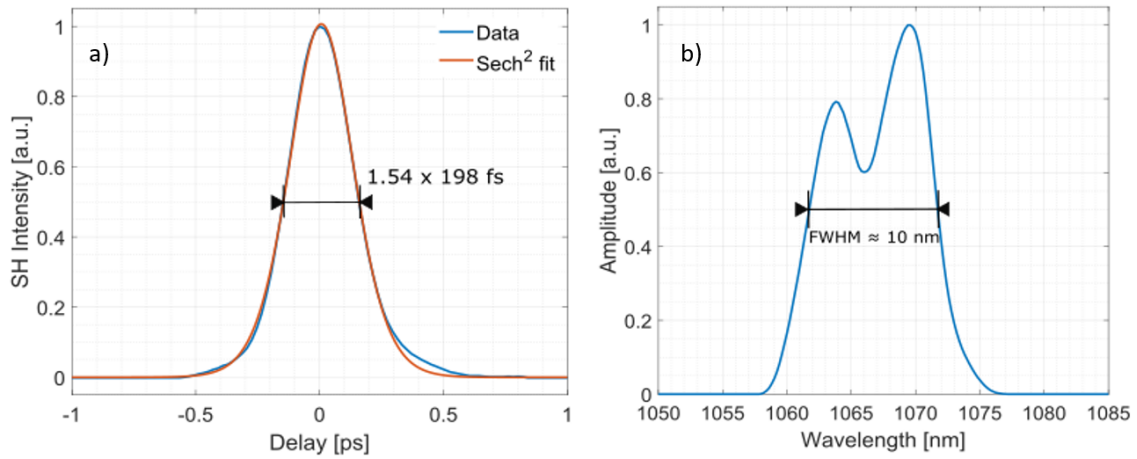

FIGURE 5.8: Autocorrelation trace (a) and spectrum (b).

The grating used in the compressor has a nominal maximum transmissivity of T_{max} $\sim 94\%$, which means that ideally, in 4 passes, $T_{4P} \sim T_{max}^4 \sim 78\%$. However, the overall efficiency of the compressor depends also on the transmission/reflection properties of telescope, lenses, waveplates and prisms used in the setup and we obtained a maximum overall transmission efficiency of about 60%, enough to reach a pulse energy after compression of 100 nJ. Fig 5.9 shows the compressor (red line) output powers as a function of the diode pump power in the amplifier.

Comparisons with the compressed pulses obtained before the amplification stage showed that CPA did not affect significantly the minimum pulse duration.
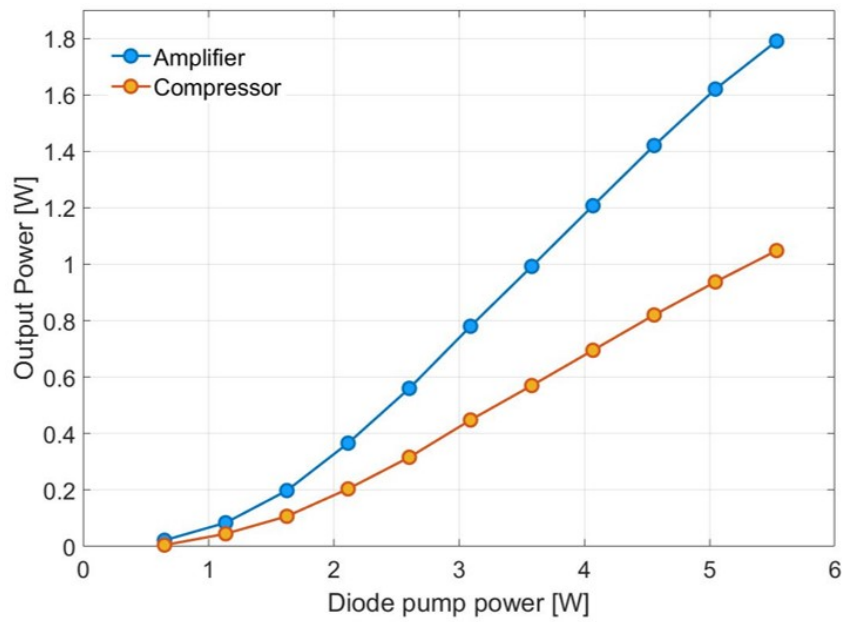
FIGURE 5.9: Output power characteristics of the amplifier (blue line) and
the compressor (red line) as a function of the diode pump power.

The long-term power stability measure, shown in Fig. 5.10, yields excellent results
with average power stability of $\sim 0.01\%$ rms over one hour.
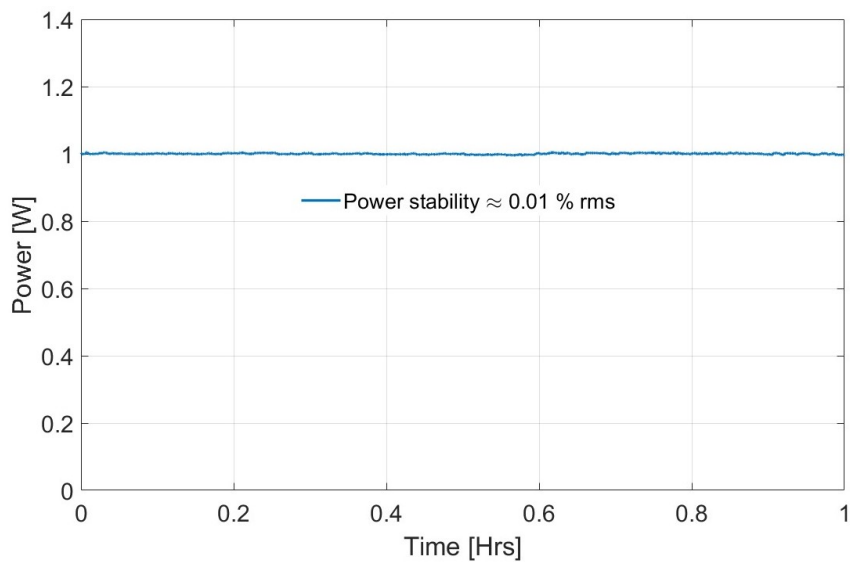

FIGURE 5.10: Average power stability measure of the output power after
the CPA over one hour.

The main features after the CPA are reported in Tab. 5.3

Chirped pulse amplification	
Average Power	1 W
Repetition Rate	10 MHz
Pulse Energy	100 nJ
Spectral bandwidth (FWHM)	10 nm
Pulsewidth	200 ps
Peak power	> 500 kW

TABLE 5.3

5.3 Realization of a portable setup

In view of the need to move the laser system from the lab at the University of Pavia, Italy, to the Institute of Photonic Science (ICFO) in Castelldefels, Barcelona (Spain), both the MO (including the seeder) and the CPA were built on separate boards. The MO, the PQS seeder and the stretcher where accomodated on the same breadboard and close in a 60×40 cm^2 box, as it is shown in Fig. 5.11. A photo of the closed box is shown in Fig. 5.12, while Fig. 5.13 shows the inside of the box.
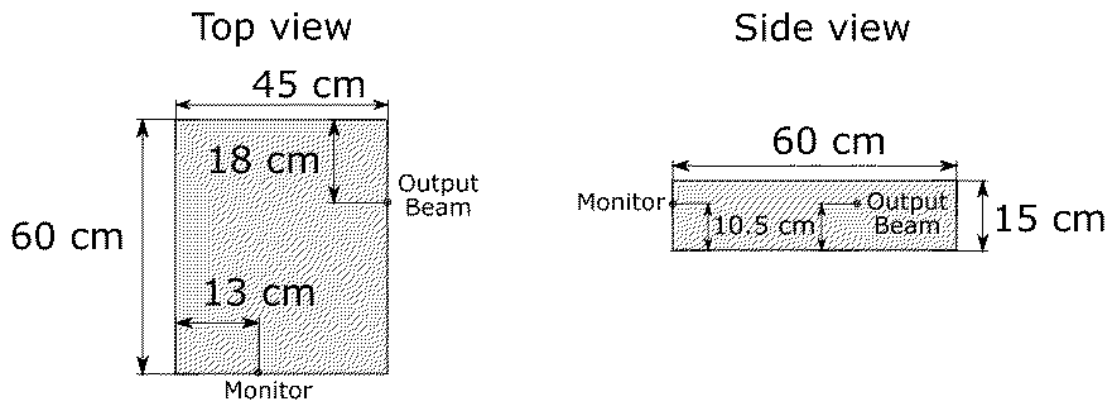

FIGURE 5.11: Footprint of the box containing the MO, the PQS seeder and the pulse stretcher.
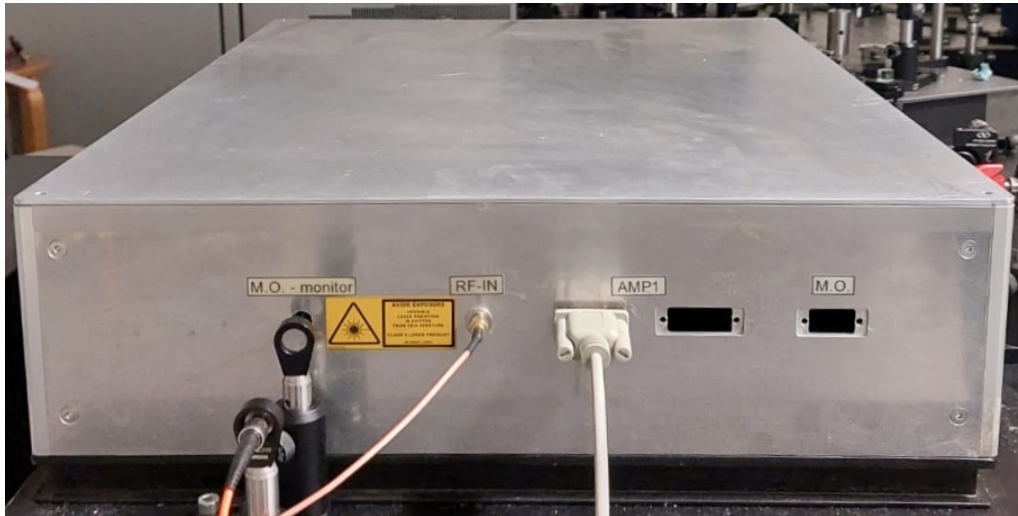
FIGURE 5.12: Picture of the closed box with the MaO, the PQS seeder and the pulse stretcher.

Legend Fig.5.13:

1. Microchip seeder control electronics

2. Microchip seeder

3. MO pump diode

4. MO cavity

5. Stretcher

The amplifier and the compressor were housed in two separate 15×30 cm^2 boards (see Fig. 5.14).
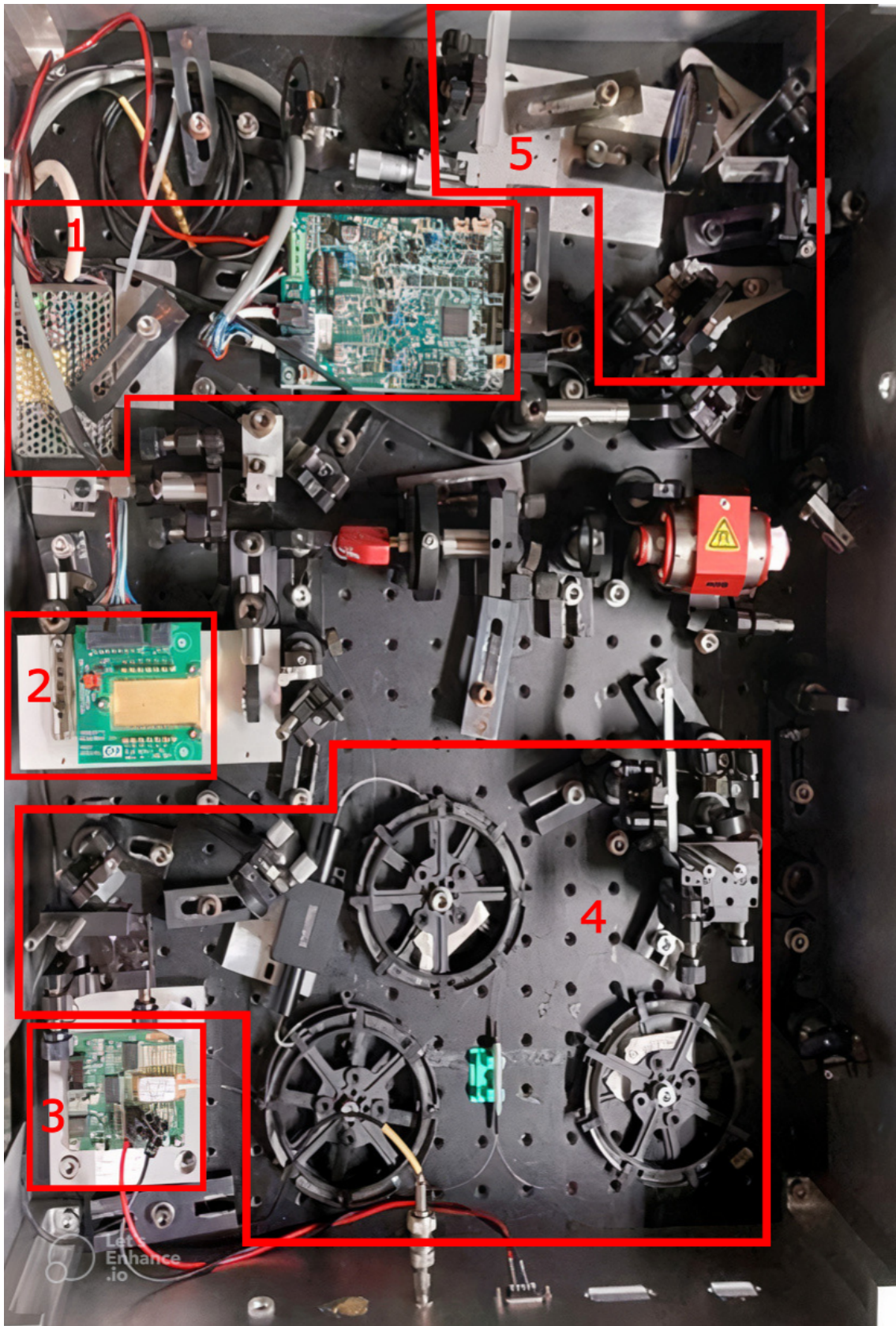
FIGURE 5.13: Picture of the opened box with the microchip seeder, the MO
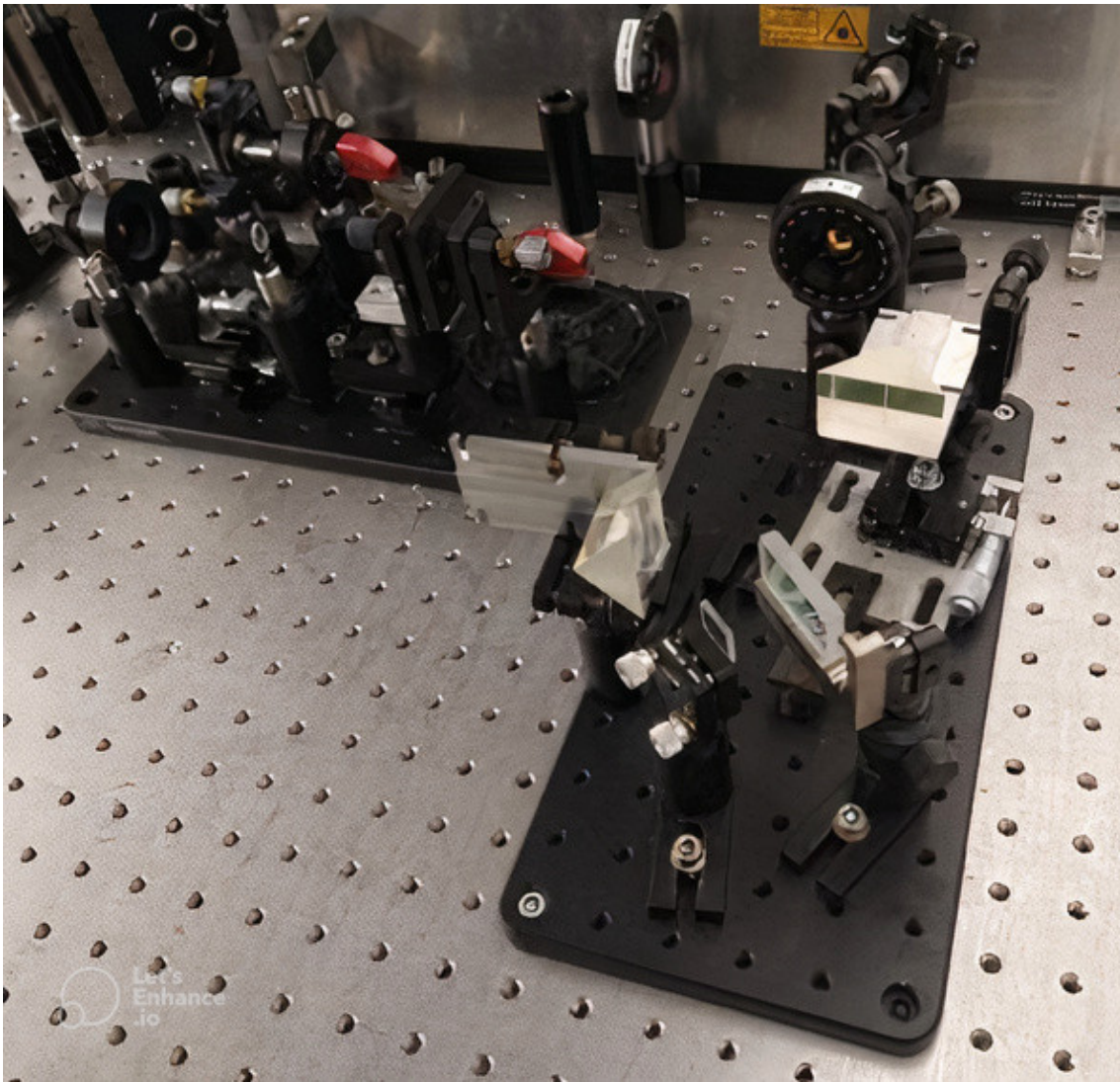and the stretcher.

FIGURE 5.14: Boards with the amplifier and the compressor.

Chapter 6

Optical parametric generation experiments

In this chapter, I will present the optical parametric generation (OPG) experiments exploiting the femtosecond source, based on the amplified MO, as the pump source.

Part of the experiments with the periodically poled MgO:PPLN crystal took place at the Institute of Photonic Sciences (ICFO) in Castelldefels, Barcelona, during my second year of Ph. D. Indeed, the setup of the MO was made portable, as described in the previous Chapter. In this way, I could bring the laser source from Pavia to the ICFO and conduct the experiments at the Parametric Optical Oscillators group headed by Prof. Majid Ebrahim-Zadeh.

During my third year of Ph.D., I was back in Italy and I tested at the Laser Source Laboratory of the University of Pavia both the 42-mm-long Mgo:PPLN crystal I used in Barcelona (conducting other experiments compared to those performed at the ICFO) and a 19-mm-long PPLN crystal.

In the next sections, I will present an introduction to the OPG process with fs sources and a brief discussion on quasi-phase-matching and periodically poled crystals. Eventually I will present and compare the results of the OPG experiments with the two aforementioned crystals I tested.

6.1 Femtosecond optical parametric generation

Tunable femtosecond laser sources in the mid-infrared (mid-IR) are of great interest for applications such as spectroscopy, material processing, laser surgery and frequency combs [29][30]. Optical parametric frequency conversion techniques have emerged as a reliable and cost-effective way to generate high-power coherent radiation in the range from 1 to 12 μm, a region that includes the important molecular fingerprints beyond 2 μm, where direct laser generation is not readily available.

The schematic of the working principle of OPG is shown in Fig.6.1

FIGURE 6.1: Schematic of optical parametric generation.

The gain required to trigger OPG starting from quantum noise, is extremely high. For this reason, together with a very intense pump, both nonlinear optical materials with very high nonlinear coefficients and, possibly, a long interaction length is required. Moreover, OPG is practically possible only if, in addition to energy conservation, there is also linear momentum conservation. This means that a the phase-matching (PM) condition must be fulfilled by the three waves involved in the process, i.e., the pump, the signal and the idler:

$$\Delta \vec{k} = \vec{k}_p - \vec{k}_s - \vec{k}_i = 0 \tag{6.1}$$

where k_p, k_s and k_i are the wave-vectors of the pump, signal and idler, respectively.

This condition expresses the requirement that the pump wave travels at the same phase-velocity as the generated signal and idler waves, so that all the contributions generated during propagation in the nonlinear medium add in phase. The PM is a necessary condition for an efficient energy conversion from the pump to the other waves.

However, this condition cannot always be satisfied as for materials that do not have birefringence (e.g., Gallium Arsenide) or may possess insufficient birefringence to compensate for the linear dispersion of the refractive indices over the wavelength range of interest.

However, the quasi-phase-matching (QPM) can be an alternative solution in these cases in presence of nonlinear materials with a ferroelectric behaviour. The idea behind the quasi-phase-matching is shown in Fig. 6.2, in which you can observe a nonlinear homogeneous ferroelectric single crystal (Fig. 6.2 a) and a periodically poled ferroelectric crystal with a period Λ (Fig. 6.2 b).
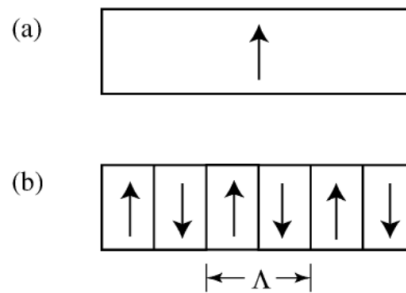

FIGURE 6.2: a) A homogeneous single crystal and b) a periodically poled material.

A periodically poled crystal is fabricated so that the orientation of one of the crystalline axes (often the c-axis of a ferroelectric material) is periodically inverted within the crystal. An inversion in the direction of the c-axis results in an inversion of the sign of the nonlinear coupling coefficient, which can compensate for a non-zero wave vector mismatch Δk. This effect is illustrated in Fig.6.3 for the case of Second Harmonic (SH) generation.
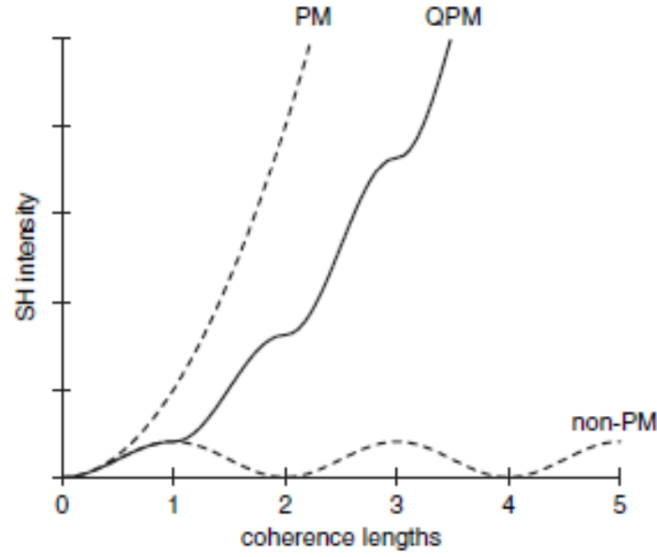
FIGURE 6.3: Second harmonic intensity in the cases of PM, non-PM, and QPM.

In the case of perfect PM, the intensity of the generated wave grows quadratically with the propagation distance, instead with no PM, the intensity of the generated wave oscillates with the propagation distance. When we have the quasi-phase-matching (QPM curve), assuming a period Λ equal to twice the coherent length of the nonlinear interaction, each time the intensity of the generated waves starts to decrease for the wave vector mismatch, the change in the sign of the nonlinear coupling coefficient leads to the field amplitude to monotonically grow.

In terms of wave-vectors, the QPM condition could be written as:

$$\Delta k = k_p - k_s - k_i + \frac{2\pi}{\Lambda} = 0 \tag{6.2}$$

It is clear from the formula that the QPM condition depends on the refractive index seen by the waves in the nonlinear crystal, which depends on their wavelength and also on the grating period of the crystal exploited during the parametric conversion process.

If compared to Optical Parametric Oscillation, OPG is a straightforward nonlinear process to implement because it is a single-pass process, eliminating the need for a resonant cavity and therefore reducing the complexity of the system. The main challenge

remaining the very high intensity required to trigger the process.

OPG usually rely on either intense nanosecond or picosecond pump sources. Achieving high performance in the femtosecond regime is challenging because of the wide bandwidth that fs pulses intrinsically posses. The dispersion of materials pumped with fs pulses leads to temporal walk-off effects between the pump, the signal, and the idler (see Fig 6.4). They, in fact, usually propagate with different group velocities through the nonlinear crystal, thus reducing the interaction length and hence the conversion efficiency. The aforementioned process, known as Group-velocity-mismatch (GVM), poses an upper limit on the usable crystal length (typically 1-2 mm). Another equivalent way of describing this process is by defining a PM acceptance bandwidth, which measures the maximum bandwidth for the pump, which can be efficiently down-converted to the signal and idler output, given a certain nonlinear crystal length. This issue severely affect the performance of OPG, usually limiting the options in the fs-regime to Optical Parametric Oscillators only.
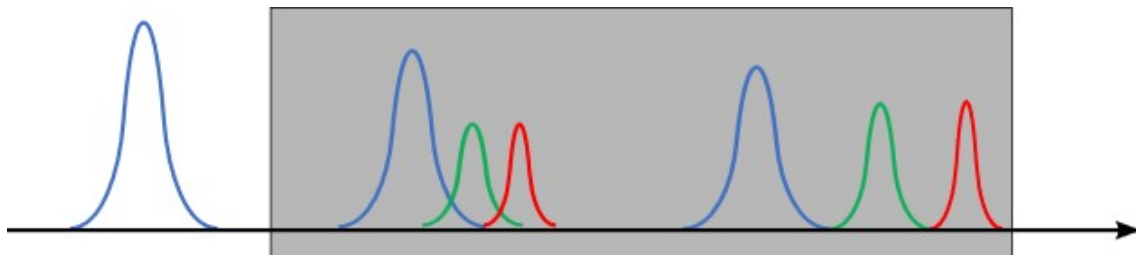

FIGURE 6.4: Pictorial representation of temporal walk-off due to group velocity mismatch $\neq 0$ in a nonlinear crystal.

However, the effects of GVM can be overcome in a particular situation, when the dispersion properties of the nonlinear material are such that the pump and idler experience the same group velocity for wavelengths for which phase-matching condition occurs [31] [32]. This leads to a wider spectral acceptance bandwidth of the pump and, under such circumstances, a longer crystal can be used for an efficient frequency conversion process.

The nonlinear crystals used in the OPG experiments, illustrated in the following sections, have this particular feature. I, therefore, used the MO designed and built during my early Ph.D. years as the fs pump source for OPG. One of the very favourable features

of this peculiar fs laser system is its native, relatively low, pulse repetition rate. This permits, even with modest average power (1 W, in our case) to have high pulse energy (100 nJ) and pulse peak power (500 kW) in the fs regime. Thus the amplified MO can be particularly advantageous since it permits to reduce the thermal load and the thermal effects due to residual absorption in the NL crystals.

6.2 MgO:PPLN crystal

Two different sets of experiments were performed for the MgO:PPLN crystal. The first was at the Institute of Photonic Sciences (ICFO) in Castelldefels, Barcelona. Experiments during my research period abroad focused on studying the optimal grating for parametric generation of the Mgo:PPNL crystal, analyzing conversion efficiency, spectral range, quality of the pulses etc. The second set of measurements, instead, was performed in Italy, at the Laser Source Laboratory of the University of Pavia. These experiments focused on studying the full spectral range obtainable through the other gratings of the non-linear crystal. To simplify the comprehension of the Chapter, and to have no redundancy in the results obtained from the experiments, tests of OPG with the MgO:PPLN crystal conducted at ICFO and at University of Pavia, will be summarized together in this section reporting only the most significant results.

These results led to a publication in the international journal Optics Letters [33] and the main results were also presented at two international conferences: Advanced Solid State Lasers (ASSL) conference 2022 [34] and Conference on Lasers and Electro-Optics (CLEO) Europe 2023 [35].

The crystal used is a 5 mol% MgO periodically-poled LiNbO$_3$ (MgO:PPLN). It is 42-mm-long, 2-mm-wide, and 1-mm-thick, with 4 uniform gratings ranging in period from $\Lambda = 28.5$ μm to $\Lambda = \mu$m, in steps of 0.5 μm, designed for type-0 (e$\rightarrow$ee) quasi-phase-matched (QPM) interaction. The end faces of the crystal are antireflection-coated at 1064 nm (R < 1%), 1400-2000 nm (R < 0.5%), and 2000-4000 nm (R < 7%).

The MgO:PPLN crystal employed has a much greater length if compared to crystals of a few mm used for optical parametric conversion techniques. Consequently, during these experiments, I analyzed in particular the conversion efficiency achievable with this crystal, the duration and quality of the generated pulses.

The setup realized for the OPG experiments is shown in Fig.6.5. The crystal is mounted on a translation stage and housed in an oven, with a temperature stability of ± 0.1 °C to control the PM temperature. The pump beam is focused to a beam waist radius of ≈ 60 μm using a lens of focal length f = 150 mm. A dichroic mirror (DM) and a long pass filter (F) are used to separate signal, idler, and undepleted pump power. A polarizing beam splitter (PBS) is employed in combination with a half-wave plate (HWP 1) to control the incident pump power on the MgO:PPLN crystal. A second plate (HWP 2) is then used to optimize the polarization of the pump beam to maximize parametric generation.
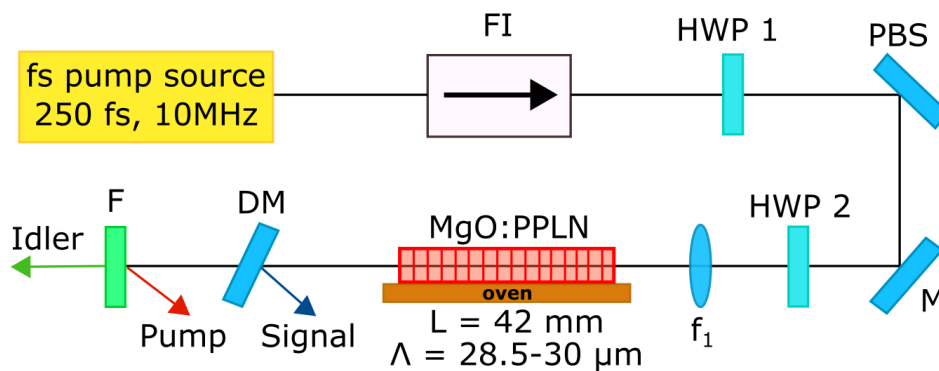

FIGURE 6.5: Setup for the OPG experiments with the MgO:PPLN crystal.

My first experiment was to find the oven operating temperature that would optimize the PM condition of the grating period Λ = 30 μm, which, from simulations, is the one that optimizes PM for the pump source wavelength [32]. Injecting 650 mW of pump power, corresponding to 65 nJ pulse eenrgy, I performed a scan from 40°C to 200°C with a step of 5°C, recording the signal power, idler power, and undepleted pump power. The results obtained are shown in Fig.6.6

Looking at the graph, you can observe that around 90°C (blue rectangle in the plot), there is a minimum for undepleted average pump power (≈ 110 mW) and a maximum for signal average power (≈ 290 mW). As for the idler, you can notice that the maximum
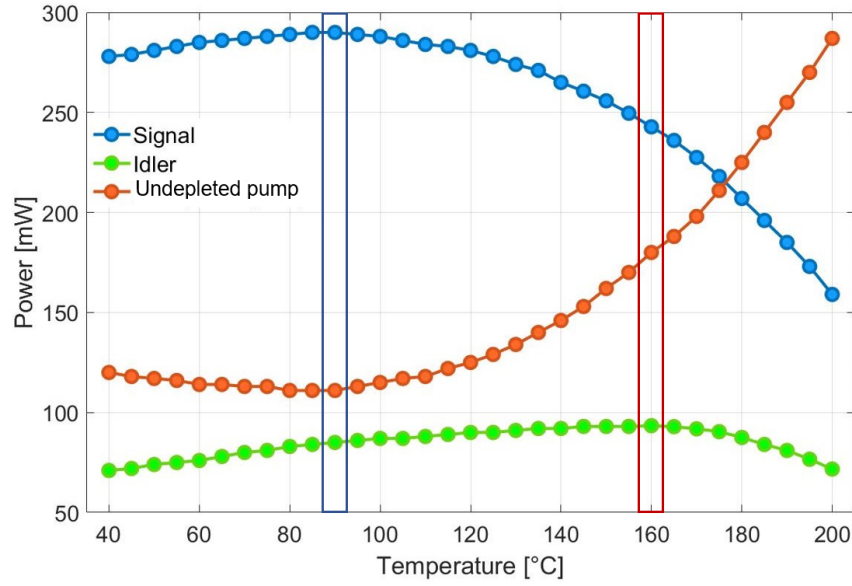
FIGURE 6.6: Recorded power of signal (blue line), idler (green line), and undepleted pump power (red line), as a function of the oven temperature.

average power of $\approx$ 93 mW is obtained at around 160°C (red rectangle). Therefore, it seems that the optimal temperatures for the idler and signal are different. However, we can notice that the variation in the idler average power for the two temperatures is very small (less than 10%). Consequently, this fluctuation of the optimal temperature could be due to various factors including the mode-matching and focusing parameters (which differ for signal and idler wavelength), as well as the wavelength-dependent losses originating from the antireflection coatings of the crystal, the dichroic mirror and the long pass filter used in the experiment. We can estimate an average loss of 5%. Therefore, for a temperature of 90°C, the maximum average power generated by injecting 650 mW (65 nJ pulse energy) is more than 305 mW (30.5 nJ pulse energy) for the signal and about 100 mW (10 nJ pulse energy) for the idler. A more accurate investigation showed that the optimal working temperature for the phase-matching condition is around 92°C.

The low threshold for the single-pass OPG process ensures further power scalability, also enabling the extension of the tuning range by using alternative grating periods. For this reason, I also studied the spectral range achievable with the different grating periods of the crystal. By fixing the oven temperature at 92°C and pumping at 470 mW average
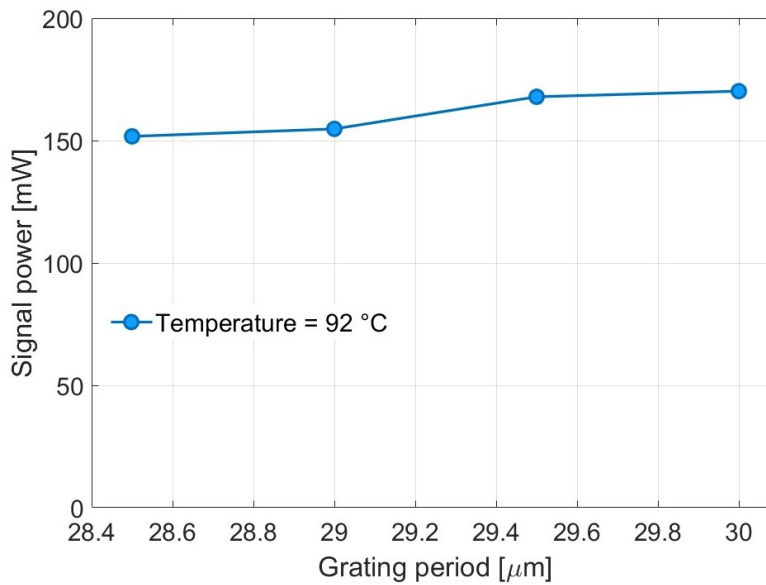
FIGURE 6.7: signal average power as a function of the grating period for
an incident pump average power of 470 mW.

power (47 nJ pulse energy), I recorded the signal average power, reported in Fig. 6.7 for
the different crystal gratings. As you can see, changing the grating period only slightly
affects the average signal output power, which experience only a 12% reduction from the
maximum value registered with the 30 μm period grating and the minimum observed
for the 28.5 μm one.

Signal spectra were also recorded during the temperature and the grating scan mea-
surements. The result of the measurement is reported in Fig. 6.8. By changing the temper-
ature of the MgO:PPLN crystal from 40°C to 200°C, the signal central output wavelength
varies from 1511 nm to 1562 nm with a typical FWHM bandwidth of $\sim$ 10 nm. If, instead,
we change the grating period at fixed temperature, the signal central output wavelength
varies from 1445 nm to 1530 nm. Since the graphs in Fig. 6.8 have the same horizontal
scale, it can be seen that by combining the two different types of tuning, it is possible to
cover the whole spectral region extending between 1445 nm and 1562 nm.

For what concerns the idler, the same measurement was carried out and is shown
in Fig. 6.9. When the wavelength tuning is realized by means of the oven temperature
variation, the idler central output wavelength varies from 3318 to 3600 nm, with FWHM
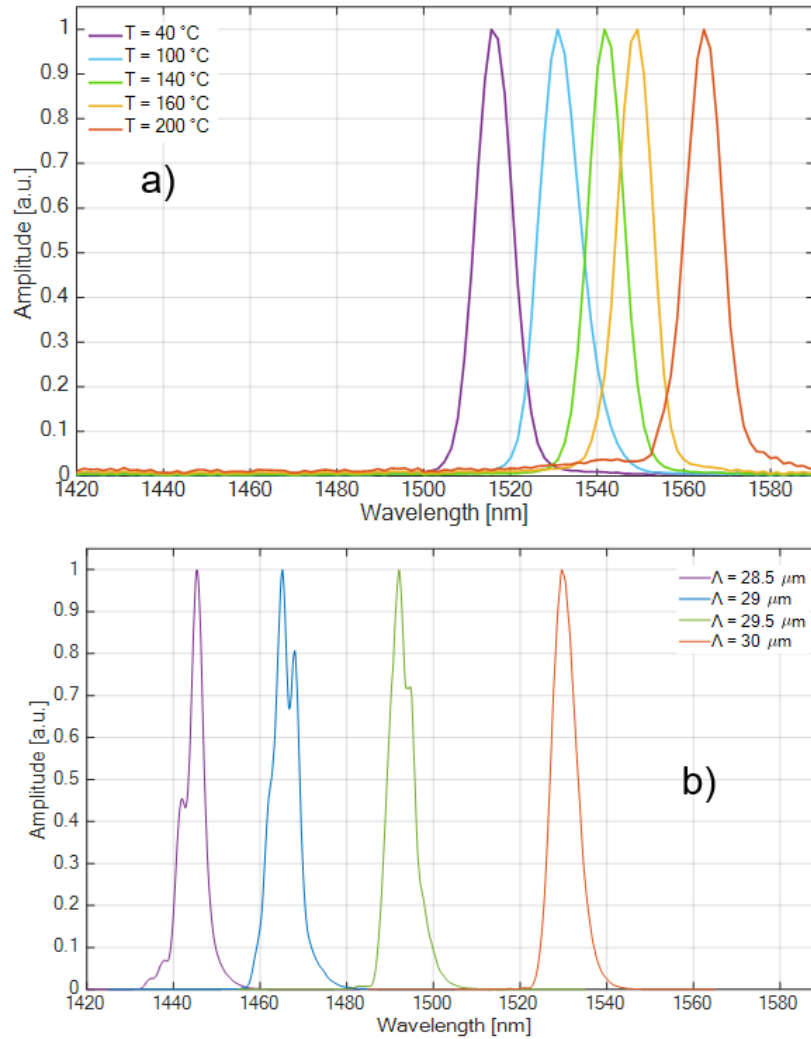
FIGURE 6.8: Signal spectra registered during the temperature scan (a) and
the grating scan (b).

bandwidth $\geq$ 100 nm across the whole tuning range and a maximum of $\sim$ 181 nm at
3457 nm. By exploiting the grating period tuning at fixed temperature, the idler spectra
cover the range from 3570 nm to 4117 nm. When we look at Fig. 6.9 a), it becomes more
and more noticeable the progressive increase in the group-velocity mismatch between
the pump and the idler, that results in a clear tendency of the idler spectra to become nar-
rower and narrower as the temperature decreases. However, these measurements show
that even if the temperature or the grating are not optimized for quasi-phase-matching, it
is still possible to have efficient parametric generation at very good power/energy levels
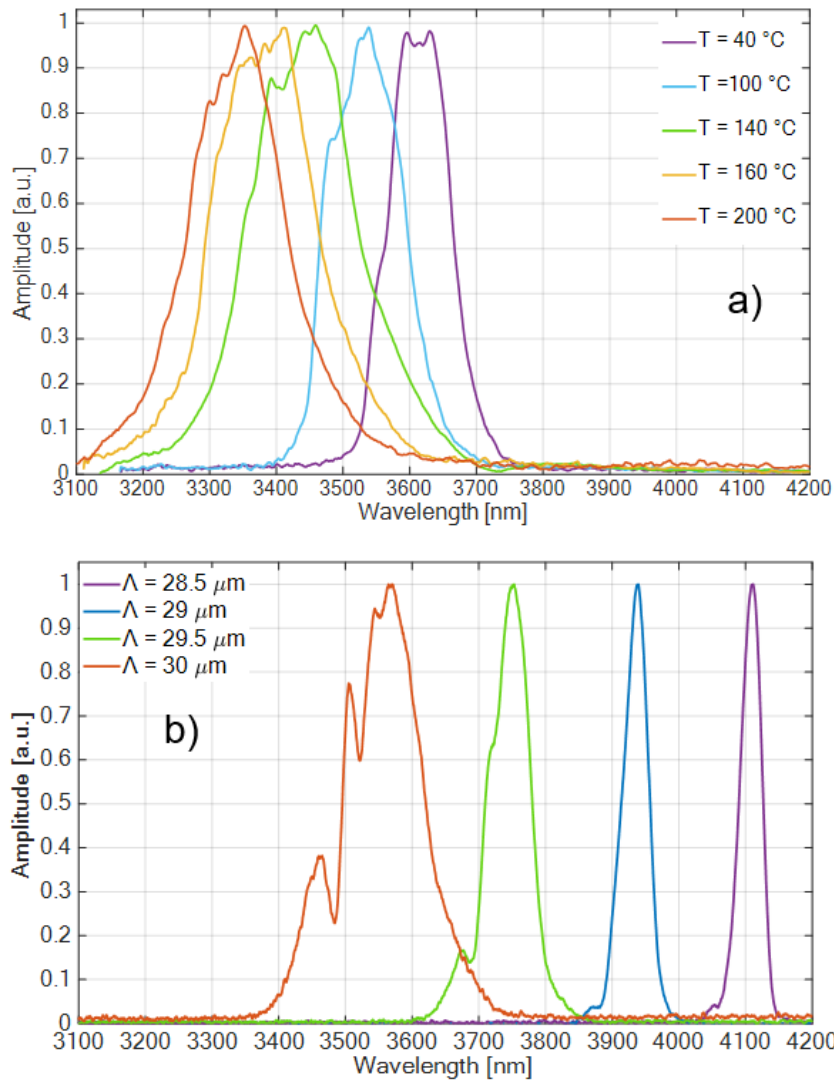
with a minimal drop in performance.

FIGURE 6.9: Idler spectra registered during the temperature scan (a) and the grating scan (b).

I also performed simulations for the temperature and for the grating period tuning based on the Sellmeier equations [36] available for the 5 mol% MgO:PPLN crystal.

The very good agreement between the experimental results (blue circles for signal and green circles for idler) and the simulations (blue solid line for signal and green solid line for idler) is evident from Fig. 6.10.

I then measured the characteristic of idler and signal average power as a function of the incident average pump power for the grating period $\Delta = 30~\mu$m at the temperature of
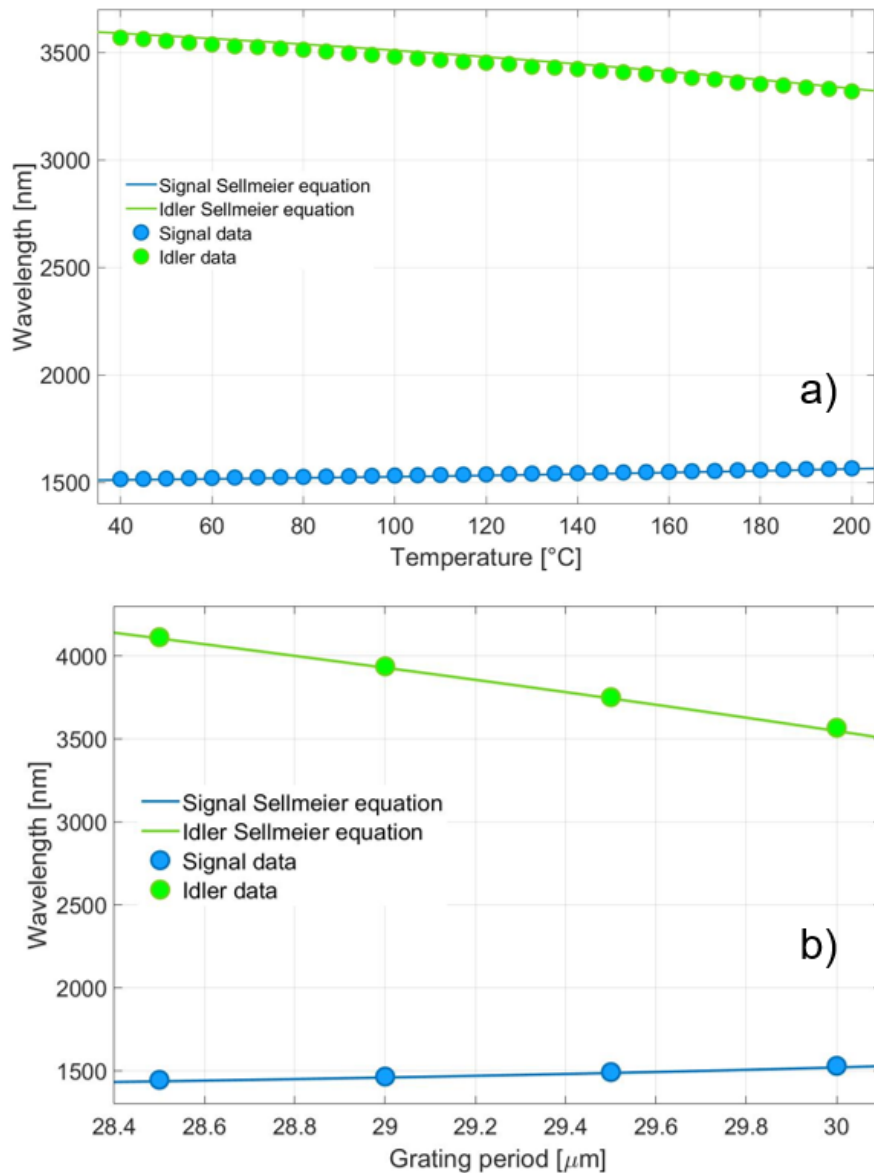
FIGURE 6.10: Experimental data (circles) compared with simulations (solid lines) of wavelengths as a function of temperature for signal (blue) and idler (green) for the grating $\Delta = 30$ μm (a) and for the grating tuning for a temperature of 92 °C (b).

92 °C. In Fig. 6.11 we can be observe that no saturation is evident in the characteristic. By measuring the slope well above the threshold, we can retrieve an efficiency of 50% for the signal (maximum pulse energy of 42.5 nJ at 100 nJ pump pulse energy), and of 20% for idler, with an maximum pulse energy of 19 nJ.

I also carried out simultaneous long-term power stability measurements of the output
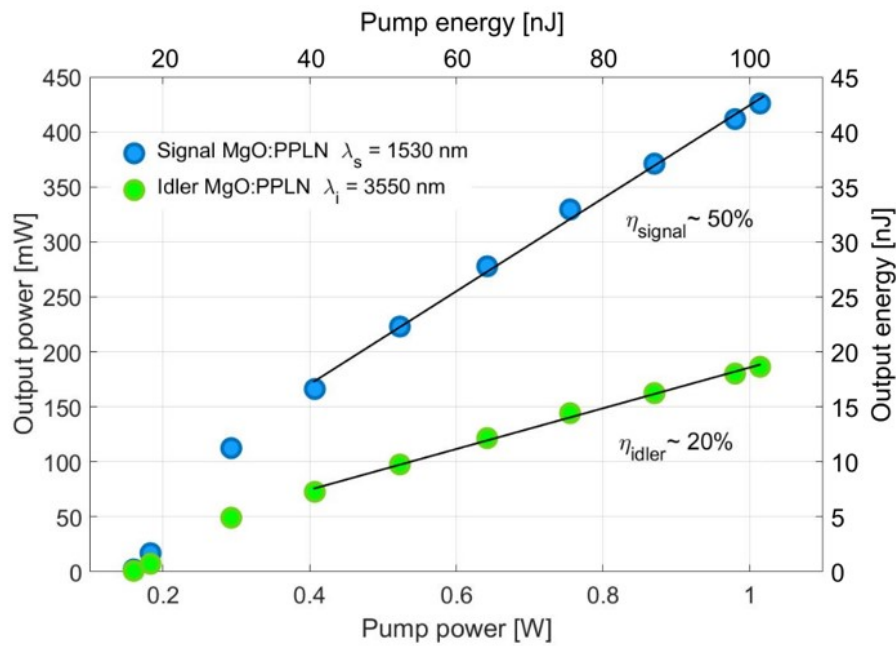
FIGURE 6.11: power scaling of the signal (blue) and the idler (green).

signal and idler (Fig. 6.12 a and Fig. 6.12 b) at 92°C for the grating period of $\Delta = 30$ μm. Both the signal at 1530 nm, and the corresponding idler at 3566 nm exhibited excellent average power stability with $\sim 0.2\%$ rms fluctuations over one hour. It is worth to point out that only the MgO:PPLN crystal is thermally stabilized: the MO pump source had no
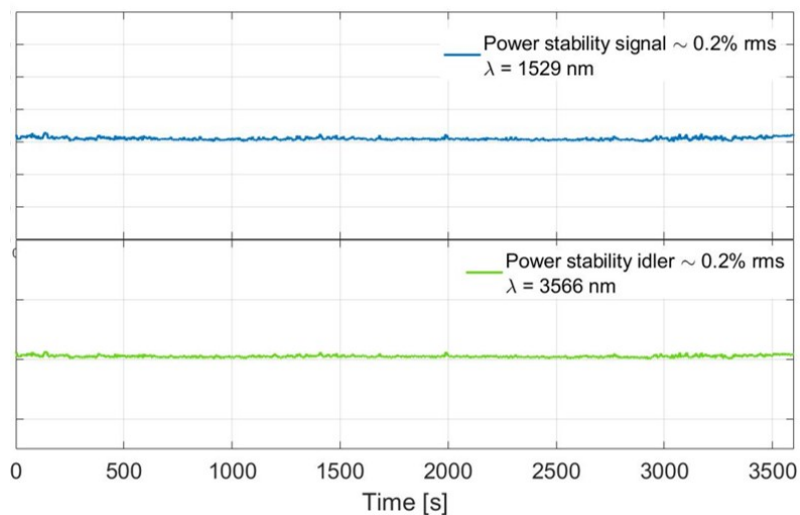
FIGURE 6.12: Power stability measurements of the output signal (blue line)
and idler (green line) over one hour run.

type of control for power fluctuations. This is a clear indication of the excellent stability of the femtosecond MO and CPA amplifier.
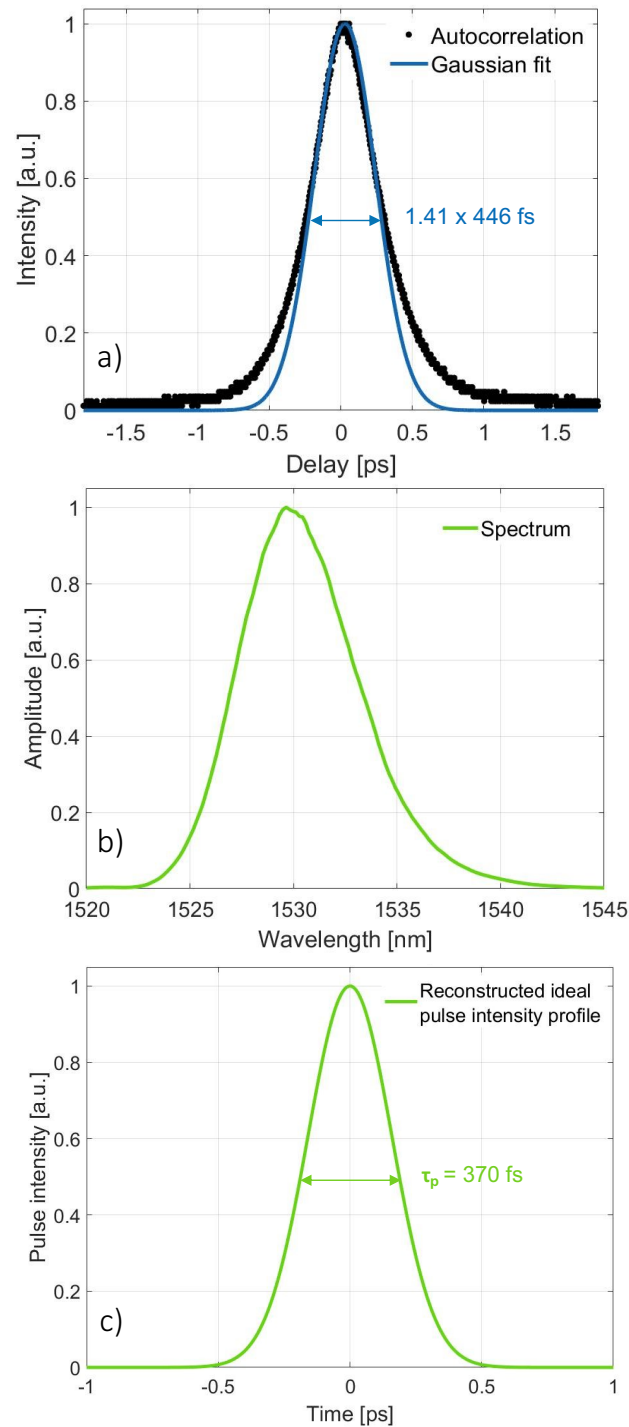

FIGURE 6.13: a) Autocorrelation trace (black points) and gaussian fit (blue line). b) Spectrum of the signal. c) Reconstructed ideal intensity profile starting from the signal spectra.

For what concerns the characterization of the signal pulses, we performed a SH intensity AC measuerement which is shown in Fig. 6.13 a). The black dots correspond to the measured data for the grating period of 30 μm at the operating temperature of 92°C. Assuming a Gaussian shape of the pulse (blue line), from the best fit, we obtain a pulse duration of $\sim$ 450 fs. Given the spectrum of the pulses (Fig. 6.13 b)), in order to understand how far we are from the Fourier transform limit, I calculated the corresponding ideal pulse intensity profile assuming a constant phase over the whole spectrum. the result is show in Fig. 6.13 c). With this procedure we can calculate the minimum pulse duration that can be sustain by the actual optical spectrum of the signal pulses, which turned out to be about 370 fs, i.e., we are only about 1.2 times above the Fourier Transform limit with the measured pulse duration.

The same procedure was performed for the other grating periods as well. The results obtained are shown in Table 6.1. In particular, you can observe in the last column the ratio between the measured pulse duration and the Fourier Transform limited pulse duration ($\tau_{measured}/\tau_{ideal}$). this ratio is always close to 1, meaning that the signal pulses obtained in the OPG process with the MgO:PPLN crystal are very close to the Fourier limit.

Grating [μm]	Signal wavelength [nm]	$\tau_{measured}$ [fs]	τ_{ideal} [fs]	$\tau_{measured}/\tau_{ideal}$
28.5	1445	390	346	1.12
29	1465	393	390	1
29.5	1493	385	355	1.08
30	1530	446	370	1.2

TABLE 6.1

The beam quality measurement of signal and idler performed with the standard knife-edge method, are reported in Fig.6.14. The measured M^2 parameter of the signal and idler is ≤ 1.5. This excellent result confirms a very good preservation of the pump spatial beam quality in the long MgO:PPLN crystal.

We also investigated the dependence of the OPG threshold on the duration of the pump pulse (see Fig. 6.15). This is quite straitforward thanks to the flexibility given by the CPA. Indeed, the amplified pulse duration can be easily varied by simply changing the negative dispersion in the Treacy pulse compressor.
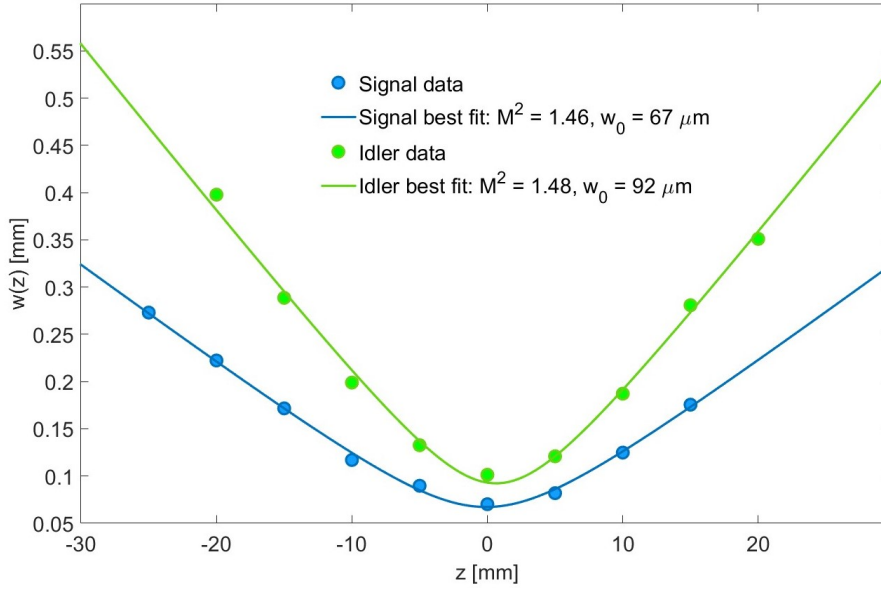
FIGURE 6.14: beam quality of signal (blue) and idler (green).

For the experiments reported so far, the Treacy compressor of the CPA was set to minimize the duration of the pump pulse. In this case, we modified the length of the Treacy compressor to give either additional negative dispersion (orange line in the graph), or to reduce the net amount of negative dispersion (this is the meaning of "positive dispersion") represented by the blue line in the graph. To measure the threshold we set the oven temperature at 92°C and we choose the 30 μm grating period. We monitored the OPG output with an optical spectrum analyzer set in log scale (dBm) with a noise base level of about -70 dBm. When we noticed the onset of the signal at 1530 nm, we recorded the value of the incident pump average power (hence of the pump pulse energy).

As expected, when the pulse duration is increased, the peak power diminishes and the threshold grows. We observed a different rate of growth of the threshold depending on the sign of the residual chirp in the pump pulse. You can see that decreasing the amount of negative dispersion in the compressor (blue curve) lowers the threshold compared to increasing the negative dispersion (orange curve). In particular, by varying the duration of the pulses from 0.2 ps to $\sim$ 0.8 ps we have an increase in the threshold pump power of a factor about 1.5 for the excess of positive dispersion (blue dots/line) and a factor about 1.8 for an excess of negative dispersion (orange dots/line). Some numerical
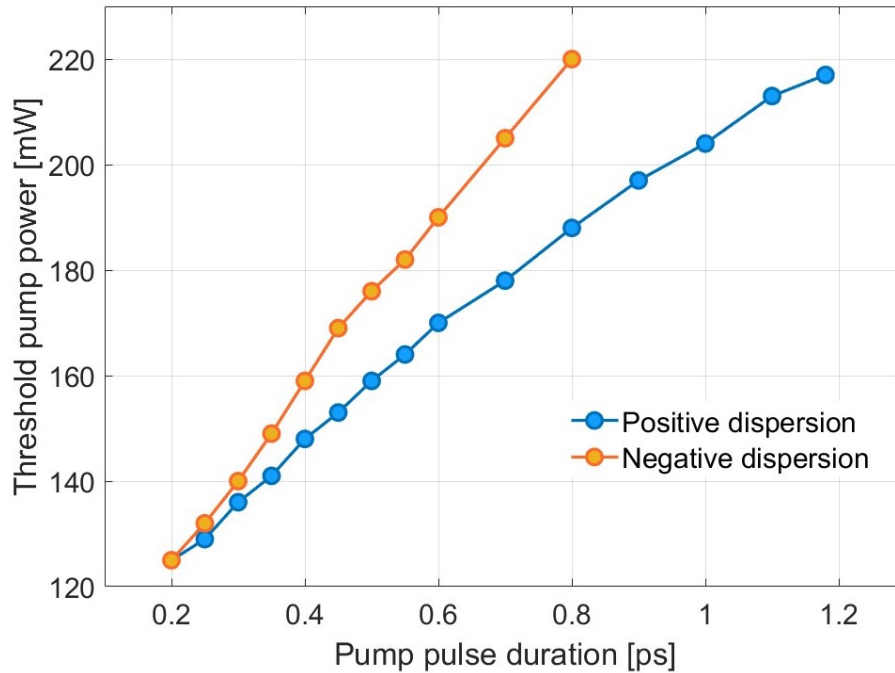
FIGURE 6.15: Threshold pump average power as a function of the pump pulse duration by changing the length of the Treacy compressor in the CPA, thus giving additional negative dispersion (orange line) or reducing the amount of negative dispersion (blue line) with respect to the amount of negative dispersion required to minimize the pump pulse duration at the output of the CPA.

simulations are ongoing to help in the interpretation of these results.

In conclusions, by exploiting OPG in a Group-Velocity-Matched 42-mm-long MgO:PPLN crystal we obtain excellent conversion efficiency of 50% and 20% for signal and idler, measuring 42.5 nJ (425 mW) for the signal and 19 nJ (190 mW) for the idler with an incident pump pulse energy of 100 nJ (1 W). The signal pulse duration was about 400 fs, very close to the Fourier Transfor limit, given the idlers spectrum width. The whole tuning range of the signal and idler wavelength, considering a combination of the temperature and the grating period scan, is 120 nm for the signal, extending from 1445 nm to 1566 nm, and 800 nm for the idler, extending from 3318 nm up to 4112 nm. Signal and idler showed an excellente average power stability in a smooth almost TEM_{00} beam profile ($M^2 < 1.5$), thus well preserving the pump beam characteristics.

6.3   PPLN crystal

In this section, I will present the OPG experiments carried out with the periodically-poled LiNbO$_3$ (PPLN) crystal. It is 19-mm-long, 11-mm wide, and 500-μm thick, with 8 gratings with a period varying between Λ = 28.5 μm and Λ = 29.8 μm in steps of 0.18 μm. The two end facets are antireflection coated for the pump and the signal wavelengths. In this case, we tested a shorter crystal for the OPG process to verify if the conversion efficiency and the signal pulses duration, were comparable to those obtained with the MgO:PPLN crystal, which has more than twice the length of the PPLN.

The setup realized for the experiments is shown in Fig.6.16. The lens f$_1$ (f = 150 mm) is anti-reflection coated at the pump wavelength and focuses the pump beam into the nonlinear crystal to a waist of $\approx$ 40 μm, in order to fairly match the confocal parameter of the pump to the PPLN crystal length. The CaF$_2$, un-coated lens f$_2$ = 80 mm is used to collimate the output beams. The High Reflectivity (HR) mirror at 1060 nm separates the pump beam from the signal and idler. We separately characterized the transmission of this mirror for the idler and signal wavelengths, in order to take into account the mirror losses in the generated signal and idler power measurements. A polarizing beam splitter (PBS) is used in combination with a half-wave plate (HWP$_1$) to control the amount of incident pump power on the PPLN crystal. The HWP$_2$ is used to optimize the polarization of the pump beam to allow parametric generation.
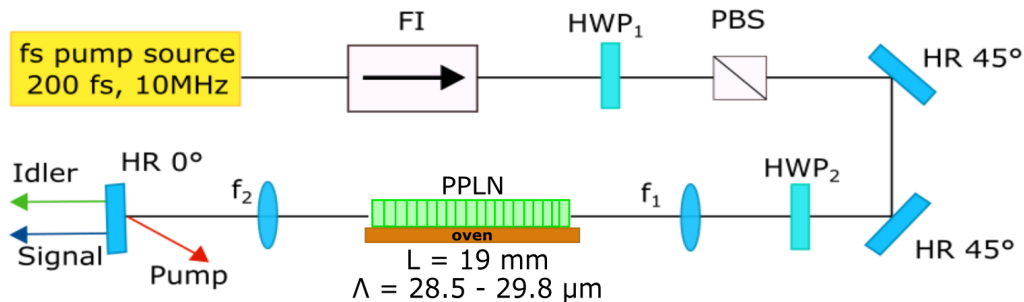

FIGURE 6.16: setup for the OPG experiments with the PPLN crystal.

The crystal is housed in a home-made oven, for this reason, we do not have enough accuracy in choosing temperatures, and to prevent damage due to photorefractive effects,

we tested the PPLN crystal at only two oven temperatures to find the optimal one for the optical parametric generation process. The results are shown in Fig. 6.17.
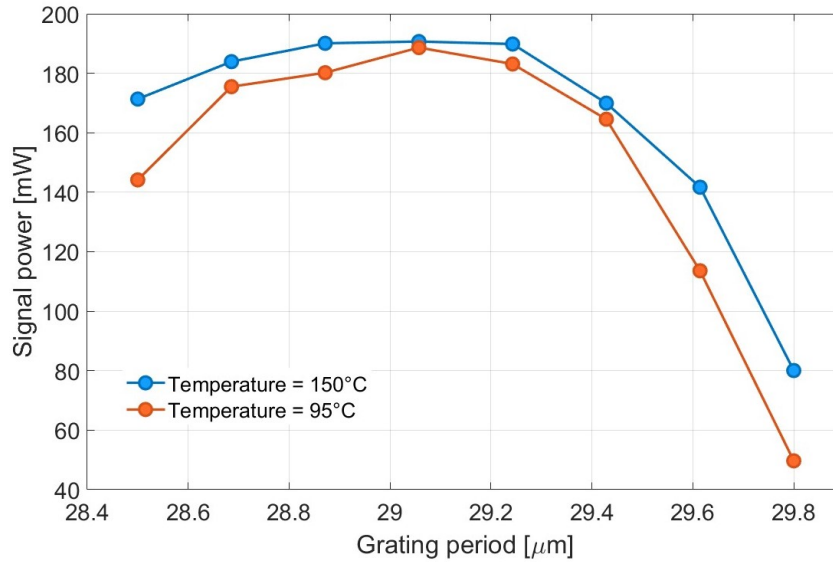
FIGURE 6.17: Signal power as a function of the grating period for the temperature of 95°C (orange line) and 150°C (blue line).

As it can be seen, the recorded signal power levels are lower for temperature T = 95°C (red line in the graph) for all gratings. For this reason, an oven temperature of 150°C was preferred for the experiments. You can observe that, by injecting a pump power of 470 mW (47 nJ), at the temperature of 150°C the power levels are roughly constant with a maximum at 190 mW and a minimum variation of 5% excluding the two longest grating periods (29.61 μm and 29.8 μm).

This trend can also be seen from the signal spectra shown in Fig.6.18. Indeed, for these two gratings, the shape of the spectrum is not smooth and shows multiple peaks. Nevertheless, we obtained a spectral tuning range of 100 nm, from 1475 to 1580 for the signal and more than 470 nm for the idler, from 3376 to 3854 (see Fig.6.19).
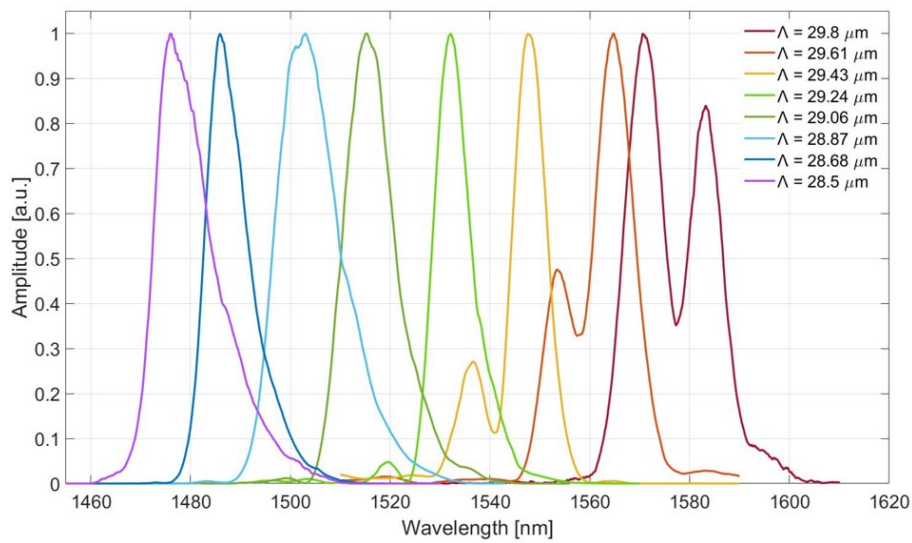
FIGURE 6.18: Signal spectra for the different grating periods at the temperature of 150°C.
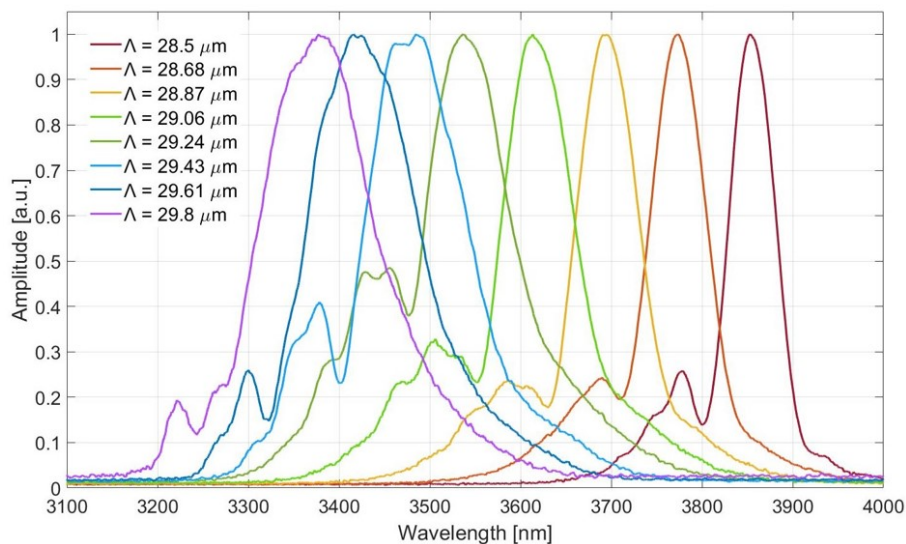
FIGURE 6.19: Idler spectra for the different grating periods at the temperature of 150°C.

Comparison of Sellmeier equations for the PPLN crystal at the temperature of 150°C with the experimental data in Fig. 6.20 shows very good agreement for all the gratings, except for the one with a period of 29.8 μm, where the measured idler wavelength value is slightly above the theoretical curve.

I measured the power scaling of the PPLN crystal at the temperature of 150°C for the grating period 29.24μm. The results are shown in Fig.6.21. At 102 nJ (1.02 W) of pump
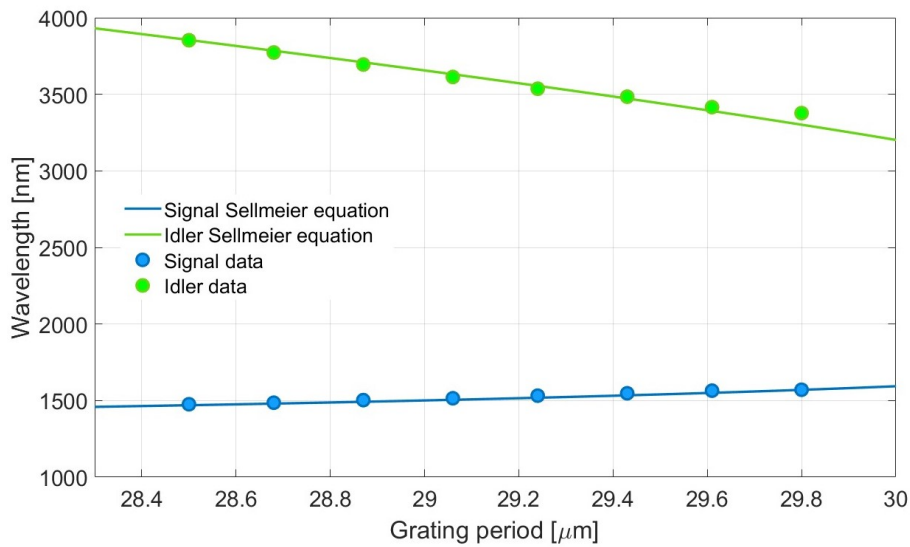
FIGURE 6.20: Experimental data (circles) compared with simulations (solid lines) of wavelengths as a function of grating period for signal (blue) and idler (green) at the temperature of 150°C.

power, a value of 44 nJ (440 mW) is measured for the signal and 20 nJ (200 mW) for the idler with a conversion curve slope efficiency, well above the threshold, of 47% and 21%. The threshold is around 220 mW (22 nJ) of pump average power. These results are excellent for the single-pass optical parametric generation.
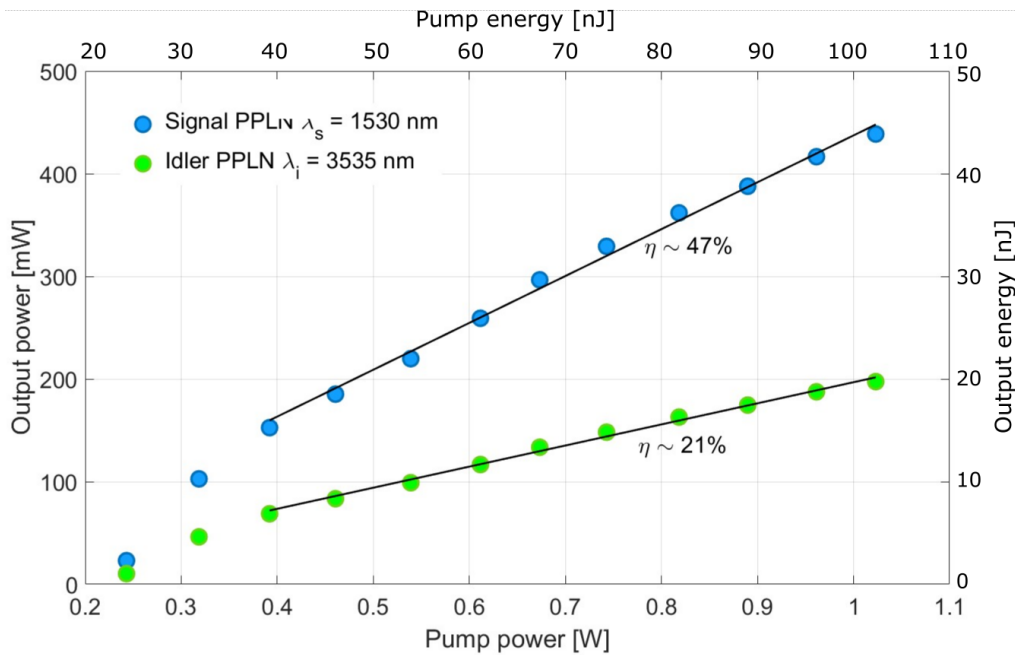
FIGURE 6.21: Power scaling of the signal (blue) and the idler (green).

Grating [μm]	Signal wavelength [nm]	$\tau_{measured}$ [fs]	τ_{ideal} [fs]	$\tau_{measured}/\tau_{ideal}$
28.5	1476	355	192	1.8
28.68	1486	312	248	1.25
28.87	1503	306	200	1.5
29.06	1515	300	212	1.4
29.24	1532	306	177	1.7
29.43	1548	327	190	1.7
29.61	1564	305	143	2
29.8	1580	270	196	1.4

TABLE 6.2

To evaluate the temporal quality of the signal pulses, the same procedure explained in the previous section was followed: I performed the Fourier transform of the electric field starting from the available data of the signal spectral intensity, assuming a constant phase. Then I derived the corresponding intensity profile of the ideal pulse and retreived the corresponding pulse duratio (τ_{ideal}). This value was then compared with the experimental data measured with the AC ($\tau_{measured}$). The results in Tab. 6.2 show measured pulse durations always shorter than 350 fs, with a minimum value of 270 fs. These values are shorter than the ones reported in Tab. 6.1 for the MgO:PPLN crystal (about 400 fs). The ratio $\tau_{measured}/\tau_{ideal}$ appears to be slightly higher than the MgO:PPLN crystal, however, the results exhibit good values with pulses that can be defined as nearly Fourier-limited.

The simultaneous long-term power stability measurements of signal and idler, shown in Fig.6.22, yield good results with average power stability of $\sim 0.25\%$ rms and $\sim 0.75\%$ rms for signal and idler respectively.

Measurements about the variation of the threshold by changing the pulse duration of the pump source lead to the same results already presented for the MGO:PPLN. Also the beam quality of signal and idler was very similar with a measured $M^2 \leq 1.5$ for both.

In this section we demonstrate that with the shorter PPLN crystal we were able to match the efficiency of the longer MgO:PPLN a similar threshold and maximum output power, comparable power stability and beam quality, with an improvement in the pulse duration of signal pulses which can be as short as 270 fs.
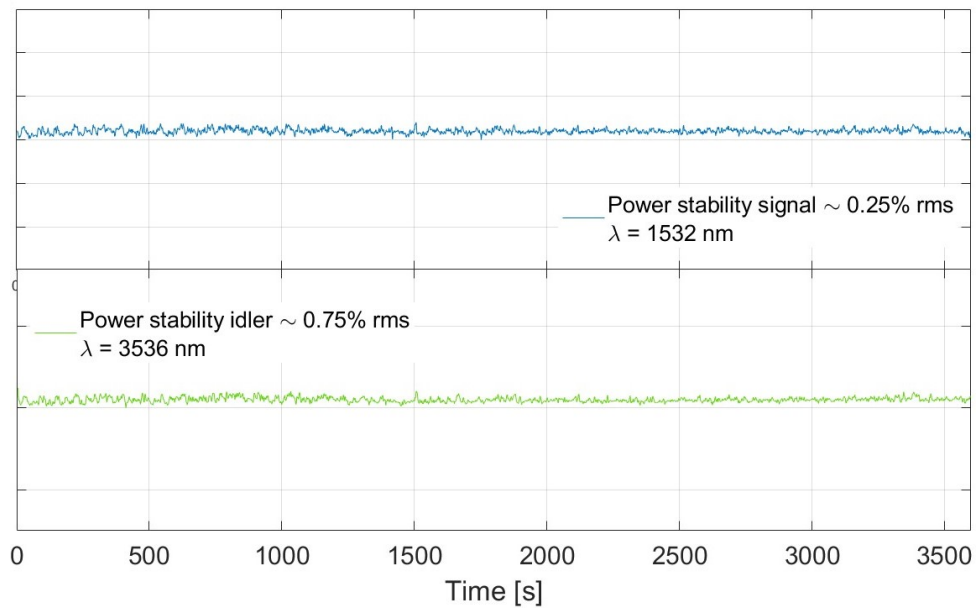
FIGURE 6.22: Average power stability measurements of the signal (blue line) and idler (green line) over one hour run.

These excellent results were presented to the international Advanced Solid State Lasers (ASSL) conference 2023 [37]. In addition, in collaboration with the Optical Parametric Oscillators group at ICFO, we are working on the writing of a manuscript reporting the comparison of the two crystals and a proper numerical model in support of the experimental evidences we observed.

6.4   Comparison between MgO:PPLN and PPLN

In this Chapter I reported efficient generation of femtosecond near-IR and broadband mid-IR pulses at 10 MHz repetition rate based on simple, single-pass OPG in MgO:PPLN and PPLN. Pumping with a microchip-started, amplified MO providing 500 kW peak power, 100 nJ, 200 fs-long-pulses and exploiting GVM-matching in long PPLN crystals, we obtain 42.5 nJ of signal and 19 nJ of idler for the Mgo:PPLN and 44 nJ and 20 nJ for signal and idler in the PPLN with similar sloper efficiency of 50% and 20%., respectively.

The whole tuning range of the output wavelength for the MgO:PPLN, considering the temperature scan and the grating period scan, is of 120 nm for the signal, extending from 1445 nm to 1566 nm, and 800 for the idler, extending from 3318 nm to 4112 nm. For the shorter PPLN crystal, the tuning range is 1475-1580 nm for the signal and 3376-3854 nm for the idler.

Both the crystals exhibit good power stability and good beam quality preservation with $M^2 \leq 1.5$ for both the signal and idler, thus maintaining the good pump beam characteristics. The practical output powers, high conversion efficiency, and broad spectral bandwidths, together with high spectral and spatial beam quality at 10 MHz repetition rate, make the Mamyshev-pumped OPG source attractive for access to near- to mid-IR femtosecond pulses at high energy and low average power.

Nonlinear crystal	42-mm-long MgO:PPLN	19-mm-long PPLN
Tuning range	Signal: 1445-1566 nm (120 nm) Idler: 3318-4112 nm (800 nm)	Signal: 1480-1580 nm (100 nm) Idler: 3380-3850 nm (470 nm)
Conversion efficiency	Signal: ~50 % Idler: ~20 %	Signal: ~50 % Idler: ~20 %
Output Energy	Signal: 42,5 nJ (100 kW peak power!) Idler: 19 nJ	Signal: 44 nJ (100 kW peak power!) Idler: 20 nJ
Power stability	Signal: 0.2% rms (1 h) Idler: 0.2% rms (1 h)	Signal: 0.25% rms (1 h) Idler: 0.75% rms (1 h)
Beam quality	Signal: $M^2 \sim 1.5$ Idler: $M^2 \sim 1.5$	Signal: $M^2 \sim 1.5$ Idler: $M^2 \sim 1.5$

FIGURE 6.23: comparison of the main characteristics obtained for the MgO:PPLN and the PPLN crystals, with the OPG process.

Conclusions

To conclude, in my Ph.D. thesis, I had the opportunity to build a low-power MO based on a single-mode polarization maintaining fiber at 1 μm and pumped by a single-mode pump laser diode. This was a new research line for our group at the University of Pavia, therefore, I had to learn a lot from experience over the years.

Nevertheless, different configurations of the MO were realized, testing several solutions for the spectral filters employed. In all cases, we demonstrated the operation of the MO once a seed pulse from a PQS microchip laser was injected into the cavity and the mode-locking regime was established. At the end, the best spectral filtering configuration was the combination of a Gaussian filter and a super-Gaussian filter, reaching an average output power of 35 mW at 10 MHz repetition rate, corresponding to a pulse energy of 3.5 nJ, compressible to a minimum pulse duration of 170 fs. Moreover, we demonstrated the effectiveness of a new seeding technique that exploits a narrow-band, sub-nanosecond, single-longitudinal-mode, pulses spectrally broadened by the four-wave mixing process in a passive, polarization-maintaining, single-mode fiber.

To increase the pulse energy and the peak power of the low-power MO pulses, we designed and built a chirped pulse fiber amplifier exploiting a 5-W fiber coupled multi-mode pump diode and a 2-meter-long double-clad, polarization maintaining Yb-doped fiber. In this way, we were able to achieve a pulse energy of 100 nJ and a peak power of $\sim$ 500 kW for a pulse duration of 200 fs. In addition, the entire setup was realized on individual transportable boards. This step was necessary to test the fs laser source based on the amplified MO as a pump source for optical parametric generation experiments carried out at ICFO in Castelldefels, Barcelona, during the second half of my Ph.D.

I tested the fs source with two different crystals: a 42-mm-long MgO:PPLN and a 19-mm-long PPLN. The final results are excellent. In fact, by injecting 100 nJ, 200 fs pulses, we obtain $\sim$ 42 nJ of signal and $\sim$ 20 nJ of idler for both crystals with similar slope efficiency of 50 % and 20% for signal and idler respectively. Depending on the wavelength and the crystal tested the pulse duration of the signal can vary in the range between 270 and 450 fs, always almost Fourier Transform limited.

The whole tuning range for the MgO:PPLN extends from 1445 nm to 1566 nm for the signal and from 3318 nm to 4112 nm for the idler. For the PPLN crystal, the tuning range is 1475-1580 nm for the signal and 3376-3854 nm for the idler. Both the crystals showed very good average power stability and almost Gaussian TEM_{00} beam profiles with beam quality parameter ($M^2 \leq 1.5$) for both signal and idler.

Given the excellent results of this laser source based on a low-power amplified MO, we recently started to work on a Watt-level MO exploiting double-clad, large-mode-area fibers and multi-Watt pump laser diode. Preliminary promising results employing this power-scaled oscillator have been already presented to the international conference "Advanced Solid State Lasers" in Tacoma, Washington, USA [38] during 2023, but have not been included in this dissertation.

The MO architecture is a relatively new method for generating ultrashort pulses and can be considered a hot research topic on which there is still much work to be done.

List of Publications

Articles published in Peer Reviewed International Journals

1. S. Pizzurro, F. Pirzio, S. Jun, A. Di Lieto, G. Piccinno, M. Tonelli, A. Agnesi. "25 W continuous-wave Yb: $LiLuF_4$ single-crystal-fiber laser oscillator", Optics Communications, vol. 500, pp. 127337 (2021)

2. S. Pizzurro, S. Jun, M. Tonelli, L. Carrà, G. Piccinno, A. Agnesi, F. Pirzio. "1-mJ multi-kHz nanosecond pulses from a single-crystal $Yb:LiLuF_4$ amplifier seeded by a passively-Q-switched laser", Journal of Optica & Laser Technology, vol. 148, pp 107744 (2022)

3. S. Pizzurro, R. Gotti, L. Carrà, G. Piccinno, A. Agnesi and F. Pirzio. "Femtosecond Mamyshev fiber oscillator started by a passively Q-switched microchip laser", Optics Letters, vol. 47, pp 1960-1963 (2022)

4. Sukeert*, S. Pizzurro*, A. Esteban-Martin, R. Gotti, L. Carrà, G. Piccinno, A. Agnesi, F. Pirzio, S. Chaitanya Kumar, and M. Ebrahim-Zadeh."Efficient femtosecond optical parametric generation in group-velocity-matched MgO:PPLN at 10 MHz", Optics Letters, vol. 48, pp. 6008 (2023)

Communications to International conferences

1. S. Pizzurro, M. Tonelli, A. Agnesi and F. Pirzio. "Investigations on High Power Oscillators and Amplifiers Based on Birefringent $Yb:LiLuF_4$ Single Crystal Fibers Grown by the Micro Pulling Down" ALT'21 28th International Laser Conference

on Advanced Laser Technologies, Moscow 6-10 September 2021 (held virtually), INVITED talk.

2. Sukeert*, S. Pizzurro*, A. Esteban-Martin, R. Gotti, L. Carrà, G. Piccinno, A. Agnesi, F. Pirzio, S. Chaitanya Kumar, and M. Ebrahim-Zadeh. "Efficient Femtosecond Optical Parametric Generation in Group-Velocity-Matched MgO:PPLN at 10 MHz" Advanced Solid State Lasers Conference. 11-15 December 2022, Barcelona, Spain.

3. Sukeert*, S. Pizzurro*, A. Esteban-Martin, R. Gotti, L. Carrà, G. Piccinno, A. Agnesi, F. Pirzio, S. Chaitanya Kumar, and M. Ebrahim-Zadeh. "High Conversion Efficiency Broadband Femtosecond Mid-IR Optical Parametric Generation at 10 MHz" Conference on Lasers and Electro-Optics/Europe. 26-30 June 2023, Munich, Germany.

4. Sukeert*, S. Pizzurro*, A. Esteban-Martin, R. Gotti, L. Carrà, G. Piccinno, A. Agnesi, F. Pirzio, S. Chaitanya Kumar, and M. Ebrahim-Zadeh. "Femtosecond Mid-IR Optical Parametric Generation at 10 MHz with High Conversion Efficiency" Photonics Conference. 5-8 July 2023. IISc, Bengaluru, India.

5. S. Pizzurro*, Sukeert*, A. Esteban-Martin, R. Gotti, L. Carrà, G. Piccinno, A. Agnesi, F. Pirzio, S. Chaitanya Kumar, and M. Ebrahim-Zadeh. "Efficient Femtosecond Mid-IR Optical Parametric Generation at 10 MHz Pumped by a Mamyshev Fiber Oscillator and Amplifier" Advanced Solid State Lasers Conference, 08 - 12 October 2023, Tacoma, Washington.

6. R. Gotti, L. Carrà, S. Pizzurro, G. Piccinno, A. Agnesi, F. Pirzio. "Microchip Laser Started, 1-MW Peak Power Mamyshev Oscillator at 1 μm" Advanced Solid State Lasers Conference, 08 - 12 October 2023, Tacoma, Washington.

 * authors with equal contribution

Bibliography

[1] M. E. Fermann and I. Hartl. Ultrafast fiber lasers. *Nature Photonics*, 7(11):868–874, 2013.

[2] W. Fu, L. G. Wright, P. Sidorenko, Backus S., and F. W. Wise. Several new directions for ultrafast fiber lasers. *Optic Express*, 26(8):9432–9463, 2018.

[3] R. Paschotta. Mode-locked fiber lasers. RP Photonics Encyclopedia.

[4] P. Grelu and N. Akhmediev. Dissipative solitons for mode-locked lasers. *Nature Photonics*, 6:84–92, 2012.

[5] B.G. Bale, S. Boscolo, and K.T. Sergei. Dissipative dispersion-managed solitons in mode-locked lasers. *Optics Letters*, 34(21):3286–3288, 2009.

[6] M. E. Fermann, V. I. Kruglov, B. C. Thomsen, J. M. Dudley, and J. D. Harvey. Self-similar propagation and amplification of parabolic pulses in optical fibers. *Physical Review Letters*, 84:6010–6013, 2000.

[7] A.M. Heidt, J.P. Burger, J.N. Maran, and N. Traynor. High power and high energy ultrashort pulse generation with a frequency shifted feedback fiber laser. *Optics Express*, 15:15892–15897, 2007.

[8] K. Regelskis, J. Zeludevicius, K. Viskontas, and G. Raciukaitis. Ytterbium-doped fiber ultrashort pulse generator based on self-phase modulation and alternating spectral filtering. *Optics letter*, 40:5255–5258, 2015.

[9] Z. Liu, Z. M. Ziegler, L. G. Wright, and F. W. Wise. Megawatt peak power from a mamyshev oscillator. *Optica*, 4:649–654, 2017.

[10] P. Sidorenko, W. Fu, L. G. Wright, M. Olivier, and F. W. Wise. Self-seeded, multi-megawatt, mamyshev oscillator. *Optics letters*, 43:2672–2675, 2018.

[11] M. Piché. Mode locking through nonlinear frequency broadening and spectral filtering. *SPIE Proc. Vol. 2041 - Mode-locked and Other Ultrashort Laser Designs, Amplifiers, and Applications*, pages 358–365, 1994.

[12] P.V. Mamyshev. All-optical data regeneration based on self-phase modulation effect. *24th European Conference on Optical Communication (ECOC 98)*, page 475, 1998.

[13] M. E. Fermann, M. J. Andrejco, Y. Silberberg, and M. L. Stock. Passive mode locking by using nonlinear polarization evolution in a polarization-maintaining erbium-doped fiber. *Optics Letters*, 18(11):894–896, 1993.

[14] M. E. Fermann, F. Haberl, M. Hofer, and H. Hochreiter. Nonlinear amplifying loop mirror. *Optics Letters*, 15(13):752–754, 1990.

[15] Y. Chen, P. Sidorenko, R. Thorne, and F. W. Wise. Starting dynamics of a linear-cavity femtosecond mamyshev oscillator. *Journal of the Optical Society of America B*, 38:743–748, 2021.

[16] E. Treacy. Challenge and study for developing of novel single crystalline optical materials using micro-pulling-down method. *IEEE Journal of Quantum Electronics*, 5:454–458, 1969.

[17] D. Yan, X. Li, S. Zhang, and J. Liu. Pulse dynamic patterns in a self-starting mamyshev oscillator. *Optics Express*, 29:9805–9815, 2021.

[18] I. Samartsev, A. Bordenyuk, and V. Gapontsev. Environmentally stable seed source for high power ultrafast laser. *Proc. SPIE*, 10085, 2017.

[19] V. Boulanger, M. Olivier, F. Guilbert-Savary, F. Trépanier, M. Bernier, and M. Piché. All-fiber mamyshev oscillator enabled by chirped fiber bragg gratings. *Optics letters*, 45:2672–2675, 2020.

[20] P. Repgen, D. Wandt, U. Morgner, J. Neumann, and D. Kracht. Sub-50fs, μj-level pulses from a mamyshev oscillator–amplifier system. *Optics Letters*, 44:5973–5976, 2019.

[21] A. Agnesi, L. Carrà, F. Pirzio, R. Piccoli, and G. Reali. Low repetition rate, hybrid fiber/solid-state, 1064 nm picosecond master oscillator power amplifier laser system. *Journal of the Optical Society of America B*, 30:2960–2965, 2013.

[22] G. Agrawal. *Nonlinear Fiber Optics*. (Elsevier, 6th edition, 2019.

[23] J. Fève, P. E. Schrader, R. L. Farrow, and D. A.V. Kliner. Four-wave mixing in nanosecond pulsed fiber amplifiers. *Optics Express*, 15:4647–4662, 2007.

[24] A. S. Y. Hsieh, G. K. L. Wong, S. G. Murdoch, S. Coen, F. Vanholsbeeck, R. Leonhardt, and J. D. Harvey. Combined effect of raman and parametric gain on single-pump parametric amplifiers. *Optics Express*, 15:8104–8114, 2007.

[25] P. Kryukov and V. Letokhov. Fluctuation mechanism of ultrashort pulse generation by laser with saturable absorber. *IEEE Journal of Quantum Electronics*, 8(10):766–782, 1972.

[26] S. Pizzurro, R. Gotti, L. Carrà, G. Piccinno, A. Agnesi, and F. Pirzio. Femtosecond mamyshev fiber oscillator started by a passively q-switched microchip laser. *Optics Letters*, 47:1960–1963, 2022.

[27] D. Strickland and G. Mourou. Compression of amplified chirped optical pulses. *Optics Communications*, 55:447–449, 1985.

[28] O. E. Martinez. 3000 times grating compressor with positive group velocity dispersion: Application to fiber compensation in 1.3-1.6 μm region. *IEEE Journal of quantum electronics*, QE-23:59–64, 1987.

[29] A.S. Woutersen, U. Emmerichs, and H.J. Bakker. Femtosecond mid-ir pump-probe spectroscopy of liquid water: Evidence for a two-component structure. *Science*, 278(5338):658–660, 1997.

[30] J. Ma, Z. Qin, G. Xie, L. Qian, and D. Tang. Review of mid-infrared mode-locked laser sources in the 2.0 μm–3.5 μm spectral region. *Applied Physics Reviews*, 6(2), 2019.

[31] R. Das, S. C. Kumar, G.K. Samanta, and M. Ebrahim-Zadeh. Broadband, high-power, continuous-wave, mid-infrared source using extended phase-matching bandwidth in mgo: Ppln. *Optics letters*, 34(24):3836–3838, 2009.

[32] C. F. O'Donnell, S. Chaitanya Kumar, and M. Ebrahim-Zadeh. Enhancement of efficiency in femtosecond optical parametric oscillators using group-velocity-matching in long nonlinear crystals. *APL Photonics*, 4(5), 2019.

[33] Sukeert, S. Pizzurro, A. Esteban-Martín, R. Gotti, L. Carrà, G. Piccinno, A. Agnesi, F. Pirzio, S. Chaitanya Kumar, and M. Ebrahim-Zadeh. Efficient femtosecond optical parametric generation in group-velocity-matched mgo: Ppln at 10 mhz. *Optics Letters*, 48(22):6008–6011, 2023.

[34] Sukeert, S. Pizzurro, A. Esteban-Martin, R. Gotti, L. Carrà, G. Piccinno, A. Agnesi, F. Pirzio, S. Chaitanya Kumar, and M. Ebrahim-Zadeh. Efficient femtosecond optical parametric generation in group-velocity-matched mgo:ppln at 10 mhz. *Optica Advanced Photonics Congress 2022*, page ATh3A.5, 2022.

[35] Sukeert, S. Pizzurro, A. Esteban-Martin, R. Gotti, L. Carrà, G. Piccinno, A. Agnesi, F. Pirzio, S. Chaitanya Kumar, and M. Ebrahim-Zadeh. High conversion efficiency broadband femtosecond mid-ir optical parametric generation at 10 mhz. *The European Conference on Lasers and Electro-Optics*, page cd_6_1, 2023.

[36] O. Gayer, Z. Sacks, E. Galun, and A. Arie. Temperature and wavelength dependent refractive index equations for mgo-doped congruent and stoichiometric linbo 3. *Applied Physics B*, 91:343–348, 2008.

[37] S. Pizzurro, Sukeert, A. Esteban-Martin, R. Gotti, L. Carrà, G. Piccinno, A. Agnesi, F. Pirzio, S. Chaitanya Kumar, and M. Ebrahim-Zadeh. Efficient femtosecond mid-ir optical parametric generation at 10 mhz pumped by a mamyshev fiber oscillator and amplifier. *Laser Congress 2023 (ASSL, LAC)*, page AM6A.4, 2023.

[38] R. Gotti, L. Carrà, S. Pizzurro, G. Piccinno, A. Agnesi, and F. Pirzio. Microchip laser started, 1-mw peak power mamyshev oscillator at 1 μm. *Laser Congress 2023 (ASSL, LAC)*, page ATu2A.5, 2023.